Alma Mater Studiorum - Università di Bologna

Dottorato di Ricerca in Ingegneria Elettronica, Telecomunicazioni e Tecnologie dell'Informazione

Ciclo 34

Settore Concorsuale: 09/F1
Settore Scientifico Disciplinare: ING-INF/02
CAMPI ELETTROMAGNETICI

RF ENERGY HARVESTING SOLUTIONS FOR ELECTROMAGNETIC HARSH ENVIRONMENTS: FROM INDUSTRIAL PLANTS TO WEARABLE/IMPLANTABLE DEVICES

Presentata da:
Francesca Benassi

Coordinatore di Dottorato:
Prof. Ing. Aldo Romani

Supervisore:
Prof. Ing. Diego Masotti

Co-Supervisore:
Chiar.ma Prof.ssa Ing. Alessandra Costanzo

Esame Finale Anno 2022

Contents

Abstract

The presented Thesis describes the design of RF-energy harvesting systems with applications on different environments, from the biomedical side to the industrial one, tackling the common thread problem which is the design of complete energy autonomous tags each of them with its dedicated purpose. This Thesis gathers a work of three years in the field of energy harvesting system design, a combination of full-wave electromagnetic designs to optimize not only the antenna performance but also to fulfil the requirements given by each case study such as dimensions, insensitivity from the surrounding environment, flexibility and compliance with regulations. The research activity has been based on the development of highly-demanded ideas and real-case necessities which are in line with the environment in which modern IoT (Internet of Things) applications can really make a positive contribution. The following Thesis will describe four main activities carried out in the field of energy harvesting, and also wireless power transfer, for applications belonging to the medical and industrial sectors, two environments apparently so divergent, albeit equally challenging.

The Thesis is organized as follows: the first application, described in Chapter 2, regards the design and experimental validations of a rotation-

insensitive WPT system for implantable devices. The system receiver element is made of three coils each attached to its dedicated rectifier circuitry, arranged in such a way that quasi-constant powering is achieved regardless the RX rotation in the 3-D plane. The new idea developed with this implementation combines a CAD design that takes into account small coils arranged in a 3-D structure, together with an appropriate implementation of the rectifier and matching network circuit that allows for guaranteeing constant wireless power transfer capabilities. This capability can provided a strong added value to overcome a common challenge of most designs based on inductive resonant WPT: the performance degradation occurring when the RX coils is rotated.

Always related to the biomedical environment, Chapter 3 presents the design of a wearable and energy autonomous detector to identify the presence of ethanol on the body surface. The system is intended to be wrapped around the wrist as a bracelet, to monitor the correct hygiene procedure when hand sanitizers are used: the sensing is performed by means of a microfluidic channel placed on top of resonant stub that is tuned to open resonate at 2.45 GHz when the target solution is present. A new technique to perform a safe readout of the channel content, and thus a correct fluid detection, is presented in this Chapter, adding a novel approach to common passive dielectric spectroscopy techniques. The resonant stub is placed in substitution of one open end of a second order coupled line filter whose

main function is to perform frequency selectivity and decoupling between the antenna, dedicated to the power reception, and the rectifier, responsible for power transduction. The readout is performed by reading different dc-output voltage levels. The energy autonomy, together with the passive activation and complete wearability, contribute to make this detector fully compliant with the requirements of IoT technologies.

Leaving the microwave range to welcome the millimetre one, Chapter 4 describes investigations in the use of Bessel Beam launchers for creating a highly-focused energy harvesting link for wearable applications. Reduced dimensions, high focusing and decoupling from the human body are the key points to be addressed during the full-wave design and nonlinear optimization of the receiver antenna. Due to the higher operating frequencies of the two compared solutions, TM- and TE-polarized BB launchers operating at 37.5 and 30 GHz respectively, and the intrinsic properties of limited nondiffractive region, the maximum operating distance has been found to be 40 mm for which an $\eta_{RF-to-dc}$ of around 15% is achieved. Further in-depth studies are currently being performed to improve this solution to make it as feasible as possible to be applied in a biomedical real-case scenario. However, the novel idea of using Bessel Beam launchers within a wireless power transfer applications has found interesting feedbacks from the scientific community.

Finally, Chapter 5 presents an energy autonomous system exploiting

LoRa (Long Range) nodes for tracking trailers in industrial plants. High gain antenna arrays are used to provide power from the main source located in the main trailer to the attached ones, in a cascade configuration. The combination of wireless powering between two trailers and cable connection within each trailer allows for providing sufficient amount of power to five trailers each of them is equipped with a LoRa node. Each trailer hosts two antennas, one for reception and the other for transmission placed at the two edges of the trailer and connected by a coaxial cable. From the total amount of power that is received from each trailer, a small portion is collected by means of an embedded power splitter that sends a small percentage to the rectifier and then to the LoRa node, creating a system whose modularity clearly is an important added value. The novelty behind this design lies on the aim of obtaining a perfectly scalable system that exploits not only energy harvesting basic operating systems but embeds a seamless solution for collecting a certain amount of power that varies with respect the received power level on the antenna, without the need of additional off-the-shelf components.

List of abbreviations and acronyms

BB Bessel Beam

BW Bandwidth

CP Circularly Polarized

DC Direct Current

EH Energy Harvesting

EIRP Effective Isotropic Radiated Power

EM Electromagnetic

FBC Fabry-Perot Cavity

GaAs Gallium Arsenide

HB Harmonic Balance

ICNIRP International Commission on Non-Ionizing Radiation Protection

IIoT Industrial Internet of Things

IoT Internet of Things

ISM Industrial, Scientific and Medical

LoRa Long Range

LPWAN Low-Power Wide-Area Network

LRW Leaky Radial Waveguide

MPPT Maximum Power Point Tracker

PCE Power Conversion Efficiency

PMU Power Management Unit

PRS Partially Reflecting Surface

PTE Power Transfer Efficiency

RF Radiofrequency

RX Receiver

SAR Specific Absorption Rate

SMD Surface Mount Device

TE Transverse Electric

TM Transverse Magnetic

TX Transmitter

WPT Wireless Power Transfer

WSNs Wireless Sensor Networks

List of symbols

$k_{i,j}$	Coupling coefficient
Q	Q-factor
λ_0	Free-space wavelength
$\eta_{RF-to-dc}$	RF-to-dc power conversion efficiency
$\eta_{RF-to-RF}$	RF-Link Efficiency
θ,ϕ	Rotational angles
ε_r	Relative permittivity
$tan\delta$	Loss tangent
δ	Antenna radiation efficiency
$S_{i,j}$	Scattering parameter
k_ρ	Radial wavenumber
β	Phase constant
α	Attenuation constant
k_0	Free-space wavenumber
C_ρ	Confinement ratio
S_ρ	Radial spot size
ρ_{ap}	Antenna aperture
J_0	Zeroth-order Bessel function
j_{0n}	nth-zero of the J_0 Bessel function
z_{ndr}	Nondiffractive range
θ_0	Axicon angle (Chapter 4)
J_{eq}	Equivalent current source
Y_A	Antenna admittance
Z_A	Antenna impedance
Z_C	Characteristic impedance
Z_{RECT}	Rectifier input impedance
X_{s}	Sheet Reactance

Acknowledgements

When viewed from the outside, three years of doctoral studies may appear to be a mere interlude in one's life and work. However, I recognise that many people have made significant contributions to this experience, and while a single page would be insufficient, I would like to express my gratitude to them.

First and foremost, I want to express my heartfelt gratitude to my supervisors, Prof. Diego Masotti and Prof. Alessandra Costanzo, whose expertise, dedication, and enthusiasm were invaluable in developing the research questions and methodology, and whose constant guidance has propelled my research to new heights. Outstanding mentors and leaders for all of us, they have always provided insightful remarks and support, widening my research activities to cover different prospectives.

I would like to express my sincere gratitude to Giacomo Paolini for being not only an amazing colleague but also one of the pillars of the fantastic team with whom I had the pleasure of working. Together with him, I would like to thank all of my RFCAL Lab colleagues: Baris, Enrico, Simone, Mazen, Elisa, Giulia, and Alessandra for all of the fun times we have had. Every day, we have been accompanied by enthusiasm, respect, an interchange of ideas, mutual encouragement, and support, making our labour far from insignificant.

I would also like to thank Prof. Milica Popovic and Prof. Alessandro Galli, whose valuable comments and feedback helped to improve the quality of my Thesis and served as motivation for future developments.

I would like to thank Prof. Alessandro Lipparini, for the constructive comparisons, enthusiastic support, and insights provided throughout these three years of research activity.

I would like to express my gratitude to Dr. Walter Fuscaldo for sharing his knowledge with such zeal, which has aided my professional development in the field of leaky wave antennas.

I would like to convey my heartfelt gratitude to the IEEE MTT-S Education Committee and the European Microwave Association (EuMA) for providing me with outstanding possibilities to expand my research activity as a young researcher.

I'd like to thank the University of Glasgow and Dr. Masood Ur Rehman for the opportunity to work as a visiting researcher.

My sincere gratitude goes to my pals Riccardo, Michele, Francesco, Michael, Beatrice, and Filippo for their understanding ears, strong encouragement, and unending support.

My PhD would not have been possible without the help of my parents and my sister Federica, to whom I am extremely grateful.

Finally, I'd like to convey my heartfelt gratitude to Giacomo for always being a constant source of empathy and encouragement.

In memory of all the victims
of the COVID-19 pandemic.

1. Introduction

"When wireless is perfectly applied the whole earth will be converted into a huge brain, which in fact it is, all things being particles of a real and rhythmic whole. We shall be able to communicate with one another instantly, irrespective of distance. Not only this, but through television and telephony we shall see and hear one another as perfectly as though we were face to face, despite intervening distances of thousands of miles; and the instruments through which we shall be able to do this will be amazingly simple compared with our present telephone. A man will be able to carry one in his vest pocket.", Nikola Tesla, Collier's Magazine, 1926.

More than 100 years ago the pioneer of electromagnetism Nikola Tesla set the bases for the first wireless power transmission, confirmed by some experiments using inductive and capacitive coupling principles. However, the innovative idea was about the possibility to transfer electricity without the use of cables through the atmosphere or through the earth, but the technology was not so developed and able to make him prove this concept with thorough demonstrations. In parallel to Tesla, Guglielmo Marconi, an Italian inventor, was studying the possibility to transfer information wirelessly, as Nikola Tesla was doing for power, developing the first wireless telegraphy and becoming the first and official radio inventor. So it is

thanks to the unintentionally joint work of these two extraordinary minds, that nowadays we can make use of certain technologies, such as using our smartphone to call the other side of the world, that sometimes are taken too much for granted. From Tesla's and Marconi's works, technology has developed exponentially, setting the basis for what nowadays is called the *"Internet of Things"* that finds applications in various and diversified environments: industries and health [1, 2], agriculture [3], logistics [4], retail [5] and many others.

The adjective "smart", when associated to modern technological applications, gathers a wide meaning describing devices that are equipped with multiple sensors to perform, for example, the monitoring, localization, and optimization of industrial processes, while, at the same time, achieving energy autonomy, compactness, lightness and non-intrusiveness, which are some of the pillars of the IoT world [6]. The so called "smart-health" is considered a breakthrough to overcome multiple issues related to patient care [7–12], equipment tracking in hospitals [13] or monitoring and localization of elderly people in nursing homes [14, 15]. These modern devices are mainly wearable, thus characteristics such as lightness, wearability and comfort, miniaturization and compactness must be key points on which their design is based.

One important key role is played by the energy autonomy of these devices, a concept that is increasingly raising interests among the electronic

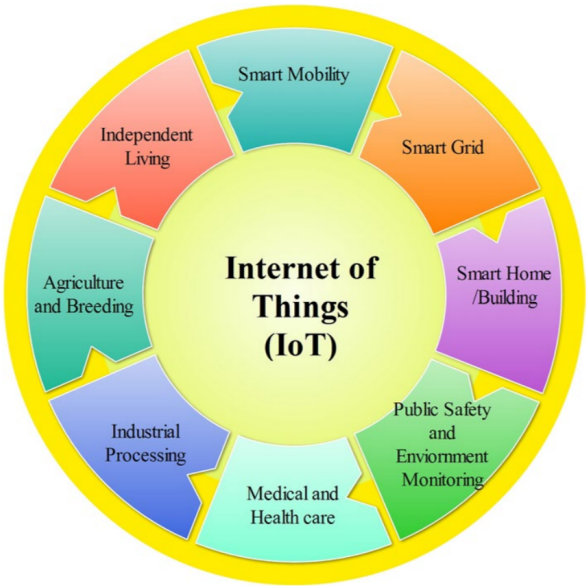

Figure 1.1: Schematic representation of common applications of the IoT technologies. [16]

devices manufactures. Although battery efficiency has been extended thanks to modern technological advancements, they still require maintenance and, most of the time, batteries contribute to make this devices bulky, drastically in contrast with the required characteristics of compactness and lightness. For this reason, together with the aim of reducing battery disposal and thus pollution, modern IoT devices are thought and designed to be powered wirelessly.

To achieve this purpose, energy must be provided directly to the device (Wireless Power Transfer) or must be collected from the environment (Energy Harvesting). Energy can be harvested from multiple and different sources such as piezoelectric one, exploiting mainly Kinetic Energy [18], photovoltaic [19], thermoelectric [20], electromagnetic [21, 22] and several

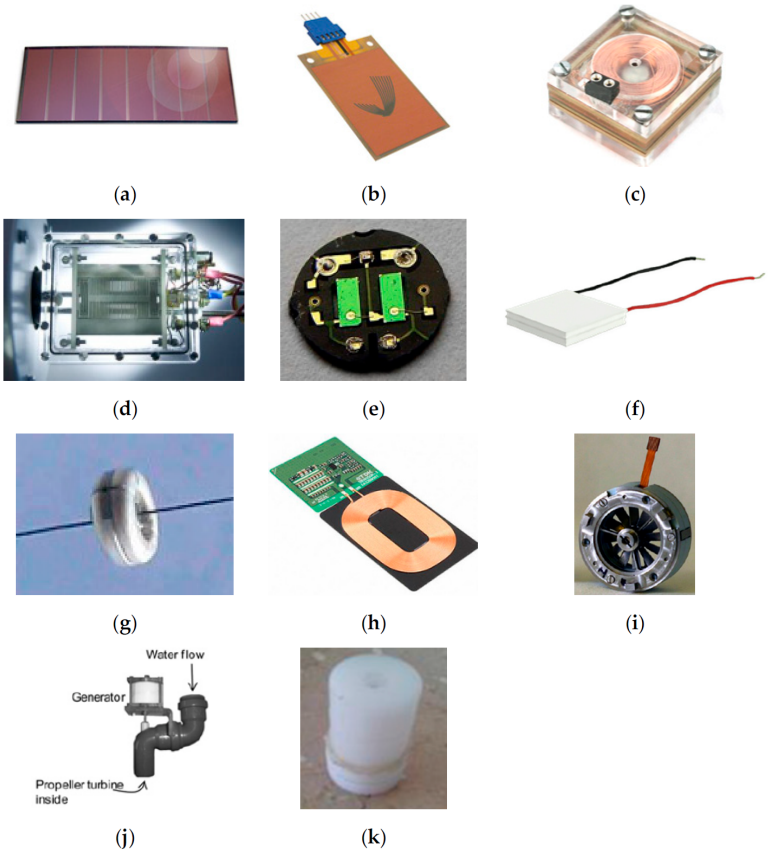

Figure 1.2: Examples of energy harvesting topologies: (a) Photovoltaic; (b) Piezoelectric; (c) Electromagnetic; (d) Electrostatic; (e) Pyroelectric; (f) Thermoelectric; (g) Magnetic; (h) RF; (i) Wind flow; (j) Liquid flow; (k) Acoustic noise. [17]

others, schematically gathered in Fig. 1.2. In some cases, the need for harvesting energy can be occasional, requiring energy "on demand", for this reason, designing devices that are wirelessly powered can have a twofold goal of enhancing the efficiency and life cycle of the device itself and maximizing the efficiency of the overall power consumption, reducing unnecessary waste. In this Thesis, different energy-autonomous systems based on RF-energy harvesting, and wireless power transfer, are described, belonging to two main operative contexts: the biomedical one, namely devices which

are designed to be wearable and exploited within medical applications, and the industrial one, where the target devices are placed in electromagnetically harsh environment, a constant challenge for the overall design. The energy provided through electromagnetic waves is strictly related to multiple parameters. In particular, the distance from the RF source, the antenna radiation performance, such as gain, as well as the environment topology (presence of surrounding metal or interposed obstacles) do affect the amount of power that can be harvested on the receiver side [23]. Although RF sources are really important to thoroughly describe an energy harvesting system, this Thesis will be mainly focused on the receiving side, with design and experimental validations of rectifying antennas, called "*rectennas*". These antennas are equipped with a circuitry dedicated to RF-to-dc power conversion and a power storage unit to collect the harvested power to energize a specific device to which they are connected. The RF power is provided by sources that can be dedicated or environmental. The former, requires an accurate design with previous knowledge of the mutual and possible positions between the source and the tags to be powered; the latter exploits ambient RF sources which are highly accessible, especially in urban areas. [24] proposes a spectral survey carried out in the London urban area that shows how possible could be to harvest power in the frequency range between 0-3 GHz, between 10:00 am and 3:00 pm, exploiting the Electromagnetic (EM) density provided by mobile phone usage. Be-

ing the direction of this type of sources unknown, the receiving antenna dedicated to the energy harvesting must be as omnidirectional as possible. Measurements of the RF power density have been performed inside the Department of Electrical and Electronic Engineering ICL, London building, and the results have allowed a good prediction of the expected RF power level, as shown in Fig. 1.3 [24].

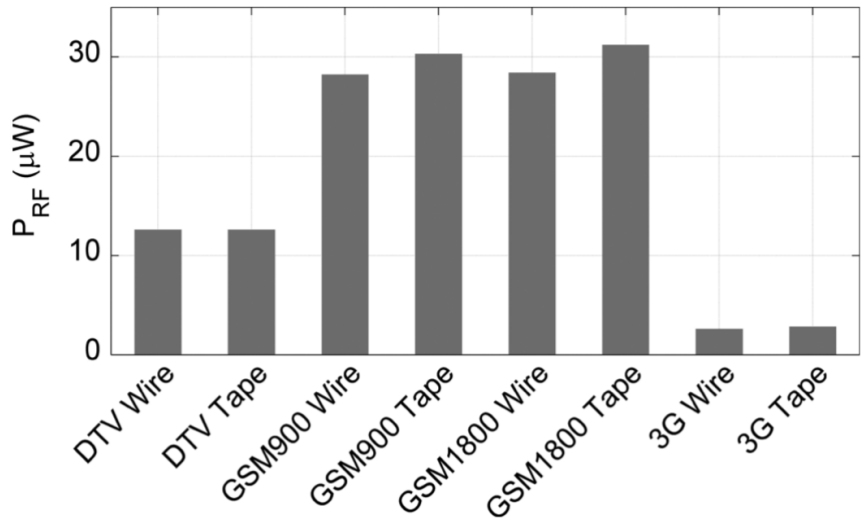

Figure 1.3: Expected RF input power levels due to four ambient sources at ICL. [24] © 2015 IEEE

A half-wave rectifier and power management module have been integrated and optimized with respect to the predicted input power level (Fig. 1.3), allowing for an estimation of an end-to-end efficiency, the ratio between the energy supplied to the load and the input RF energy [24], that is about 40% for an RF input power of -25.4 dBm. Authors have investigated the option of using a multiband array architecture to cover all the eight frequencies, while the rectifier configuration has been studied for two cases: the first con-

siders multiple rectennas with shared power management module (PMM), whereas the second takes into account a multiple rectenna configuration with individual PPMs [24]. This last topology allows for lowering the input power level for harvesting power down to -29 dBm, although improving on the structure interconnection and power balance between the circuital branches must be investigated, especially for the lowest input power levels. Indeed, this study shows how promising the implementation of RF energy harvesting system can be, especially in urban areas.

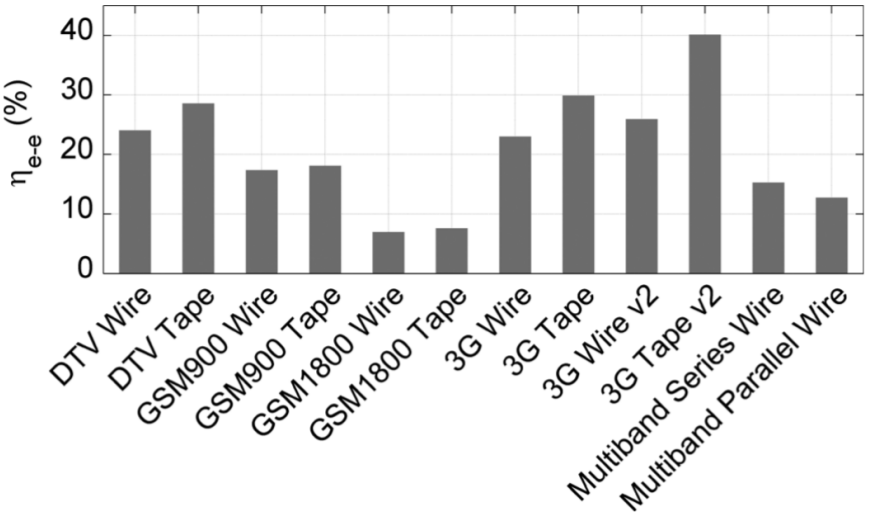

Figure 1.4: Expected end-to-end efficiency. [24] © 2015 IEEE

Many applications based on RF-harvesting can also be derived on textile materials to ease wearability without negatively impacting the performance of the whole system. To ease comfort and flexibility in wearable applications, conventional substrate-based rectennas are substituted with antennas derived on denim, felt, wool and other fabrics [25, 26].

In [27], a tightly coupled antenna array, working in the 2-5 GHz frequency range, for energy harvesting applications, is presented. To perform a more thorough optimization of the circuit, in particular for the rectifier one, a preliminary estimation of the expected power level density on the ambient is performed, allowing for a safe characterization in the 0.5-2.5 GHz frequency band mainly, as shown in Fig. 1.5.

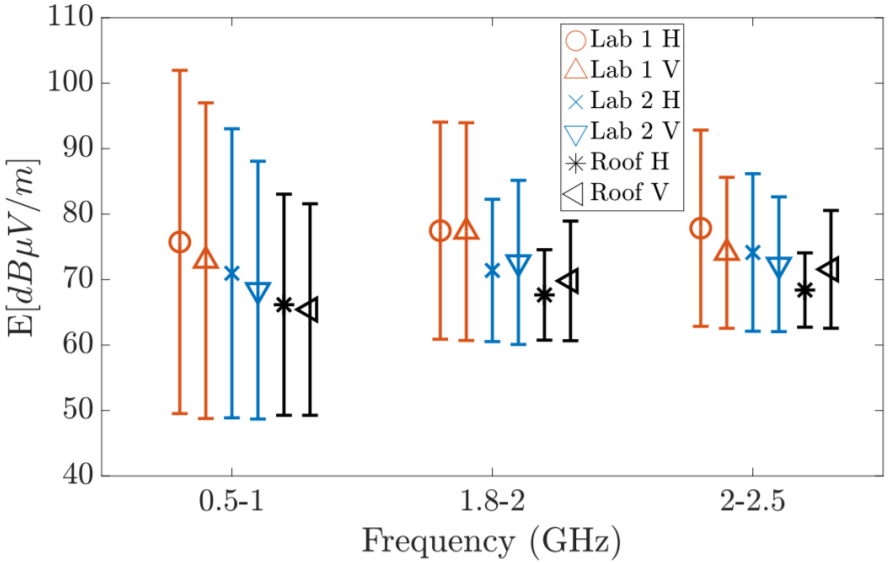

Figure 1.5: Measurement of the Electric field in three different environments over a period of time of three hours. [27] © 2020 IEEE

To perform the antenna design the diode SMS7630-079LF is firstly characterized by means of circuital harmonic balance optimizations with respect to a broad frequency range and different incident power densities, to establish the best impedance values that the antenna has to present to perform in the most efficiency conditions. The antenna array, loaded with the rectifier, is then designed with a period of $\lambda_0/6$ at 5 GHz, with λ_0 the free-space

wavelength, and full-wave simulations are conducted with the array placed on a realistic body torso for a 4x4 and 9x9 array configuration. The simulated stack up is presented in Fig. 1.6.

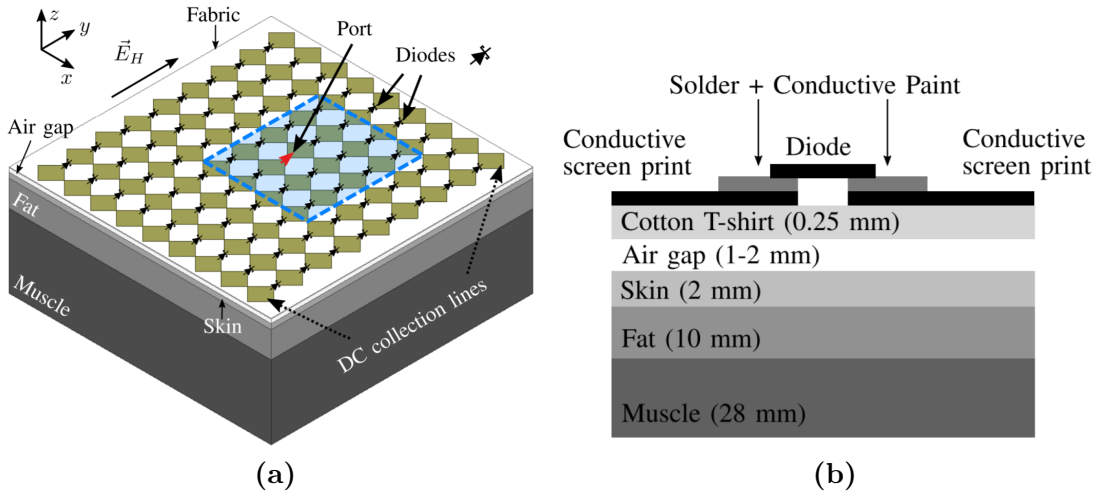

Figure 1.6: (a) schematic representation of the simulated system for the 9 x 9 array configuration and (b) cross-section description of the body torso model used for full-wave simulations. [27] © 2020 IEEE

As shown in Fig. 1.6b, the air gap between the clothing and body (h) may vary, thus simulations on the antenna radiation performance are conducted for increasing values of h, showing no drastic changes for a variation between 1-2 mm, but highlighting an evident variation for values between 0-1 mm, suggesting that extremely thin fabric should not be used for this implementation. The prototype is fabricated using a metallized ink on a cotton tee-shirt and firstly characterized using a phantom body made of saline solutions. The received power on the antenna surfaces is preliminary characterized making use of the Friss' line-of-sight equation for a given distance of 69 cm between the TX and RX antennas, when varying the power

density on the RX antenna from 3 to 130 μ W/cm^2. Subsequently, an incident power density of 4 μ W/cm^2 and a dc-load of 2 $k\Omega$ is considered as set up for the final measurements of the rectifier dc-power. These measurements are carried out in the 2-5 GHz- frequency range, for three different cases, on body and with or without the phantom, while considering two antenna polarizations, vertical and horizontal [27]. The obtained results are displayed in Fig. 1.7. Authors state that the obtained outcomes show that, in order to achieve better efficiency, is more useful to combine the dc-power of a number of small arrays than use a single larger one.

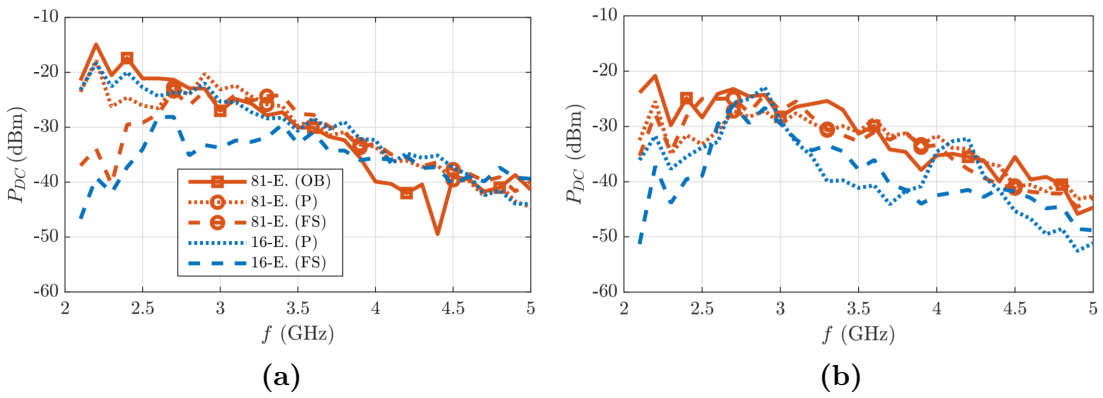

Figure 1.7: dc-power vs frequency for the 4 x 4- (blue curves) and 9 x 9- (red curves) element arrays. Measurements are conducted on-body (OB), using phantom (P) and in free space (FS) considering a horizontal (a) and vertical (b) polarization. [27] © 2020 IEEE

Whereas the system [27] is fully derived on a fabric substrate, other implementations have found convenient to combine fabrics with standard substrates to enhance the performance of the rectifier circuit. In [28], a wearable and flexible energy harvesting system, operating at 2.45 GHz at a TX-RX distance of about 2 m, is presented. The rectenna radiating

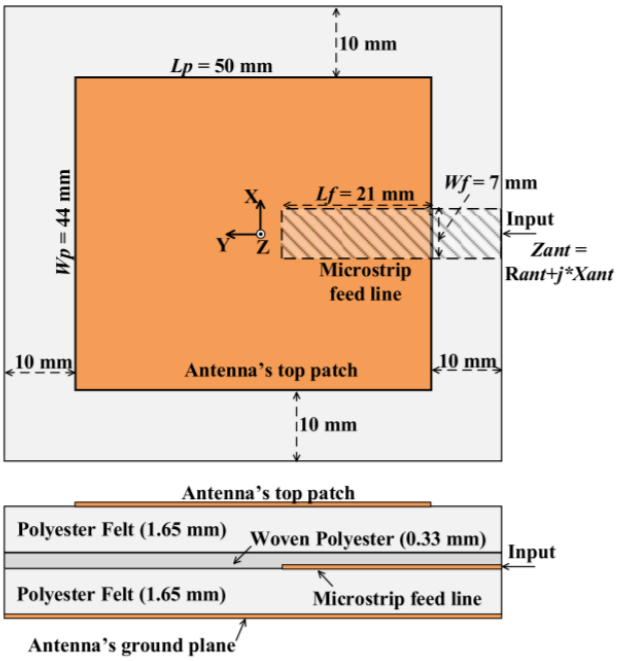

Figure 1.8: Stack-up of the antenna described in [28]. © 2018 IEEE

part is composed of a microstrip-fed patch antenna derived on a multi-layered structure of both polyester felt ($\varepsilon_r = 1.2$, $\tan\delta = 0.023$) and woven polyester ($\varepsilon_r = 1.5$, $\tan\delta = 0.028$), as shown in Fig. 1.8, performing a gain and radiation efficiency of about 6.8 dBi and 62% respectively when worn around the wrist. The rectifier is derived on a conventional RF substrate, the Rogers RT/duroid 5880 ($\varepsilon_r = 2.2$, $\tan\delta = 0.0009$), and makes use of a single Schottky diode, the SMS7630 from Skyworks, achieving an $\eta_{RF-to-dc}$ power conversion efficiency of about 33.6% at -20 dBm [28], as displayed in Fig. 1.9.

Flexibility and wearability have been two of the main objectives that have been targeted within this Thesis activity. Chapter 3 presents a wearable energy harvesting system for the detection of ethanol solution on the body

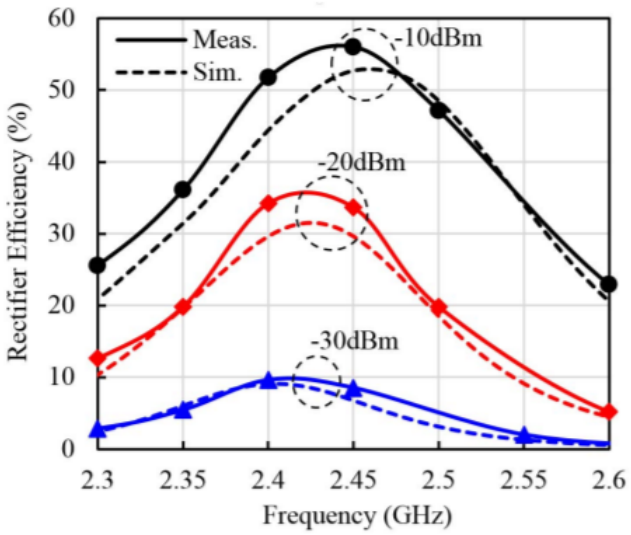

Figure 1.9: Rectification efficiency for different rectifier input powers. [28] © 2018 IEEE.

surface. As well as in [28], a patch antenna is used as the main radiating element of the rectenna, thanks to the presence of a background plane that allows for electrical decoupling from the body surface. Due to the fact that the proposed system accounts for three main elements: a patch antenna for signal reception, a coupled-line filter embedding a miniaturized meandered microfluidic channel for fluid detection, and a rectifier to perform not only the $\eta_{RF-to-dc}$, but also a safe readout, the operative choices has opted for the use of a single RF substrate, the Rogers RT/duroid 5880, for the whole rectenna. The $\eta_{RF-to-dc}$ is optimized as a good trade-off between maximization and capability of differentiate the fluids under test, creating a rectenna that may not be as efficient as the one presented in [28], but that allows for behaving not only as energy harvester, but also as wireless passive detector, without introducing any further circuitry component.

As in the previous cases, single-frequency rectennas are widely spread and allow a more controllable full-wave/nonlinear optimization. However, multi band rectennas can enhance their versatility especially when RF-sources of multiple frequencies are present. [29] describes the design and implementation of a multiband rectenna for ambient energy harvesting purposes, that operates in four frequency bands: 840 MHz, 1.8, 2.1 and 2.45 GHz, respectively.

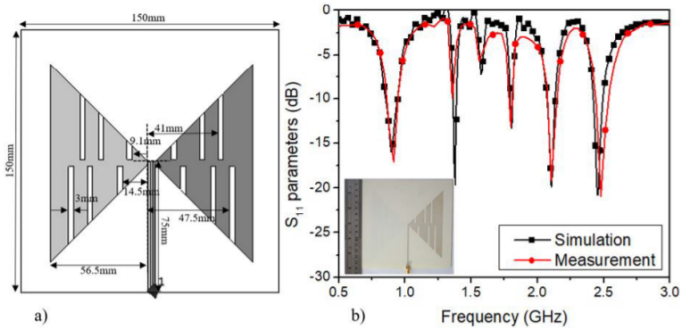

(a)

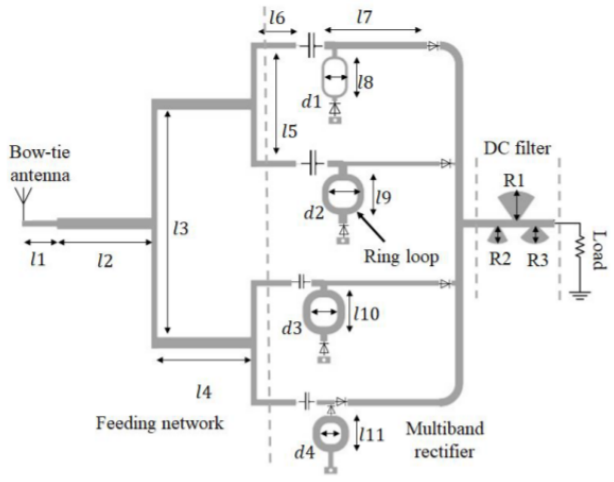

(b)

Figure 1.10: (a) slotted bow-tie antenna and (b) multiband rectifier with $l1 = 10$, $l2 = 24$, $l3 = 63$, $l4 = 23.5$, $l5 = 31.8$, $l6 = 10$, $l7 = 27.6$, $l8 = 9$, $l9 = 6.5$, $l10 = 7$, $l_1 1 = 5$, $d1 = 5$, $d2 = 7$, $d3 = 6.5$, $d4 = 5$, $R1 = 8$, $R2 = 4$, $R3 = 4$. [29] © 2020 IEEE

The radiating element is a slotted bow-tie antenna derived on a Rogers 4003C substrate of a thickness of 0.8 mm (Fig 1.10a), whereas the rectifier is a 4-branch circuit, Fig 1.10b, each of them corresponds to one of the four operating frequencies and embeds a single Schottky diode to achieve the maximum efficiency while maintaining the same dc-load. As reported, the peak $\eta_{RF-to-dc}$ power conversion efficiencies are 46%, 42%, 42% and 36% at 0.84, 1.86, 2.1 and 2.4 GHz respectively [29].

Although the ambitious goal of powering a device without the need of cables is based on accurate design and expertise, working outside the medical context may relieve a little stringent requirements. However, being able to power wearable, or even implantable, devices can have a drastic impact on patients treatments and also life quality. In particular, most of the implanted devices require batteries to function correctly (i.e. pacemakers, defibrillators...); although batteries life has been extended thanks to the technological development, after a certain time, patients must undergo surgical procedures to have their device batteries replaced. We all agree that powering those kind of devices can be a breakthrough and a risk at the same time, since vital devices are considered, but for many other topologies of medical devices, being energy autonomous can definitely be more than a simple added value. Having devices that acquire the needed power from external sources can guarantee continuos operative conditions and be of a paramount importance when monitoring patient's parameters

whose abnormality requests medical interventions.

Madal et al. [30] have designed a completely energy-autonomous wearable tag that is able to monitor physiological parameters such as phonocardiogram (PCG), electrocardiogram (EKG), blood oxygen saturation (photoplethysmograph, PPG), respiratory sounds, blood pressure and body temperature and generates alarms in the case of medical emergency. The system is able to harvest energy from an RF-source by making use of two CMOS rectifiers connected to an antenna for power reception. A representation of the system proposed by *Madal et al.* [30] is reported in Fig. 1.11:

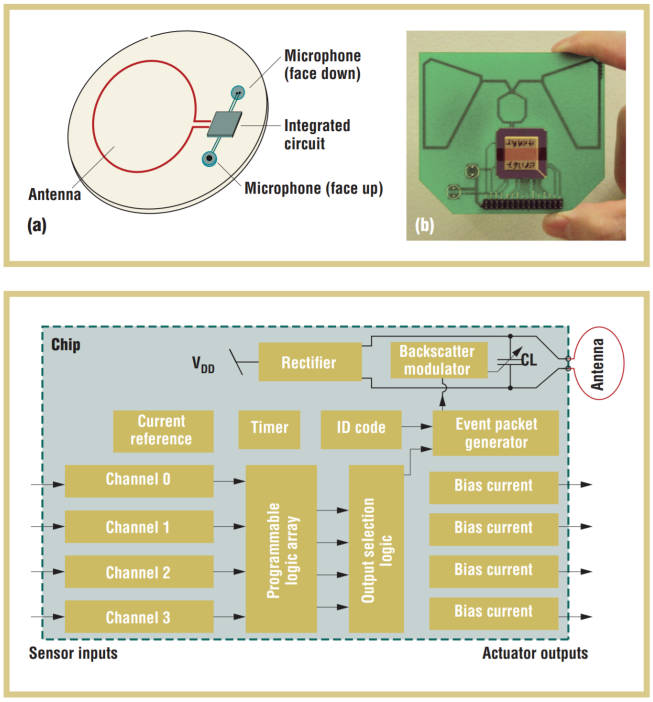

Figure 1.11: Picture of the realized tag and block diagram of the chip. [30] © 2009 IEEE.

Experimental results have confirmed a reading range of about 3.1 m at the operating frequency of 800 MHz when providing 800 mW-EIRP.

In this reading range, the minimum harvested power is 15 μ W which is sufficient to power the embedded microphone and perform the PCG [30]. The system is also simulated at 2.45 GHz with the purpose of reducing the antenna dimensions, with the consequent shortening of the reading range. As previously mentioned, energy harvesting systems can also be applied in industrial applications. As well as for the biomedical side, the main goal of reducing power consumption of each sensor node has made EH techniques of a paramount importance when applied in industrial plants [31–33]. Chapter 5 presents a system that boasts good efficiency in terms of WPT, tackling a more critical aspect that is related on how the distribution of this received power can be efficiently performed when having multiple nodes in a cascade configuration. Although applications of these energy harvesting system can be found in a variety of different scenarios, the operating principles can be commonly described.

The mutual position of two antennas within a radio channel identifies three different operative zones (see Fig. 1.12):

- the *Reactive Near-field* (Fresnel zone) occurring when the distance $d < 0.62\sqrt{D^3/\lambda}$,
- the *Radiating Near-field* (Fresnel zone) also called *Mid-field* when the distance $0.62\sqrt{D^3/\lambda} < d < 2D^2/\lambda$,
- the *Far-field* when $d < 2D^2/\lambda$ [34].

The *Reactive Near-field* is a region immediately surrounding the antenna

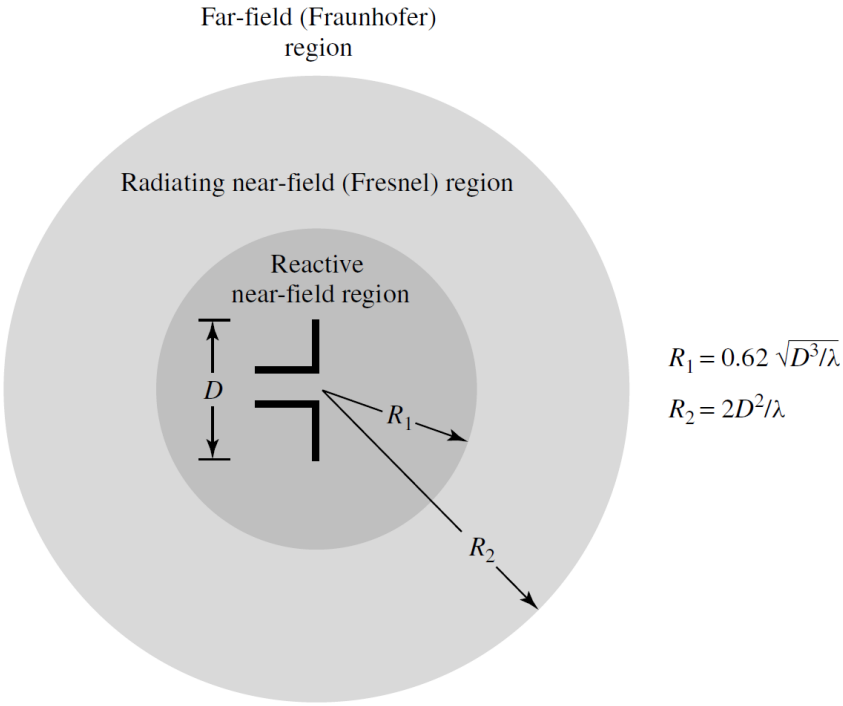

Figure 1.12: Field regions of an antenna [34].

where the reactive field predominates. The electric and magnetic fields are not necessarily in phase to each other and the angular field distribution is highly dependent upon the distance and direction from the antenna. In this region, interaction undergo the names of Inductive or Capacitive coupling depending on which field (magnetic or electric, respectively) contribution is the strongest [35]. In these applications, coils and plates are used both in transmission and reception but the interaction can be influenced by different factors such as mutual position, misalignment and geometry. In [36], near field communications is exploited to provide both wireless powering and perform communication to a small millimetre-scale NFC-enabled platform operating at around 14 MHz.

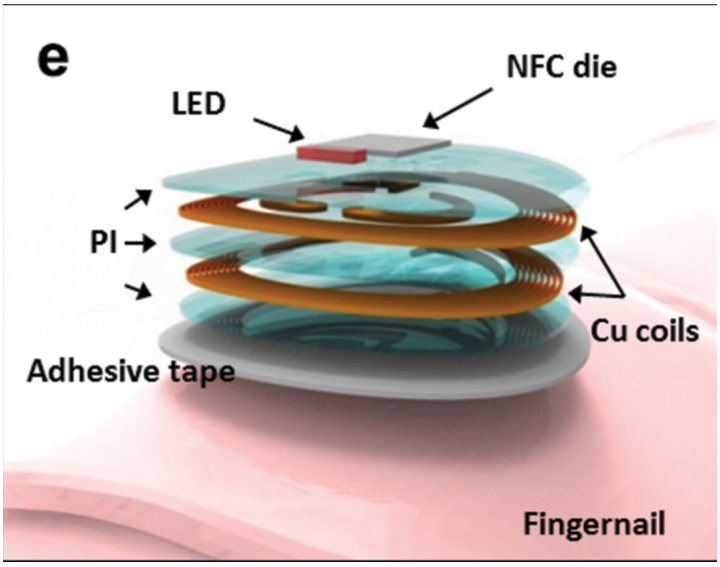

Figure 1.13: Stack representation of the small NFC chip [36].

Fig. 1.13 shows a stacked representation of the system made of two coils (8 turns each) with an overall diameter of 7.04 mm, and LED connected to the NFC die to perform temperature sensing. This device is enabled by using a standard smartphone at a distance of around 20 mm [36]. Devices like this one can certainly be really useful to have a constant monitoring of the body temperature or perform chemical sensing in bio-fluids, because the stretchability and reduced dimensions allow to reduce invasiveness in favour of comfort.

In the *Radiative near-field*, the reactive fields are not more dominant so the fields are characterized by a combination of reactive and radiative modes [37]. The electric and magnetic fields are in phase, but the angular field distribution is still dependent on the distance from the antenna.

The *Far-field* is dominated by radiated fields and the E and H-components

of the EM field are orthogonal to each other generating what are called *plane waves*. The radiation pattern does not change with the distance from between the antennas because there is no interaction between them (differently from the previous near-field case) and the amplitude of the E-and H-components decays with $1/d$.

In this Thesis, most applications operate in the *Far-field* with the only exception of the wireless link exploiting Bessel Beam launchers (Chapter 4), in which the transmitting and receiving antennas are made operate in the *Radiative Near-field*, and the rotational independent wireless power transfer system for implantable devices, Chapter 2, that operates in the *Reactive Near-field*.

Within an energy harvesting system the main role is played by the receiving *rectenna* (rectifying antenna) [38, 39], that needs to be modelled and optimized to maximize its performance both in terms of radiation properties but also in terms of rectification efficiency. As can be inferred by its name, a rectenna is an antenna that embeds a rectification circuit to harvest dc-power. A schematic block diagram, representing the main components of an energy harvesting system, is shown in Fig. 1.14:

The receiving antenna is connected to its rectifier through a matching network realized by means distributed or lumped components. This linear subnetwork is used to perform impedance matching between the antenna, that generally offers a purely real impedance Z_A (i.e. 50 Ω), when operat-

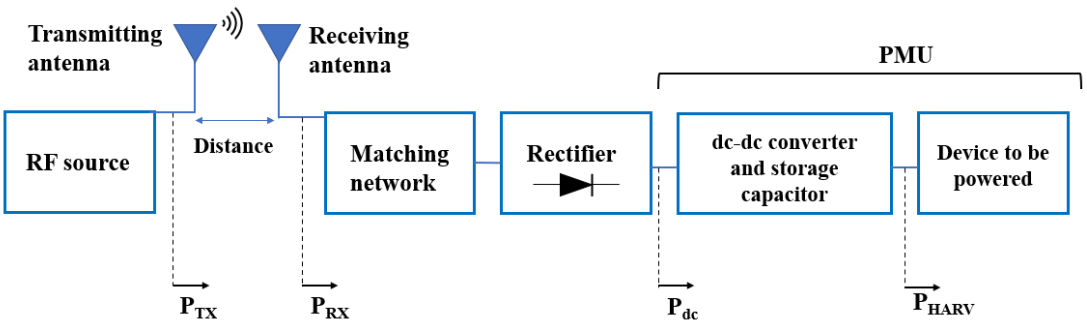

Figure 1.14: Schematic block diagram describing an RF energy harvesting system.

ing in resonant condition, and the rectifier whose complex input impedance Z_{RECT} is characterized by a small real part and higher negative imaginary part (i.e. $10 - j70\ \Omega$). A rectifier is an electrical nonlinear circuit device that converts an RF source (current or voltage or power, sinusoidally varying) to direct current (dc), a process known as rectification and it is composed of nonlinear components such as diodes. Different rectifier configurations can be exploited, as the half-wave rectifier made only by a single diode. This type can have a shunt diode (Fig. 1.15a) or a series diode (Fig. 1.15b) configuration, and ideally they provide dc-output voltage that is proportional to the RF-input power. The voltage doubler configuration (Fig. 1.15c) provides higher dc-output voltage but lower dc-output power mainly because of diode losses.

The dc-dc converter together with a storage capacitor is used to store the harvested power that is subsequently used to power a certain device. One of the main goals for rectenna designers is to maximize its overall efficiency [40], in particular, when modelling a rectenna system different

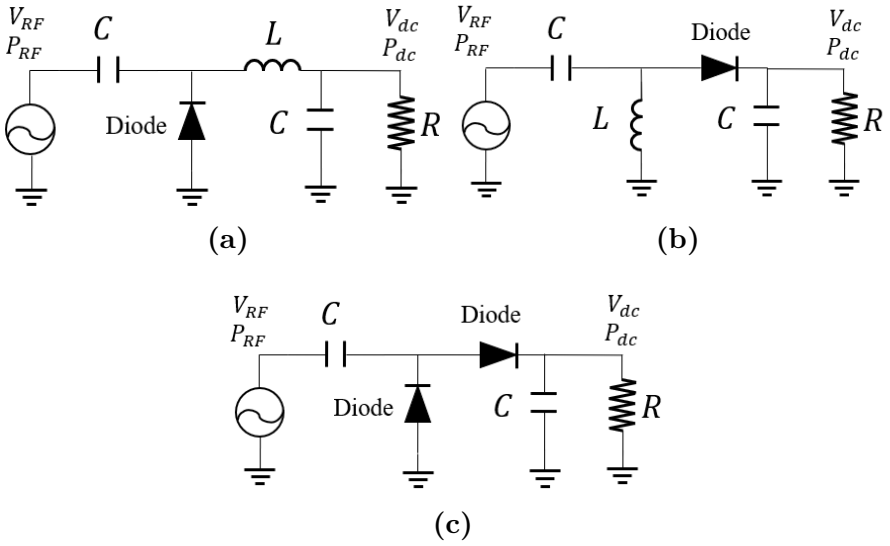

Figure 1.15: Circuital representation of the three different rectifier topologies: (a) shunt diode, (b) series diode and (c) voltage doubler.

efficiencies can be highlighted [41]. The *RF-to-dc* power conversion efficiency ($\eta_{RF-to-dc}$) is the ratio between the power measured at the rectifier output load and power received by the rectenna (see Fig 1.14 for reference):

$$\eta_{RF-to-dc} = \frac{P_{dc}}{P_{RX}} \tag{1.1}$$

This quantity needs to be optimized within the circuital simulations to identify how much power can be converted from RF to dc by the designed rectifier. Choosing the most suitable diode is an important step of a rectenna design, in fact depending on the operating frequency, input power level and application, not only the rectifier configuration is critical but also which diode can guarantee the best $\eta_{RF-to-dc}$ efficiency is an important selection. Fig. 1.16 groups some of the diodes that are commonly

used in energy harvesting applications.

	Far-Field WPT					
	HSMS-282x	**HSMS-286x**	**SMS7630**	**HSMS-285x**	**HMPS-2820**	**SMV1430**
I_s (A)	2.2e-8	5e-8	5e-6	3e-6	2.2e-8	1e-14
R_s (Ω)	6	6	20	25	8	3.15
n	1.08	1.08	1.05	1.06	1.08	1
C_{j0} (pF)	0.7	0.18	0.14	0.18	0.7	1.11
M	0.5	0.5	0.4	0.5	0.5	0.5
F_c	0.5	0.5	0.5	0.5	0.5	0.5
V_j (V)	0.65	0.65	0.34	0.35	0.65	0.86
B_V (V)	15	7	2	3.8	15	0
I_{BV} (A)	1e-4	1e-5	1e-4	3e-4	1e-4	1e-3
$\Re_{I0}$ (A/W)	18.02	18.02	18.53	18.36	18.02	19.46
			Harmonic Backscattering			

Figure 1.16: Spice parameters of the most used diodes for Energy Harvesting applications. [42] © 2021 IEEE

The following chapters will describe the main activities that have been carried out during the three years of PhD, covering the topic of RF energy harvesting system design for applications in harsh electromagnetically environments, belonging to two main sectors: the biomedical and the industrial one.

2. Rotation Insensitive Wireless Power Transfer System for Implantable Applications

This Chapter is based on the following articles:

[43] A. Pacini, F. Benassi, D. Masotti, and A. Costanzo, "Design of a miniaturized omni-directional rf-to-dc ir-wpt," in *2018 IEEE Wireless Power Transfer Conference (WPTC)*, 2018, pp. 1–4.

[44] F. Benassi, D. Masotti, and A. Costanzo, "Engineered and miniaturized 13.56 mhz omni-directional wpt system for medical applications," in *2019 IEEE International Conference on RFID Technology and Applications (RFID-TA)*, 2019, pp. 306–309.

The author of this Thesis has developed the work presented in [43] under the supervisor of Dr. Alex Pacini, and her contributions have regarded the full-wave simulations of the WPT system together with the circuital optimization. For what concerns the design of [44], the author of this Thesis has been the main contributor.

2.1 Introduction

This Chapter describes the design and experimental validations of a wireless power transfer system, operating at 13.56MHz, with the main goal of achieving quasi-constant power reception of the receiver side, regardless the mutual RX rotation in the 3D-plane. This system is thought to be applied in the biomedical field for the powering of implantable devices whose positions are generally unknown. This rotation insensitivity overcomes an important problem of performance degradation due to TX-RX mutual rotation, a topic that, in literature, has been a constant challenge to tackle.

The idea of powering implantable devices by means of EM waves has been addressed with increasing interest [45]. This approach would provide a safe and less invasive alternative to battery replacements through surgery procedures. Issues related to system reliability are still under investigation, for both near-field (reactive) and far-field (radiative) implementations. This Chapter describes a near-field resonant inductive system operating at 13.56 MHz, designed to be insensitive to any possible 3-D rotation of the receiver, which are usually unknown. Moreover, optimizations have been conducted to achieve a reasonable efficiency with a miniaturized receiver, having a volume of the order of a cubic centimetre. Previous attempts to solve this problem are available in the literature [46], [47], but characteristics such as miniaturization and omni-directionality, necessary

for implantable devices, have not been fully achieved yet. Indeed, most proposed links are designed assuming a known receiver position, rarely taking into account possible rotations or misalignments. In fact, during coil rotations, the shared flux varies drastically and consequently the output power and voltage. A successful attempt to reduce energy transfer fluctuations, when powering a small implant, has been recently demonstrated in [48], but considering a rotation only in a 2-D plane. Moreover, in [48], the receiver diameter is larger, the working frequency lower (6.78 MHz), but a comparable efficiency can be achieved. In this Chapter, a 3-D miniaturized RX is exploited to realize a quasi-constant dc-output voltage and power for any possible receiver rotation. Three orthogonal coils are wrapped around a plastic sphere, acting as the capsule; each coil is connected to its own optimized class-E rectifier and the three dc outputs are series-connected. This solution allows for a reduced output voltage ripple for any possible RX orientation, ensuring the continuous powering of the implant. The system design is carried out by means of EM/nonlinear co-simulation [49]. The results demonstrate that the proposed system allows to provide wirelessly at least 2.7 V at 5 cm, measured on optimum load of 2700 Ohm, corresponding to a dc-power of 2.5 mW. According to the state-of-the-art, these values are fully aligned with the implantable devices needs in terms of power and turn-on voltage. The prototype has been realized and a measurement campaign has been conducted.

2.2 Design of the RF-to-dc Wireless Link

The first element to be designed is the TX coil, tuned to operate at 13.56 MHz when excited by a voltage source with a 50 Ω internal impedance. Fig. 2.1 shows the equivalent circuit model of the designed IR-WPT system, Fig. 2.2a depicts the first prototype realized by 3-D printing, whereas Fig. 2.2b displays the dimensions of the 3-D RX coils. This preliminary version of the prototype hosts the rectifiers mounted on pcb and glued on the coils themselves. In the ultimate version, described later in this Chapter, the circuitry is hosted inside the sphere.

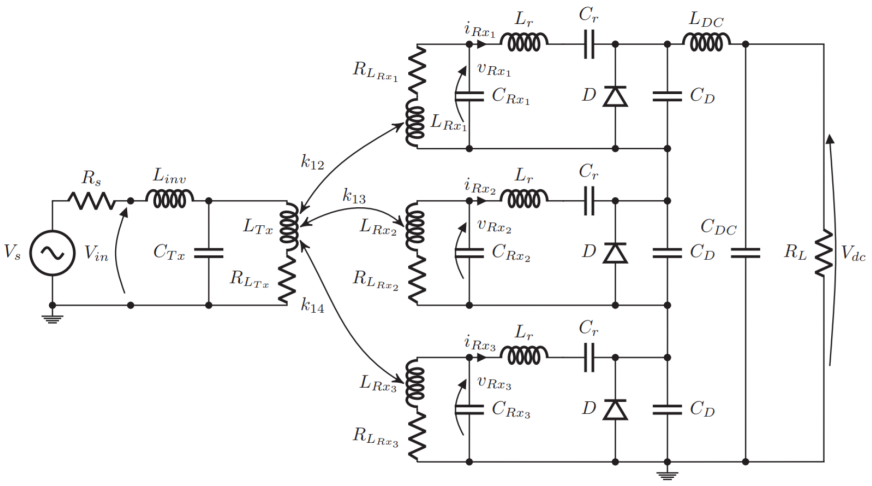

Figure 2.1: RF-to-dc link equivalent circuit. [43] © 2018 IEEE

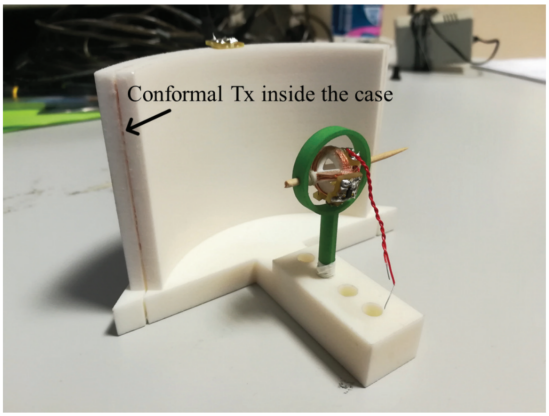

(a)

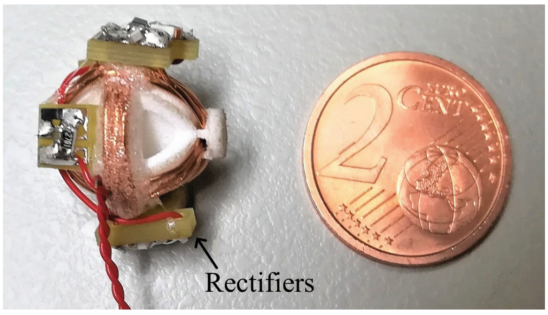

(b)

Figure 2.2: Realized prototype with the 3-D printed holding structures and (b) a comparison between the miniaturized receiver and a 2 euro coin. [43] © 2018 IEEE

2.2.1 Full-wave Characterization of the RF-to-RF Link

A large transmitter is geometrically optimized to maximize the shared flux, thus the kQ [50], in the direction of the miniaturized RX receiver axis and at a reference distance of 5 cm. This value is chosen to be comparable to the distance between the skin and the left ventricular apex or the digestive tract. The optimized geometrical parameters are: h and w_1, chosen in order to obtain a conformal coil suitable to be leaned on the body surface,

as for example on the abdomen. The RX is made of three orthogonal coils that allow a safe power reception regardless the mutual TX-RX position (see Fig. 2.3).

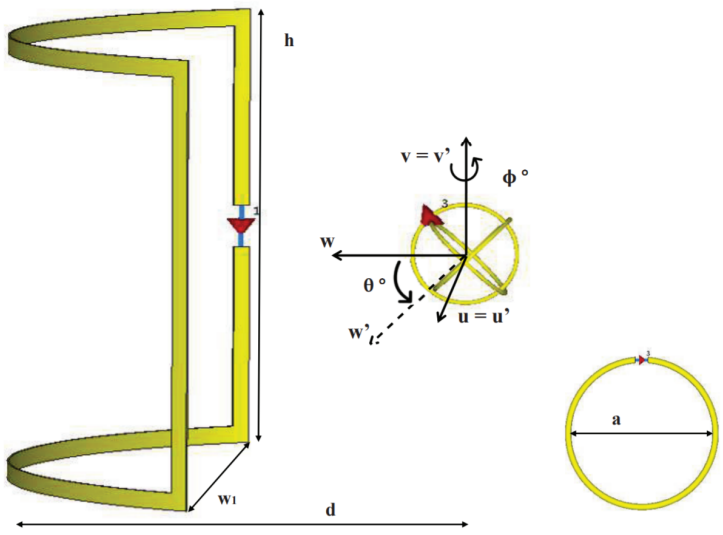

Figure 2.3: Schematic representation of the $\theta - \phi$-rotation angles. [43] © 2018 IEEE

To estimate the RF-to-RF efficiency of this system when experiencing different RX rotations, full-wave EM simulations have been carried out. The full exploitation of the 3-D RX rotations highlights several $\theta - \phi$ combinations, showing different performance. With reference to Fig. 2.3, the TX dimensions are h =52 mm, w_1=100 mm, whereas for the RX coil a =12 mm and the TX-RX operating distance d is set of 50 mm. From full-wave simulations, the equivalent circuit parameters of Fig. 2.1 are derived and the related coupling coefficients are listed in Table 2.1 and Table 2.2 for θ= 45° and ϕ= 60°, respectively.

Although the self-inductances do not vary, the coupling coefficients clearly

Table 2.1: Coupling coefficients for the RF-to-RF link for θ=45°. [43] © 2018 IEEE

ϕ	k_{12}	k_{13}	k_{14}
0	-5.5 x 10^{-3}	-4.82 x 10^{-6}	-4.95 x 10^{-3}
45	-3.48 x 10^{-3}	-5.09 x 10^{-3}	-3.48 x 10^{-3}
90	3.19 x 10^{-6}	-0.707 x 10^{-2}	1.00 x 10^{-5}
135	-3.48 x 10^{-3}	-4.82 x 10^{-3}	3.59 x 10^{-3}
180	5.04 x 10^{-3}	1.94 x 10^{-6}	5.14 x 10^{-3}
225	3.62 x 10^{-3}	4.97 x 10^{-3}	4.97 x 10^{-3}
270	-5.09 x 10^{-6}	0.71 x 10^{-2}	-0.83 x 10^{-6}
315	-3.61 x 10^{-3}	5.09 x 10^{-3}	-3.53 x 10^{-3}

Table 2.2: Coupling coefficients for the RF-to-RF link for θ=60°. [43] © 2018 IEEE

ϕ	k_{12}	k_{13}	k_{14}
0	3.58 x 10^{-3}	-5.22 x 10^{-6}	-6.03 x 10^{-3}
45	-2.488 x 10^{-3}	-5.12 x 10^{-3}	-4.32 x 10^{-3}
90	1.84 x 10^{-6}	-0.71 x 10^{-2}	0.924 x 10^{-5}
135	2.50 x 10^{-3}	-4.94 x 10^{-3}	4.41 x 10^{-3}
180	3.40 x 10^{-3}	-1.00 x 10^{-5}	6.26 x 10^{-3}
225	2.54 x 10^{-3}	4.96 x 10^{-3}	4.41 x 10^{-3}
270	-4.36 x 10^{-6}	0.71 x 10^{-2}	6.75 x 10^{-7}
315	-2.58 x 10^{-3}	5.16 x 10^{-3}	-4.32 x 10^{-3}

show different operating conditions which need to be addressed correctly to avoid unwanted fluctuations of the transferred power. This problem is tackled by the proposed 3-D structure and the rectifiers topologies, which guarantee an almost constant overall TX-RX coupling, regardless the TX

and RX reciprocal orientation.

2.2.2 Design and Optimization of the RF-to-dc Receiver

A proper receiver topology can be realized by connecting each RX coil with its own rectifier and then connecting the dc outputs in series. With this approach, the output voltage "dark-zones" are avoided and fluctuations are strongly reduced. The RF-to-dc conversion is performed by a Class-E rectifier, shown in Fig. 2.1, connected to each receiving coil through an LC-filter, which ensures a sinusoidal input current. The three outputs are then dc-combined and share the same dc-filter, where the inductance L_{dc} provides also a high RF impedance of the dc-combining path. This allows for dividing the PCBs hosting the three rectifiers and thus a free positioning of the dc filter is obtained, without any unwanted spurious RF coupling from the dc line. The equivalent circuit of the transmitter is composed of a 50 Ω voltage source, linked to the resonant TX coil through the inductance L_{inv}: in this way, the RF-to-RF link acts as a transformer, thus obtaining the source load that is proportional to the system load. This solution is suitable for sources with high internal series resistance, as in the case of low-power devices powering. The equivalent circuit of the overall system is then optimized by means of the Harmonic Balance technique. The non-linear regime is described with 7 harmonics (plus dc), with the goals of

maximizing the total efficiency (see Eq. 2.1) while minimizing the output voltage (V_{dc}) variations for any possible rotational angle. The optimization variables are C_D and the dc-load R_L, whose obtained values are 10 pF and 2.7 kΩ, respectively. Finally, to analyze the dynamic behaviour of the proposed system, nonlinear simulations have been carried out with respect to different voltage levels of the source.

2.3 Prototype Realization and Measurement Campaign

A first prototype is designed as shown in Fig. 2.2a. The three-loop coils are wrapped around three 3D-printed orthogonal holding structure that is able to rotate around the 3 axes through a Cardan suspension. The optimized components are listed in Table 2.3

Table 2.3: Circuital optimized values. [43] © 2018 IEEE

Element	**Value**	**Element**	**Value**	**Element**	**Value**
$R_{L_{inv}}$	140 nH	C_{RX_2}	890 pF	C_{RX_3}	890 pF
L_{T_x}	322 nH	C_{T_x}	430 pF	$R_{L_{TX}}$	200 mΩ
L_{RX_1}	155 nH	$R_{L_{RX_1}}$	100 mΩ	L_{RX_2}	155 nH
$R_{L_{RX_2}}$	100 mΩ	L_{RX_3}	155 nH	$R_{L_{RX_3}}$	100 mΩ
C_{RX_1}	890 pF	L_r	140 nH	R_{L_r}	20 $m\Omega$
C_r	1 nF	f	13.56 MHz	D	HSMS2822
C_D	10 pF	L_{DC}	22 μH	$R_{L_{DC}}$	20 mΩ
C_{DC}	20 μF	R_L	2700 Ω	R_s	50 Ω

The proposed 3-D RX configuration allows for achieving a limited dc-voltage fluctuation, with values always above 2.7 V, for a voltage source of 10 V. For any orientation in 3-D a dc-power of at least 2.5 mW is obtained, value that is usually sufficient to power an implant [45]. For a 10 V-source, the current flowing into the transmitter is around 4 mA, therefore the magnetic field in proximity of the receiver is quantified to be around 0.018 A/m, which is in compliance with the ICNIRP guidelines. In Fig. 2.4a the overall efficiency η_{TOT} is plotted for various $\theta - \phi$ rotations and computed starting from the simulated results and defined as in [51]:

$$\eta_{TOT} = \eta_{RF-RF} * \eta_{RF-dc} = \frac{P_{dc}}{P_{in}} \tag{2.1}$$

with:

$$\eta_{RF-RF} = \frac{P_{RX_1} + P_{RX_2} + P_{RX_3}}{P_{in}} \tag{2.2}$$

$$\eta_{RF-dc} = \frac{P_{dc}}{P_{RX_1} + P_{RX_2} + P_{RX_3}} \tag{2.3}$$

and

$$P_{RX_i} = Re\left\{\frac{v_{RX_i} i^*_{RX_i}}{2}\right\} \; with \; i = 1,2,3 \tag{2.4}$$

where P_{in} is the RF power entering the TX coil, approximately 20 mW, and P_{dc} is the power delivered to the RX load. Fig. 2.4b shows the corresponding dc-output voltage levels for any possible azimuthal and longitudinal rotation. Finally, Fig. 2.5a considers a reference RX configuration, with (θ, ϕ) = (45°, 45°) and plots the efficiency with respect to different voltage values of V_{in}. As can be inferred, when V_{in} exceeds the diodes threshold (around 1.5 V), the performance strongly improve, while if V_{in}

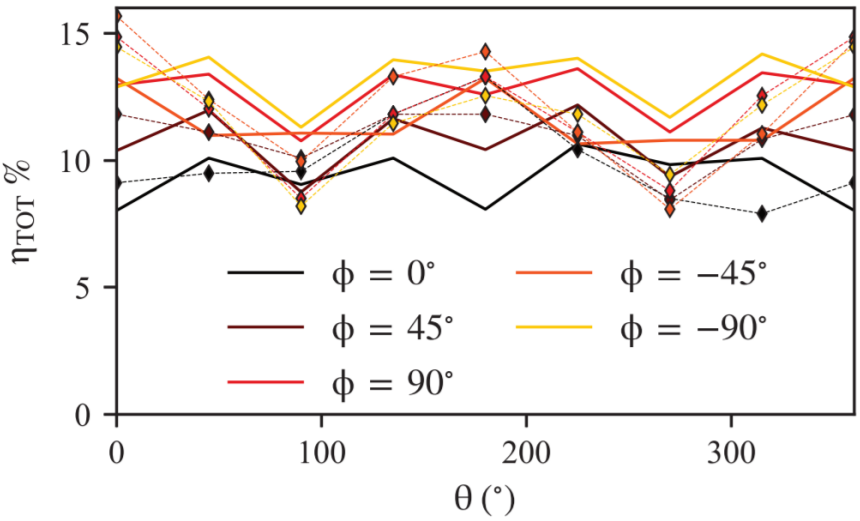

(a)

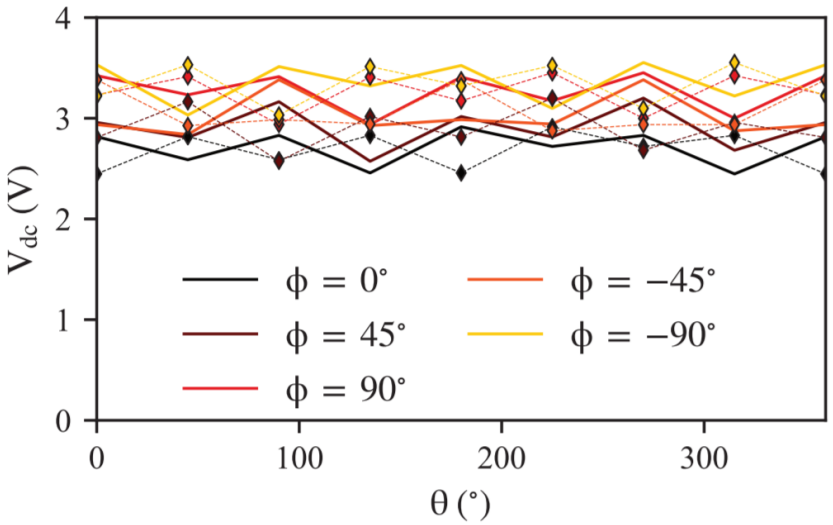

(b)

Figure 2.4: (a) total efficiency (η_{TOT}), (b) dc-output voltage (V_{dc}). Both are relative to $V_s = 10$ V. Measured data are plotted using diamonds. [43] © 2018 IEEE

is above 10 V, improvements are reduced due to the diodes nonlinear behaviour. On the other hand, when higher source voltages are applied, the rectifiers input impedance has no significant variations and the efficiency is maximized, according to kQ [52]. In the same figures, the preliminary

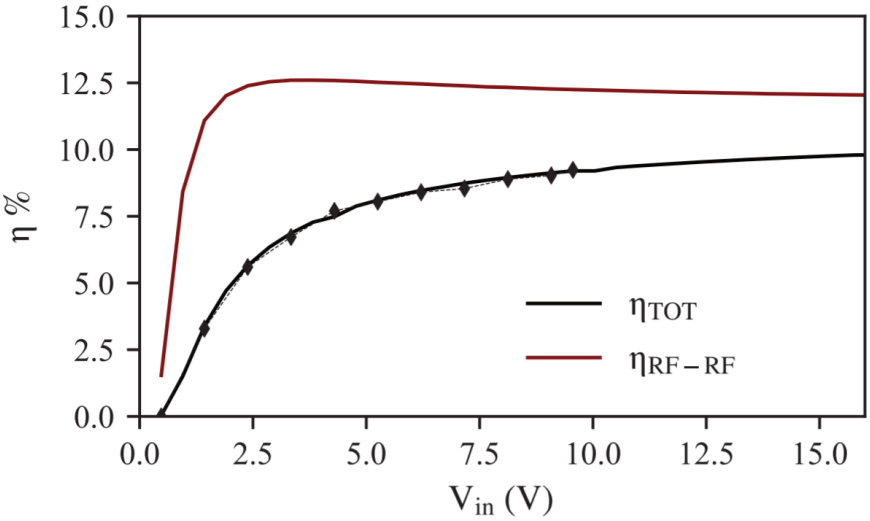

(a)

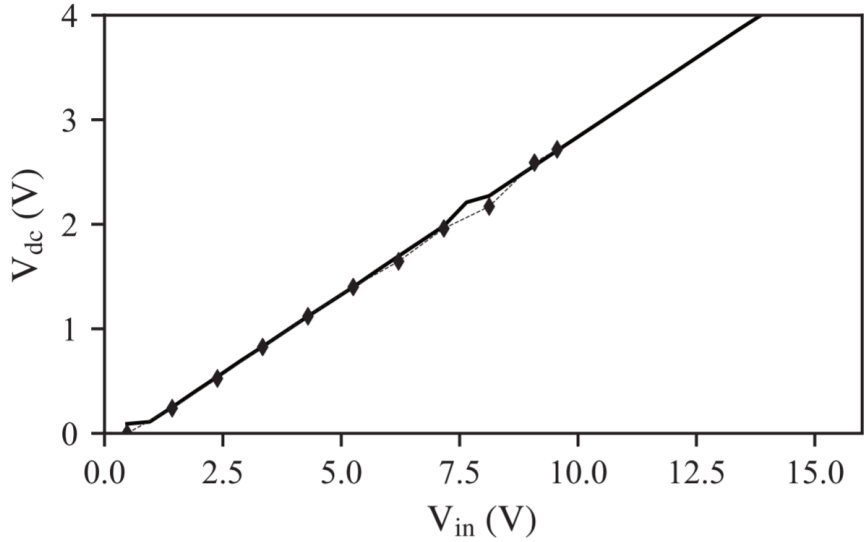

(b)

Figure 2.5: Simulated (lines) and measured (dots) values of the η_{tot} , (b) simulated and measured dc-output voltage. Both graphs are plotted with respect to different V at $(\theta, \phi) = (45°, 45°)$ and $d = 5$ cm. [43] © 2018 IEEE

measurement results are superimposed and compared with the predicted ones, confirming the accuracy of the design procedure.

2.4 Improved Compactness and Optimization

The previously-described solution aims to be a proof-of-concept of a WPT system that is minimally sensitive to the rotation of the receiver in the 3-D plane. Under a realization point of view, the system lacks of compactness and the presence of the PCB attached to the receiving coils not only contributes to increase a little the overall encumbrance of the system, but also causes a degradation of the RF-to-dc Power Transfer Efficiency, compared to the simulations, due to a shield effect which affects the EM coupling.

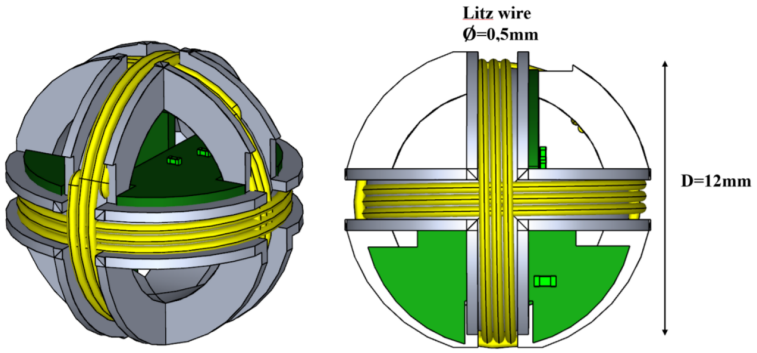

Figure 2.6: 3-D rendering of the three coils wrapped around the holding structure hosting the circuitry. [44] © 2019 IEEE

For this reason, an optimized and miniaturized structure for hosting the rectifier circuits has been realized under the constraint of maintaining a maximum overall encumbrance equal to the volume of the RX sphere, as schematically shown in Fig.2.6. In order to free the RF-channel between

the TX and RX coils, the PCBs need to be inserted inside the sphere volume: this operating choice removes the disturbing effects, but introduces challenges on the physical and mechanical realization, due to the small available volume, which is less than 1 cm^3. In order to fit all the circuitry in the most efficiency way, the printed circuit boards are designed separately: in particular, the first one hosts two of the three rectifiers, and the second only hosts one rectifier and the low-pass filter. This choice allows to connect each coil to its own rectifier and exploiting a 2-D arrangement, as Fig.2.6 shows. When designing the inductive link, the radius of the receiving coils has been set to 6 mm which leads, excluding a thin 3D-printed structure, to have an available internal diameter of about 10 mm for placing the PCBs. These reduced dimensions limit the PCB design characteristics in terms of thickness, width and positioning, thus the choice of the SMD components packages and connections is of a paramount importance. Due to the three-dimensional arrangement of the system, having only one double-layered PCB for the entire circuit has been a discarded option. For this reason, two separated PCB have been designed and placed orthogonal to each other: one hosts a coplanar connection with two of the three receiving coils wire and the second hosts a single coil connection and its related circuitry. As previously described, the outputs of each rectifier are series connected by means of a combination between copper wires and via holes.

The proposed boards are shown in Fig. 2.7 together with a schematic

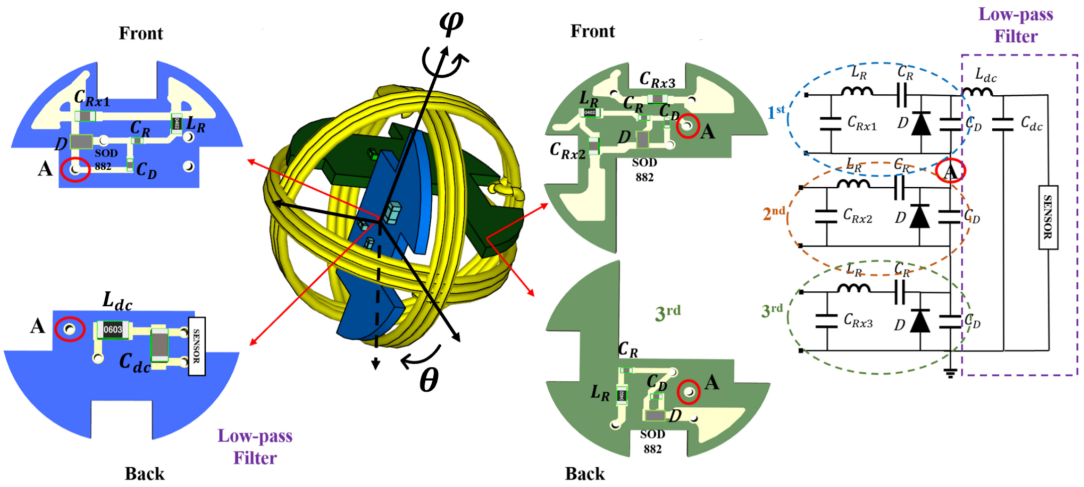

Figure 2.7: Detailed description of the two orthogonal PCBs to be placed inside the plastic sphere. [44] © 2019 IEEE

representation of their arrangement inside the holding spherical structure. The first PCB hosts one rectification circuit on the front and one on the back, whereas the second one, placed on the left-hand side of the picture, has the rectifier on the front and the low-pass filter and dc-output on the bottom layer. As described in the figure, several via holes are exploited to connect both sides of the circuitry within the same board, whereas the two board are linked by means of a copper wire in proximity of the node highlighted with the letter "A" in the schematic. This configuration is a direct consequence of the system dimension constraints, leading the boards to be placed orthogonally to each other to efficiently design the structural arrangement. Moreover, the PCBs have to be provided with some anchors in order to be stably fixed and ease the connections with each coil: in fact the 3D-printed structure is designed as three orthogonal trails, whose thickness can be exploited as hooking for each coplanar PCB. The boards

are designed using a Rogers RO4360G2 substrate (ε_r= 6.15, thickness= 0.610 mm), allowing to slightly reduce the board thickness, comparing to a standard FR-4 substrate.

2.5 Simulation Results Accounting for Biological Tissues

After reducing the PCB dimensions and choosing the appropriate components, the circuitry is re-optimized by means of Harmonic Balance algorithm. The SMD components are chosen in order to minimize the overall encumbrance of both PCBs, in particular 0201 packages are preferred with respect to slightly bigger ones. Diodes have been changed from the previous version [48]: SMS3922 Schottky diode, provided with a smaller package, the SOD-882, were found to be more suitable to achieve circuital miniaturization. The circuital design and optimization account for the real component models and they are conducted with the aim of maximizing the $\eta_{RF-to-dc}$ at a reference distance of 5 cm, rather then maximizing the dc-output voltage. The optimized components values are reported in Table 2.4.

The coupling factors to be imported in order to create the equivalent circuit model are derived by a full-wave simulations and reported in Fig. 2.8. In particular, the plot shows k_{12} and k_{13} for two different reference distance: 5 cm and 4 cm, whereas k_{14} is not reported due to its low value in this specific case.

Table 2.4: Optimized values of the circuital components. [44] © 2019 IEEE

Component	**Value**	**package**
C_{RX_1}	750 pF	0402
C_{RX_2}	750 pF	0402
C_{RX_3}	750 pF	0402
C_R	1 nF	0201
D	SMS3922-040LF	SOD-882
C_D	10 pF	0201
L_{DC}	22 μ H	0603
C_{DC}	33 μ F	0603

The simulated $\eta_{RF-to-dc}$ efficiencies are in agreement with the coupling

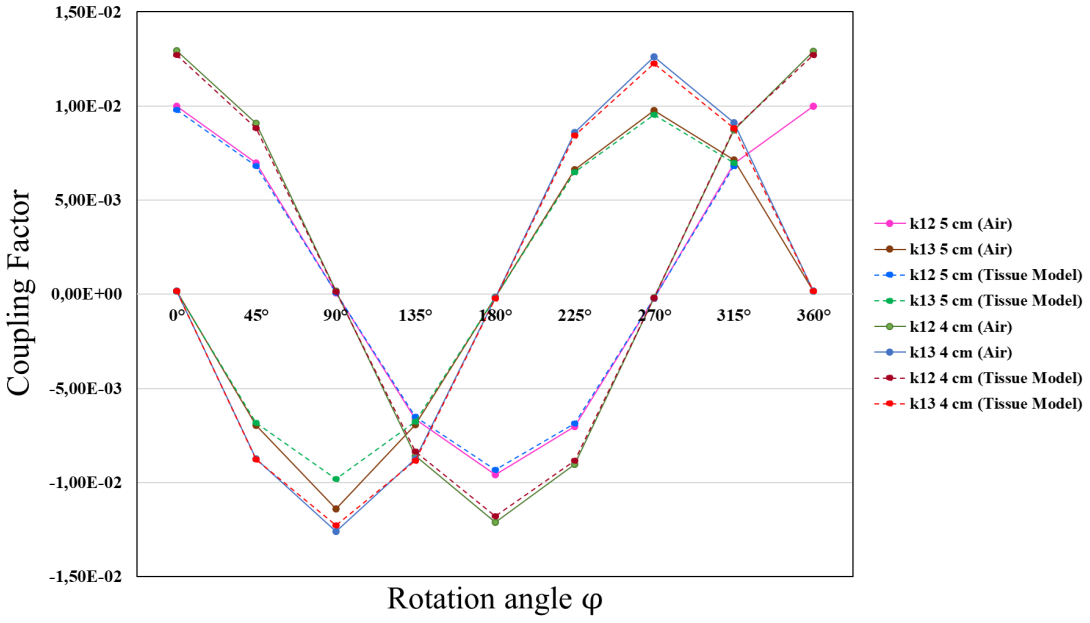

Figure 2.8: Coupling coefficients for different TX-RX distances with or without interposed biological tissues. [44] © 2019 IEEE

factors shown in Fig. 2.10, confirming the dependency of the $\eta_{RF-to-dc}$ from the kQ-product [53]. Furthermore, in order to quantify the attenuation due

to a biological tissue environment, an equivalent model of human tissues is created and interposed between the transmitter and the receiver. In particular, dielectric properties of each tissue are derived from [54] and the exact dielectric properties in correspondence to the operating frequency of 13.56 MHz are listed in Tab. 2.5.

Table 2.5: Dielectric properties of the tissues layers @13.56 MHz [54].

Tissue	ε_r	σ
Muscle	138	0.628 S/m
Fat	25.4	0.0553 S/m
Skin	285	0.238 S/m

The dielectric slab used to perform full-wave simulations is realized by means of concentric cylinders, in particular this geometry is used to mimic a stack of different tissue: 25 mm of muscle, 5 mm of fat and 5 mm of dry skin respectively, as shown in Fig. 2.9.

The above-mentioned results presented in Figs. 2.10, Fig. 2.11, and Fig. 2.12 are calculated for a TX-RX distance of 5 cm and 4 cm in the two conditions: with the TX-RX simulated in air and inside the biological environment.

As shown in the graphs, the system performs comparable output values for the two different simulation environments. This highlights that the presence of the human body does not drastically influence the EM coupling, thus the total Power Transfer Efficiency (PTE). If the distance decreases

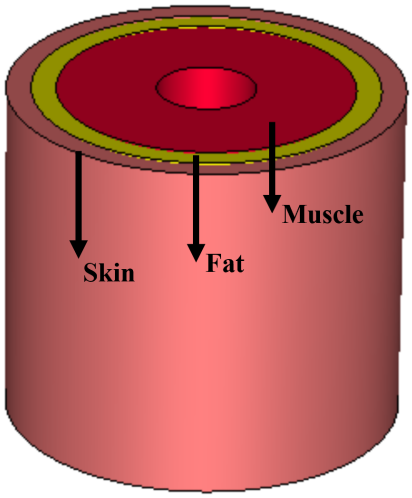

Figure 2.9: Pictorial representation of the three cylinders mimicking the stack of biological tissues.

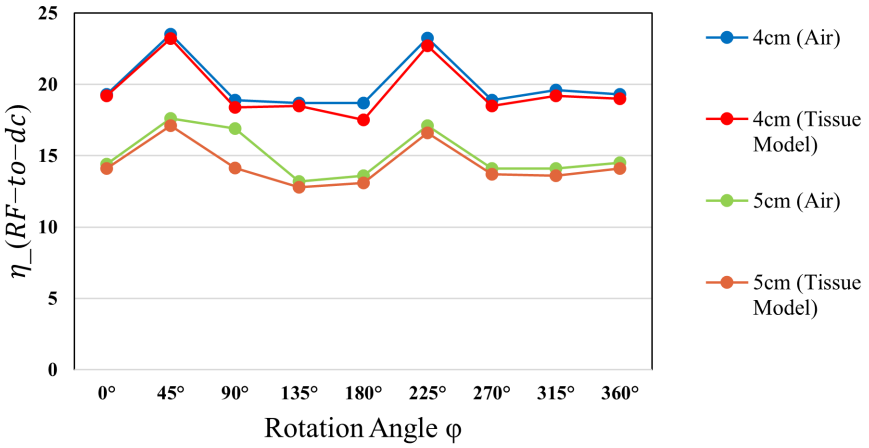

Figure 2.10: $\eta_{RF-to-dc}$ for different TX-RX distances with or without interposed biological tissues. [44] © 2019 IEEE

the $\eta_{RF-to-dc}$ efficiency increases to an averaged value of 20 % corresponding to a received power of 3.5 mW. The three rectified dc-outputs are series connected in order to avoid dark zones during the rotation around each $\theta - \phi$ combination. In fact, if the output voltage of each coil is measured

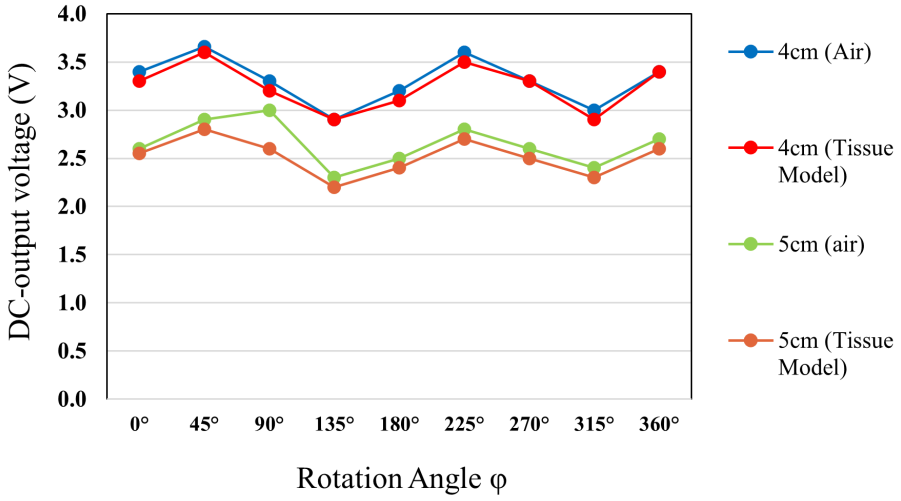

Figure 2.11: Dc-output voltage on the dc-load for different TX-RX distances with or without interposed biological tissues. [44] © 2019 IEEE

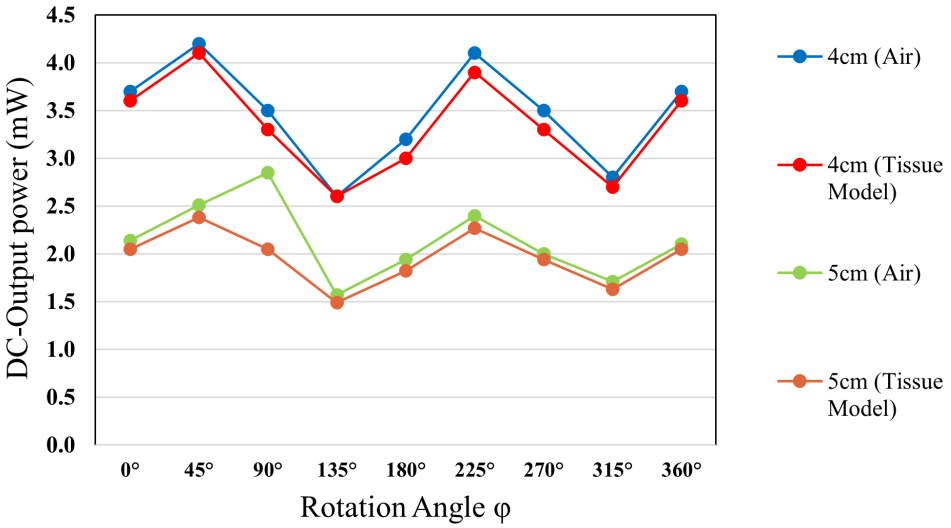

Figure 2.12: Dc-output power on the dc-load for different TX-RX distances with or without interposed biological tissues. [44] © 2019 IEEE

separately with respect to a ϕ-rotation, each coil alternates a symmetrical behaviour of on-off states, thus making the rectified outputs strictly

dependent on the instant position.

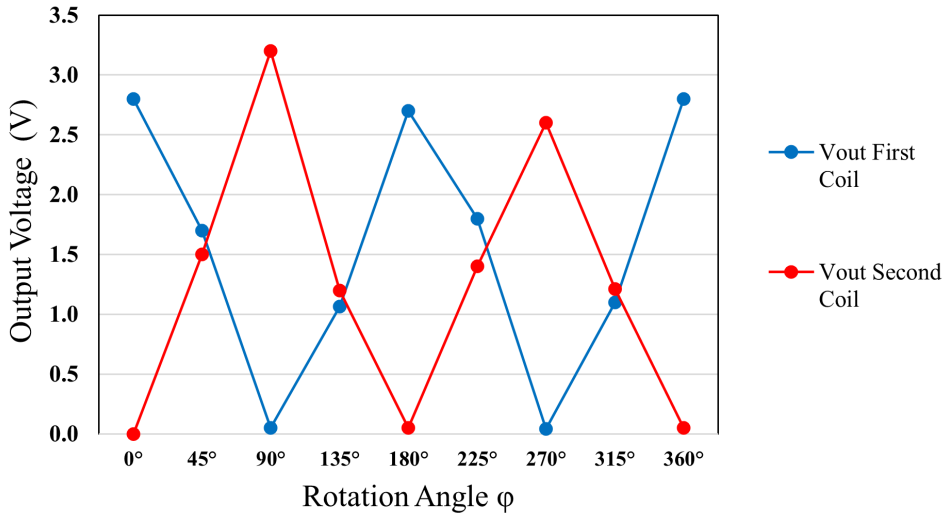

Figure 2.13: Rectified voltage on each coil for a 360°-ϕ rotation in air. [44] © 2019 IEEE

In particular Fig. 2.13 describes the rectified voltage for two of the three coils separately for a 360°-ϕ rotation, considering no rotation around θ. The first and second coil have a complementary behaviour and the third one presents almost zero-output voltage value due to its position with respect to the transmitter; in fact this coil is positioned orthogonally to the transmitter which causes an EM coupling close to zero and thus no inducted voltage.

To investigate the compliance of this implementation with the safety guidelines [55], the Specific Absorption Rate (SAR) has been calculated and a value averaged on 10g of tissues has been considered. The results show that the obtained value of 0.0027 W/Kg, for a 0.5 W power provided to the transmitter, is below the safety limits (2 W/Kg) and the distribution

is shown in Fig. 2.14.

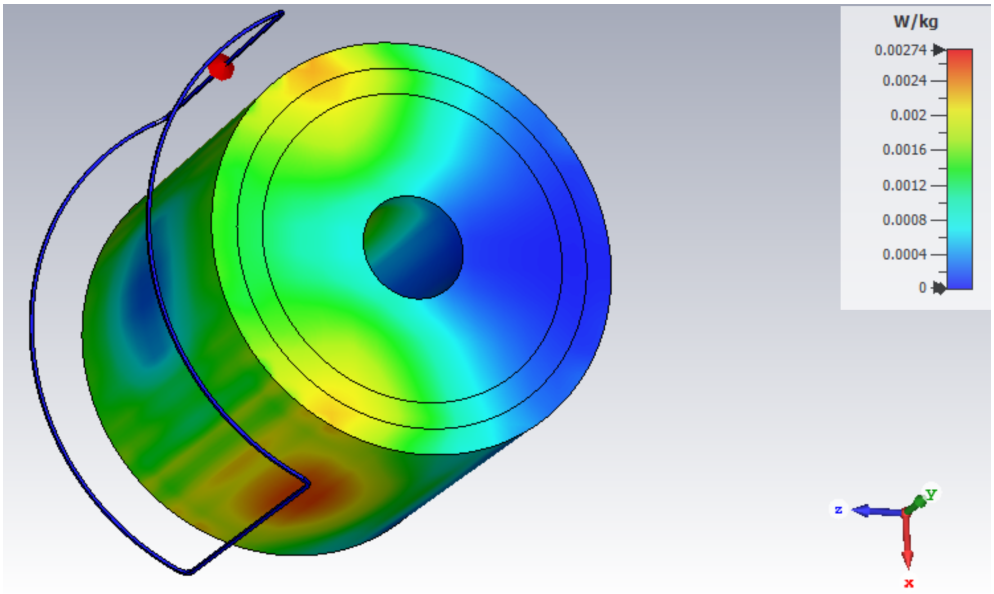

Figure 2.14: Specific Absorption Rate (SAR) distribution.

3. Energy-autonomous Filtenna for Ethanol Detection

This Chapter is based on the following articles:

[56] F. Benassi, N. Zincarelli, D. Masotti, and A. Costanzo, "A wearable passive microwave fluid sensor wirelessly activated," in *2019 IEEE Wireless Power Transfer Conference (WPTC)*. IEEE, 2019, pp. 236–240.

[57] F. Benassi, G. Paolini, D. Masotti, and A. Costanzo, "A wearable flexible energy-autonomous filtenna for ethanol detection at 2.45 ghz," *IEEE Transactions on Microwave Theory and Techniques*, 2021.

The author of this Thesis has been the main contributor of the above-mentioned articles, carrying out both the full-wave simulations and the circuital optimization of the entire sensor that has been preliminary described and presented in [56], and subsequently optimized in [57]. The measurement campaign described in [57] have been performed by the first two authors of the article.

3.1 Introduction to Microfluidic Sensors

This Chapter aims at describing the research activity carried out in the field on microwave fluid detection, describing the design of an energy-autonomous wearable filtenna (filtering antenna) for the detection of ethanol-based solutions. This project aims to exploit the operating principles of wireless power transfer in a biomedical environment, to realize a design able to passively detect the presence of a specific substance on the skin surface, in this case, the presence of ethanol-based solutions which are the main components of common hand sanitizers. The main novel characteristics that have been introduced are the complete energy autonomy of the system and the design which does not impose a laboratory setup to perform the filling of the microfluidic channel with the fluid under test.

In recent years, the need for finding alternative methods to substitute physical or chemical transduction has led to identify microwave dielectric spectroscopy as a valid candidate, in particular in situations where the use of biological marker is not a necessary requirement [58]. This implies a drastic reduction in the use of chemical products as reagents and solvents with also a considerable decrease in operational time. Microwave transduction is considered a valid procedure to analyse not only biological liquids but also smaller molecules up to cell-level and guarantee a quick e non-destructive biological characterization. The basic operating principles rely

on the interaction of microwaves with the biological matter and the correlation between the variation of dielectric permeability and permittivity and the different type of tissue or cell that is analysed and characterized. Such approach can find several applications scenarios and be a breakthrough for the early diagnosis of severe diseases [59]. The proposed project involves a detector that can be applied in medical environment to perform the detection of certain solutions, in particular of ethanol-based ones which are the main component of common hand sanitizer. The up-mentioned operating principles can also be applied in a reverse way: the main purpose is not to analyse the effect of EM waves on the dielectric properties of the fluid, but to exploit the effect of its presence within a resonant structure as a material causing a variation on the properties of the hosting structure, thus causing a shift on its resonant frequency. Several applications have already exploited these principles to create sensors based on microwave resonant structures which can be realized using interdigitated capacitors, as in [60]. The article describes a broadband system for dielectric spectroscopy operating in the 0.5-3 GHz frequency range and dedicated to the detection of organic chemicals. Fig. 3.1 describes the sensing element realized using an interdigitated capacitors, able to generate a frequency dependent model related to the single tested fluid. As expected, the sensing capacitance is directly proportional to the fluid $\varepsilon_r'(\omega)$, whereas the resistance behaves as $1/\varepsilon_r''(\omega)$. The detection readout is performed by reading the voltage level

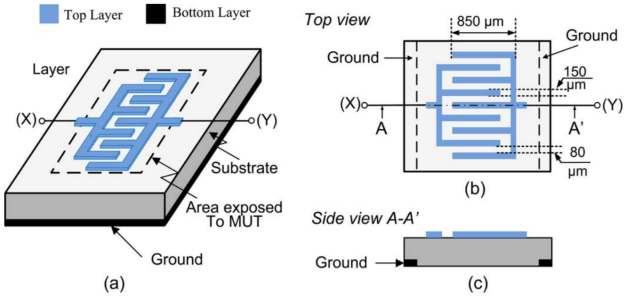

Figure 3.1: (a) schematic representation of the sensing interdigitated capacitor and (b) side views and dimensions. [60] © 2013 IEEE

variations across the interdigitated capacitor when a certain fluid is under test. The analysis of voltage amplitude and phase variation is carried out by quadrature down-conversion mixer together with detection algorithms [60]. Microwave dielectric spectroscopy con be performed not only by means of interdigitated capacitors structures [61–64], but other topologies of microwave resonator can also be exploited. In [65], a T-resonator embedding a varactor is used to detect the presence of different fluids within the microfluidic channel. The varactor is placed within a 2.4-GHz T-stub resonator in such a way that the dielectric properties of the fluid change the electrical length of the stub and thus its resonant frequency. The fluids under test are provided to the sensing area through a microfluidic channel filled by small pipes, as shown in Fig. 3.2. The tested fluids vary from plain water, to ethanol-based solutions, exanol, exanol-ethanol solutions, showing how all these combinations are responsible for exposing the varactor to different dielectric properties and this causes a shift in the T-resonator resonant frequency, which can be clearly read by measuring the transmis-

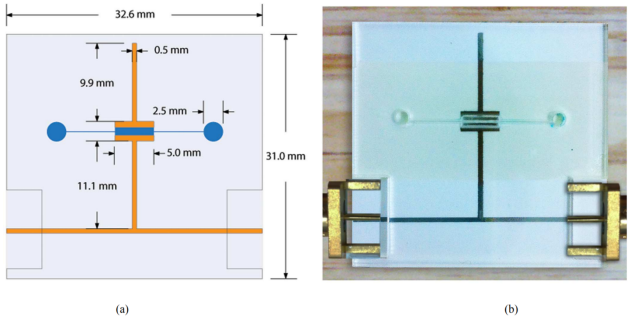

Figure 3.2: Schematic representation of the T-resonator embedding the varactor and the microfluidic channel. [65] © 2013 IEEE

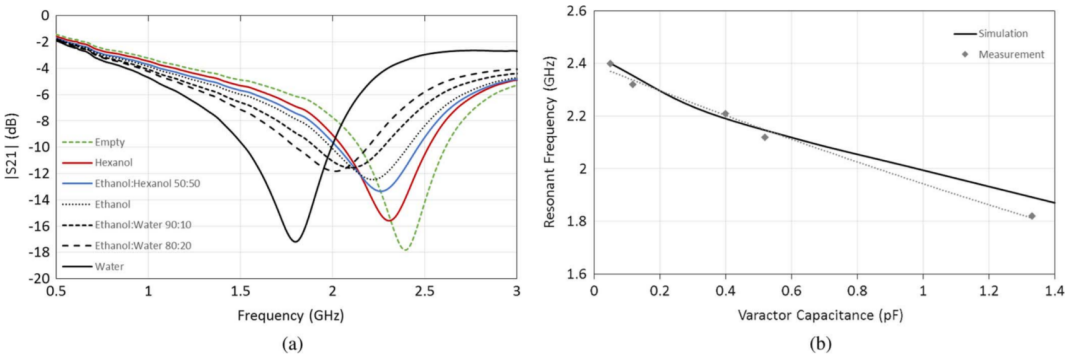

Figure 3.3: (a) measured transmission coefficient of the T-resonator when different fluids are interchanged in the channel (b) side views and dimensions. [65] © 2013 IEEE

sion coefficient of the 2-port system. Moreover, an impedance model has been exploited to model the varactor during simulations in order to reduce the computational time. This model has allowed to correlate the values of the capacitance for the obtained different resonant frequencies. Results are shown in Fig. 3.3(a) and (b).

One practical common thread linking all these presented solutions is the fact that the experimental validations are conducted in laboratory environments and the fluids are provided with the help of small pipes. For wearable solutions, both the sensing and the readout need to be performed without

using cables, since one of the key feature of IoT technology is lightness, especially when dealing with portable wearable devices. This has been the key point from which the design of the detector described in this Thesis has started.

3.2 Batteryless Wearable Filtenna: the Microfluidic Stub Resonator

Lightness, wearability, reusability and energy autonomy are the main characteristics of the presented wearable filtenna for ethanol detection. The preliminary idea behind the realization of this structure has been the possibility to detect passively the presence of ethanol-based solutions on the hand skin to validate a correct hand sensitization procedure. The device aims at identifying the presence or the absence of the target fluid, in a scenario in which ethanol-based solutions are expected to be used, in order to exclude ambiguity in the detection. The system is thought to be completely passive and energized by an external power source working at the operating frequency of 2.45 GHz. For system wearability, the grounded microwave technology has represented the most suitable choice. A Rogers RT/duroid 5880 ($\varepsilon_r = 2.2$, $\tan\delta = 0.0009$), with a thickness of 0.508 mm, has been chosen due to its flexibility which has eased the implementation of a solution to be wrapped around the wrist, as shown in Fig 3.4, as well as for its performance when used in the microwave range.

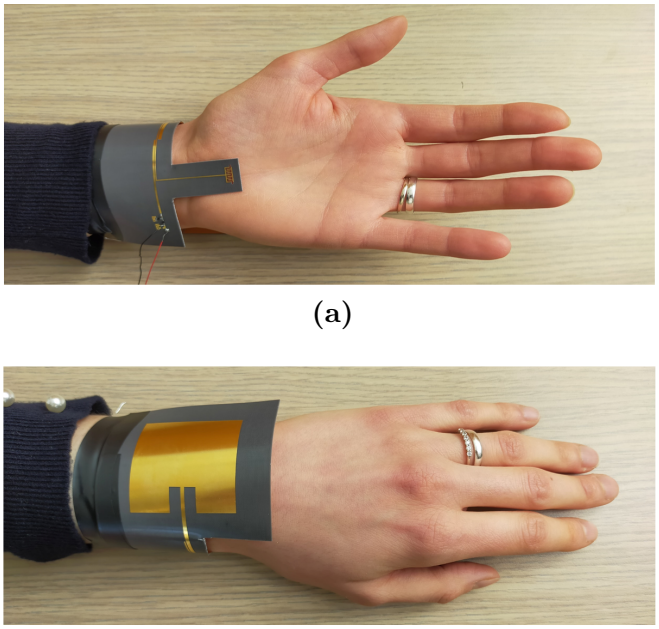

(a)

(b)

Figure 3.4: (a) front and (b) back view of the detector when worn as a bracelet. [57] © 2021 IEEE

To perform the detection, the ethanol-based solution needs to fill a specific part of the system called "microfluidic channel". Its dimensions have been chosen in order to enable the solution to completely fill the channel easily while worn as a bracelet, during hand sanitation procedures. Moreover, the meandered shape has allowed to increase the sensitivity of the detection with respect to its preliminary version presented in [56], while keeping a relatively small encumbrance. The microfluidic channel has been dug in the substrate in such a way that each finger has metallized bottom and top layers while the depth is made of Rogers, as shown in Fig. 3.5.

The microfluidic channel is placed on top of a planar microwave stub resonator and tuned to operate as an open circuit at 2.45 GHz when the

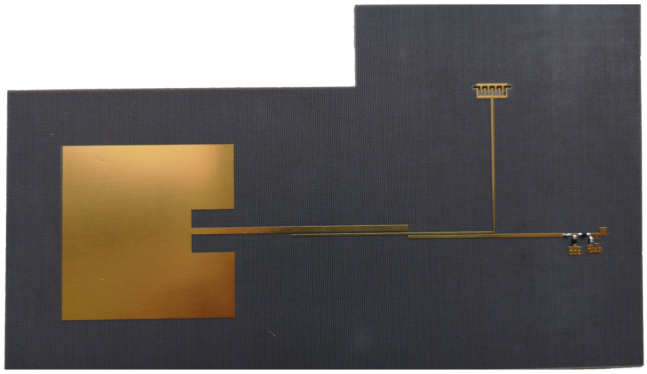

(a)

(b)

Figure 3.5: Realized prototype of the designed filtenna: (a) front view hosting the filtenna and rectifier, and (b) back view with a close-up on the microfluidic channel. [57] © 2021 IEEE

channel is filled with a target fluid: an ethanol-based solution made of 70 % ethanol and 30 % water. It has to be noticed that it is really important to tune the system when the target solution is present in the microfluidic channel because its dielectric properties contribute to define the stub electrical length, which is strictly correlated to its resonance frequency. Once tuned, since the detector needs to be able to identify the presence of the searched solution, other three fluids are tested: water, simulating the evaporation of the ethanol component within the solution, an empty channel, to mimic the total absence of fluid in the channel, and sweat to monitor

possible false detection when placed on the body surface.

As expected, the different dielectric properties of those three fluids, reported in Table 3.1, result in a variation of the stub electrical length and thus in a consequent shift in the resonant frequency.

Table 3.1: Fluids dielectric properties at 2.45 GHz. [57] © 2021 IEEE

Fluid	ε_r	$\sigma(S/m)$
Water-ethanol 70%	30	2.18
Water	77.2	1.28
Air	1	0

The shifts occurring when the fluids are interchanged are represented in Fig. 3.6 in terms of real and imaginary part of the stub input impedance.

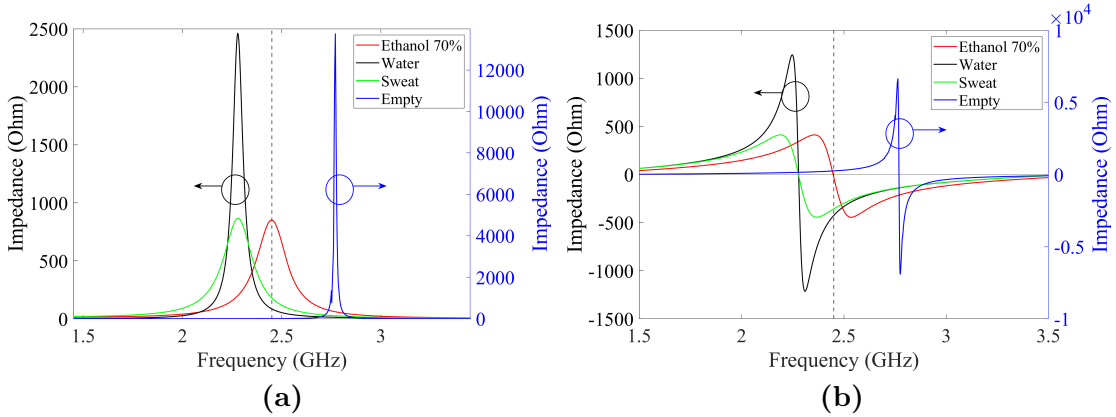

Figure 3.6: (a) real and (b) imaginary part of the stub input impedance for different fluids filling the microfluidic channel. [57] © 2021 IEEE

As it can be noticed, the presence of sweat does not influence the correct identification of the ethanol solution. This can be justified by the capacitive nature of the resonator itself: in fact, the performance are not affected by

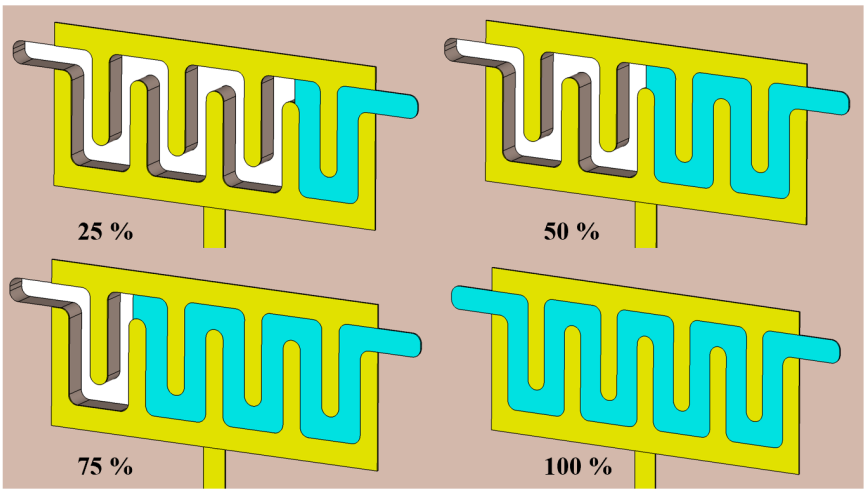

Figure 3.7: Pictorial representation of the different filling percentages of the microfluidic channel. [57] © 2021 IEEE

the variation of the fluid conductivity but mainly by the variation of the relative dielectric constant ε_r. In order to mimic sweat inside full-wave simulations, authors have considered the use of salted water, thus a result similar to the black curve is shown, albeit with a lower peak due to the higher losses with respect to plain water.

Although the reduced overall dimensions of the microfluidic channel would imply a safe complete filling of the channel with the tested fluids, investigation on the effects on the stub resonant frequency for different filling percentages has been conducted, for the sake of completeness. The ethanol-based solution has been used to conduct the simulations and the results have demonstrated the necessity of having a complete filled channel to perform a correct detection. The different filling percentages are divided into four cases: from 25% to 100% filling, as shown in Fig. 3.7. The sim-

ulated real and imaginary part of the stub input impedance have shown that for lower filling percentage, i.e. for a 25%, the resonant frequency is mainly shifted towards the one experienced in the case of an empty channel, whereas, when the filling percentage increases, the resonant frequency moves towards the expected in case of ethanol-based solutions. Due to the overall reduced dimensions of the microfluidic channel a complete filling is expected to be easily achieved thus all the following simulations are carried out under this assumption.

3.3 Design of RF-Selective Output Coupler

Once the resonant stub has been tuned, it needs to be embedded within the linear subnetwork of a rectenna system in order to be activated wirelessly and perform a correct detection. The rectenna is made of a patch antenna operating at 2.45 GHz and a rectifier to perform signal transduction. Among the several antenna topologies, patch-antennas are suitable to be applied in wearable applications due to the background plane that enables a decoupling and avoids unwanted detuning when placed close to the body surface, or, as in this case, attached to it. The full-wave rectifier has been designed to perform signal transduction and enable a safe readout of the channel content based on the dc-output voltage level. In particular, for a fixed received power level, the detector showed the highest dc-output voltage level when the channel is filled with the target ethanol-based solu-

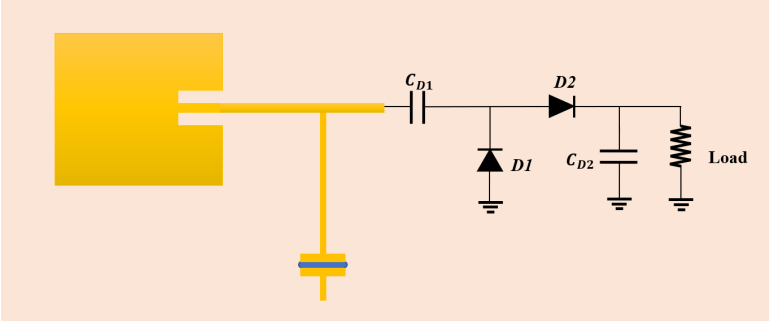

Figure 3.8: Schematic representation of the simulated rectenna with the T-resonator. [57] © 2021 IEEE

tion, whereas for the other cases it shows lover values. To perform that, the most efficient power transmission needs to occur when the ethanol solution is filling the microfluidic channel. In this scenario, at the operating frequency of 2.45 GHz, the stub behaves as an open circuit (not ideal due to the losses), thus this characteristic can be exploited to create a subnetwork layout that enables the maximum power transfer. A preliminary version of the linear subsystem has accounted for a simple and quite intuitive T-connection, as shown in Fig. 3.8. Ideally, when working at 2.45 GHz, the stub branch offers a high impedance only when the channel is filled with the ethanol solution, allowing the 2-port system to provide high value of transmission coefficients. When the channel is empty or hosts water the T-branch offers lower values of input impedance allowing part of the signal to flow into it and worsening the overall transmission coefficient S_{21}. Although this layout would have implied having reduced dimensions of the overall system, it has shown no capabilities to differentiate the dc-output voltage of the three main tested fluids: ethanol solution, water and the case

of an empty channel. The overlapping values of the dc output are shown in Fig. 3.9a. To investigate the main causes of this inaccurate results, the T-resonators S-parameters have been evaluated considering for simplicity a value of 50 Ω as input and output ports. The transmission coefficient S_{21} is displayed in Fig. 3.9b and its clearly visible how the structure does not allow to discriminate the fluids.

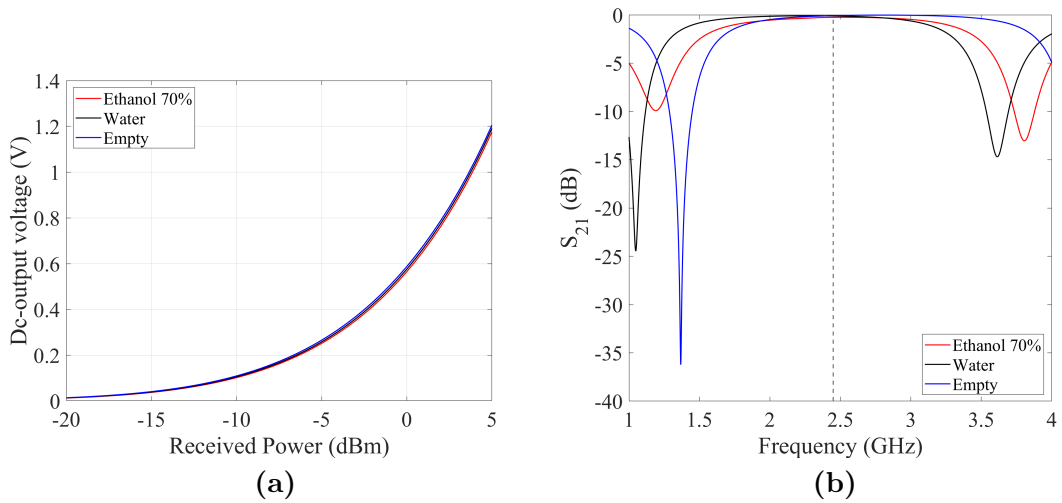

Figure 3.9: (a) dc-output voltage of the three testes fluids and (b) transmission coefficient of the T-resonator. [57] © 2021 IEEE

To overcome this lack of frequency selectivity and perform an electrical decoupling between the antenna and the linear subnetwork embedding the stub resonator, a second-order coupled-line filter is implemented. In particular, the band pass filter is realized using open-end coupled lines and it is tuned to operate at 2.45 GHz when 50-Ω input and out ports are considered. The second-order open-end coupled-line filter is realized using the same RT/duroid 5880 substrate, to again ease compactness of the overall

structure and the length of each section is about $\lambda/4$, which for the operating frequency and substrate dielectric properties corresponds to about 20 mm [66]. Since the filter is directly connected to the patch antenna the characteristic impedance (Zc) of each section must be equal to the one of the patch antenna feeding line, thus 50Ω. For a preliminary investigation the filter has been made symmetrical, every section has the same line width equal to a characteristic impedance of 50Ω.

The purple line in Fig. 3.10 shows the stand-alone filter S-parameters after the tuning to resonate exactly at 2.45 GHz. A two-section filter configuration has been chosen as the best trade-off between frequency selectivity and filter losses, as can be noticed from the graph. Subsequently, the upper line of the second section is loaded with the stub resonator and no retuning is performed at this stage. This new layout will be referred to as "loaded coupled-line filter". A schematic representation is shown in Fig. 3.11b.

The operating principles lie on the fact that, since the stub is substituting one open end of the coupled-line filter, the loaded version would work properly if and only if the channel is filled with that fluid which makes the stub resonate as an open circuit, thus the ethanol-based solution in the presented case. For this reason, the loaded filter S-parameters are simulated when the three fluids are interchanged and the results are in agreement with the expectations: when the ethanol solution fills the channel the stub offers

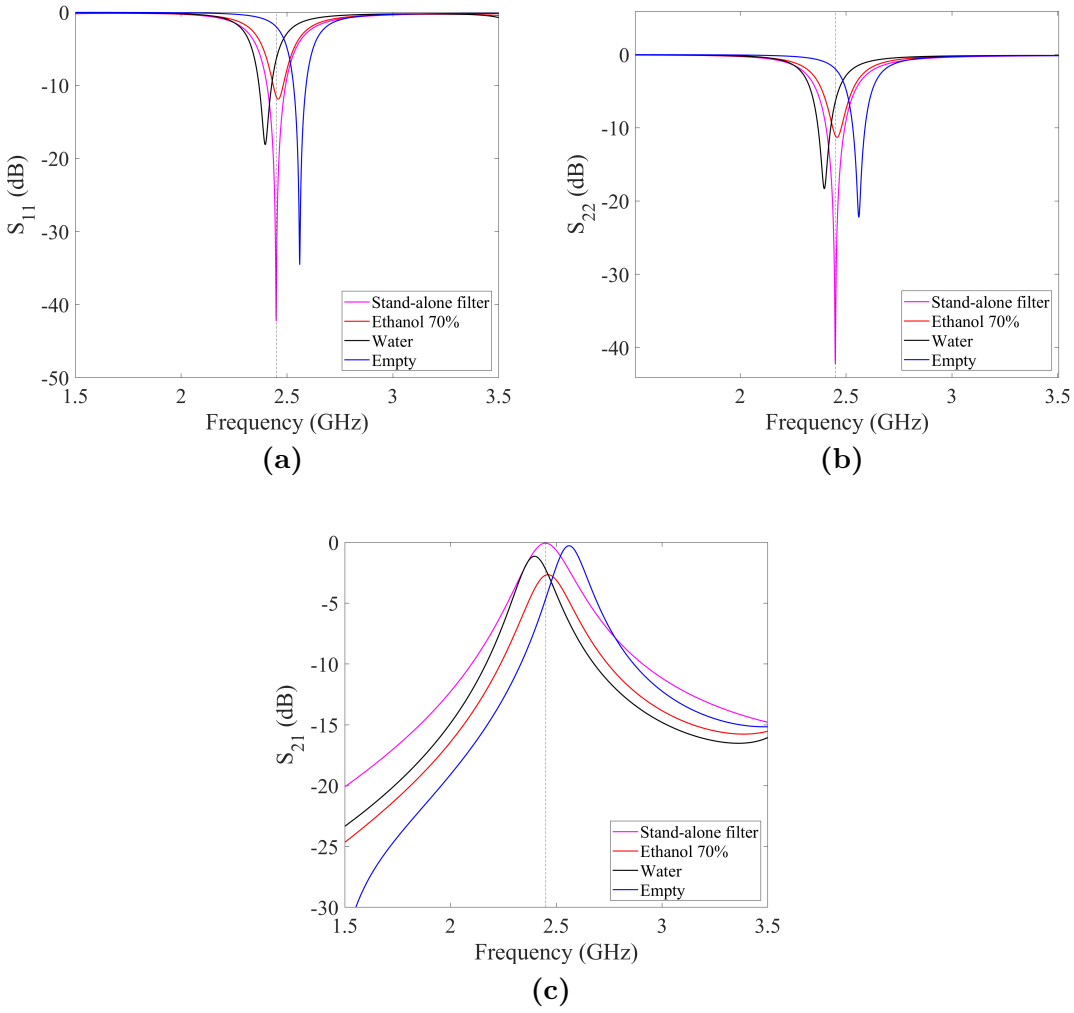

Figure 3.10: Reflection coefficient at the filter's (a) input port, (b) output port and (c) transmission coefficient for the stand-alone and for the loaded filter when fluids are interchanged. [57] © 2021 IEEE

a very high input impedance to the coupled-line filer mimicking a perfect open end termination.

The S-parameters of the loaded coupled-line filter when the three fluids are interchanged are also displayed in Fig. 3.10. As it can be seen from the graphs, the stand alone filter and the loaded coupled line filter, when the channel is filled with ethanol solution, show the same resonant frequency

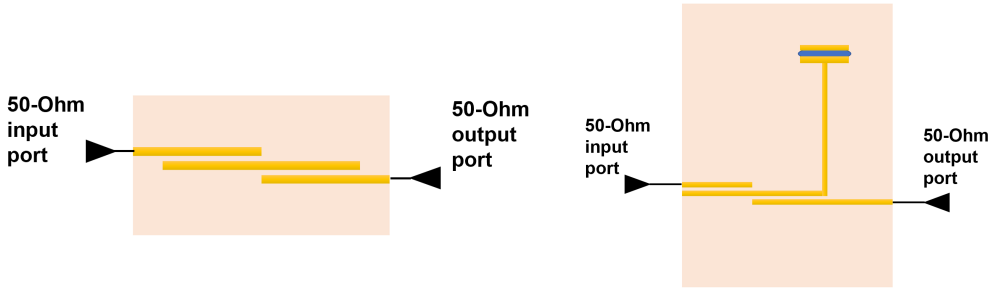

Figure 3.11: Pictorial representation of the (a) stand-alone filter and the (b) coupled-coupled line filter loaded with the stub embedding the microfluidic channel.

but with a difference in absolute values, due to the losses introduced by the non ideal open end. This behaviour confirms the achievement of a more accurate frequency and fluid selectivity allowing to proceed with further optimization of the system. The following section discuss the design of the full-wave rectifier and the circuital optimization of the overall system.

3.4 Optimization of the Designed Filtenna: the Rectifier

To properly enable a safe readout of the channel content, a rectifier is implemented to perform an RF-to-dc conversion of the incoming RF-signal. A full-wave topology has been chosen to maximize the dc-output voltage and accounts for two Schottky diodes (Skyworks SMS-7630LF) chosen for their low threshold and breakdown voltage of 0.340 V and 2 V respectively. Before carrying-out a circuital optimization exploiting the Harmonic Balance

(HB) algorithm, a study of the rectifier input impedance is performed. As well known, the rectifier is the non-linear block within a rectenna, thus the analysis of the input impedance must be done over a power range but also over a frequency range to be able to select an appropriate starting point for the advanced optimization. The chosen values for the two capacitors and resistive load are 47 pF and 6500 Ω respectively and the selected rectifier input power goes from -20 to 5 dBm. Several runs of HB simulations have been performed and the complex ratio between the input voltage and current phasors at each fundamental frequency has been used to estimate the rectifier impedance. Fig. 3.12a displays the rectifier input impedance, in terms of real and imaginary part, at the operating frequency of 2.45 GHz over a power span from -20 to 5dBm, whereas Fig. 3.12b shows the rectifier input impedance values over a frequency range, for a given input power of -10 dBm.

If the coupled-line filter is mostly designed to perform both frequency and fluid selectivity, the rectifier needs to be optimized to transfer the maximum power to the load regardless the channel content. However, for the sake of simplicity, the optimizations of the presented structure are conducted considering ht ethanol-based solution filling the channel. Moreover, being the coupled-line filter interposed between the antenna and the rectifier, it can be also exploited to achieve impedance matching, avoiding an additional matching network, which would introduce losses and increase

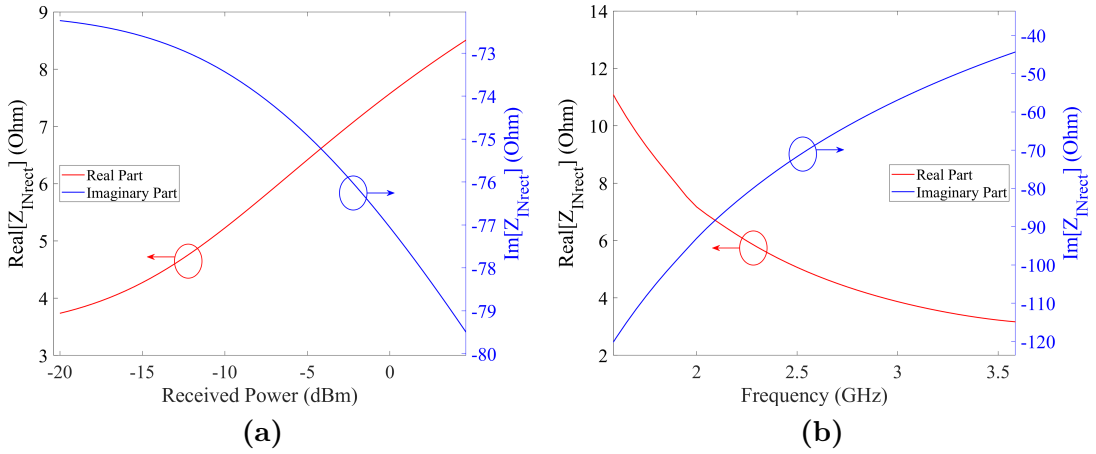

Figure 3.12: Rectifier input impedance values vs. (a) input power and (b) frequency. [57] © 2021 IEEE

the overall encumbrance. For this purpose, the circuital optimization has to be performed considering the entire structure and each component needs to be represented by its equivalent circuit model. For what concerns the patch antenna, its radiation properties are of a paramount importance to accurately estimate the received power at the filter input port [67]. The antenna radiation resistance, extrapolated from the corresponding full-wave simulation, is used as the internal resistance of the Thevenin equivalent model of an antenna in receiving mode. The circuit schematic of the overall system is reported in Fig. 3.13a, where the reference impedances are also highlighted. Z_A is the antenna equivalent impedance and can be written as:

$$Z_A = R_A + jX_A = (R_T + R_J) + jX_A \tag{3.1}$$

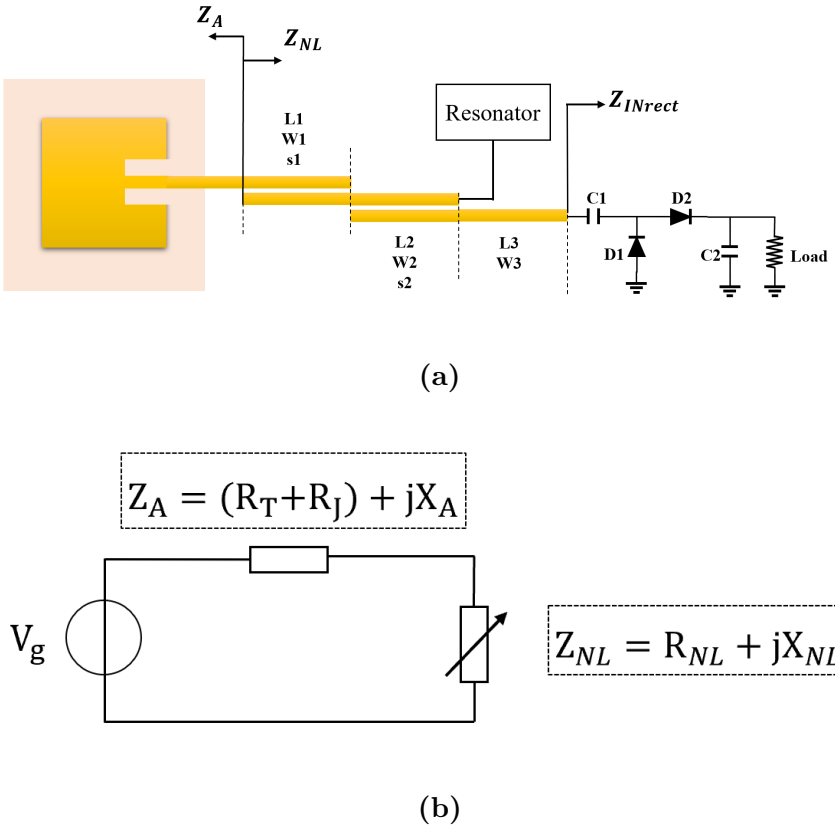

Figure 3.13: (a) Schematic representation of the proposed filtenna loaded by the rectifier and (b) its representation consisting of a Thevenin equivalent of the receiving antenna loaded by a nonlinear complex impedance. [57] © 2021 IEEE

In the definition of R_A two contributions have be distinguished: the radiation resistance R_T and the resistance associated to ohmic losses R_J.

Z_{NL} is the nonlinear equivalent impedance of the loaded-filter combined with the rectification block; in Fig. 3.13b the corresponding equivalent circuit is shown: V_g is the voltage generator that represents the RF signal impinging on the receiving antenna, whose internal impedance corresponds to Z_A. The goal is to determine the best impedance matching conditions between Z_A and Z_{NL} over a large received power range, to maximize the

power entering the rectifier. Indeed, due to the nonlinear behaviour of the rectifier, previously discussed and visually represented by the graphs in Fig. 3.12a and Fig. 3.12b, a perfect conjugate matching $Z_{NL} = Z_A^*$ between the antenna and the load can be obtained only for a fixed combination of frequency and received power. In order to correctly predict the actual received power by the antenna, it's of significant importance to distinguish the contribution and meaning of R_T and R_J. This can be obtained using the antenna radiation efficiency, extracted from the EM simulation, expressed as:

$$\delta = \frac{P_{RF}}{P_I} \tag{3.2}$$

where P_{RF} is the power delivered by the antenna to its load which, for the described case, corresponds to the available power at the coupled-line filter input, and P_I is the power impinging on the antenna. By simplifying the equation and expressing it as a function of R_T and R_J, δ can be equivalently represented as:

$$\delta = \frac{R_T}{R_A} = \frac{R_T}{R_T + R_J} \tag{3.3}$$

From (3.3), it is possible to derive the radiation resistance R_T to be used in the antenna circuit model for computing the effective received power. For the presented patch antenna, the EM analyses provides $\delta = 64\%$ and

$R_A = 50\ \Omega$, from which a radiation resistance $R_T = 32\ \Omega$, as in (3.3).

This procedure allows for a more realistic and thorough prediction of the antenna received power and thus of the actual power at the rectifier input (i.e. in a general case in which the antenna is directly connected to the rectifier). It is noteworthy to mention that this difference can be prominent and have a significant impact on the optimization process when low-efficiency antennas are considered. Indeed, if the value corresponding to R_A is considered as the internal resistance of the Thevenin equivalent model within the circuital simulation, an overestimation of the received power occurs, compared to when R_T is used. This causes a shift of the overall performance towards lower received power, as shown in Fig. 3.14 where the rectenna dc voltage is computed using R_T and R_A as the internal impedances of the voltage generator of Fig. 3.13b, respectively. The patch antenna has been firstly designed and characterized: its narrow-band characteristic allows to select the correct operating frequency to activate the coupled-line filter. The antenna is derived on the same flexible substrate, Rogers RT/duroid 5880, and it is characterized by a 5.54 dBi gain. As previously mentioned, the choice of using a patch antenna lies on the consolidated suitability of its geometry to be applied in wearable applications, indeed the ground plane avoids the antenna detuning occurring when locating the antenna close to the body surface. The EM characterization of the patch antenna is described in terms of S-parameter derived from EM

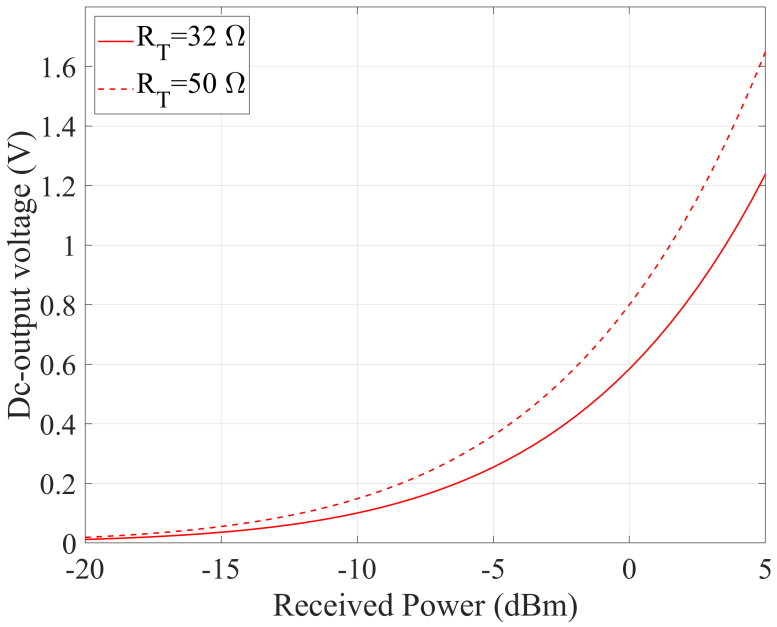

Figure 3.14: Estimated rectenna dc-output voltages for the same fluid filling the channel, when the antenna radiation efficiency is accurately accounted for (solid line) and when it is neglected (dashed line). [57] © 2021 IEEE

simulations, and the predicted received power is modelled through a RF voltage source as discussed above.

The optimization of the whole structure is conducted by means of Harmonic Balance/nonlinear simulations [68], [69] with the goals of maximizing the $\eta_{RF-to-dc}$ and dc-output voltage when the microfluidic channel is filled with the ethanol-based solution (70 % ethanol - 30 % water). The symmetrical topology of the loaded filter discussed in paragraph 2.3 is the optimization starting point and all the geometrical parameters are used as optimization variables.

Furthermore, to better exploit the filter also for matching purposes, the design has moved from symmetrical to asymmetrical coupled-lines, as in

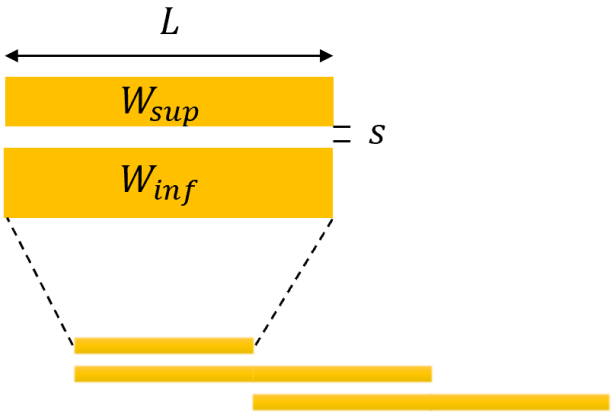

Figure 3.15: Example of an asymmetrical coupled line used in the presented design. [57] © 2021 IEEE

Fig. 3.15, which provides advantageous degrees of freedom to achieve the desired performance and avoid the use of an additional matching network [70]. The circuital optimization has been carried out using real models of the lumped element components.

Fig. 3.16 shows the simulated dc-output voltages for increasing received RF power, when the microfluidic channel is filled with the three fluids of interest: the results clearly show the system capability to identify the three fluids by providing at the rectifier output three different dc voltages, for a wide range of received power. The corresponding dc-output power on the optimum load, 6500Ω, is plotted in Fig. 3.17. In the same figure, the rectifier input power can also be derived, which is lower than the received one due to the loaded-filter insertion loss, that is about 11 dB when sensing the ethanol solutions and higher when the channel is filled with other fluids. From these figures, the rectifier sensitivity can be estimated: although a

dc output is observed with a minimum rectifier input power of -26 dBm (corresponding to a -15 dBm of received power in Fig. 3.17), the rectifier capability of showing an evident separation between the curves occurs for a minimum rectifier input power of -21 dBm (at -10 dBm of received power in Fig. 3.16). Indeed, in such conditions the dc-output voltage in the case of a channel filled with water is up to one half the value obtained when the channel is filled with the ethanol solution (corresponding to the -10 dBm of received power in Fig. 3.16). The final optimized geometrical parameters

Table 3.2: Filtenna optimized values. [57] © 2021 IEEE

COMPONENT	**STAND-ALONE FILTER**	**LOADED FILTER**
$W1_{sup}$	1.5 mm	1.5 mm
$W1_{inf}$	1.5 mm	0.47 mm
$W2_{sup}$	1.5 mm	0.5 mm
$W2_{inf}$	1.5 mm	0.7 mm
$W3$	1.5 mm	0.85 mm
$s1$	0.1 mm	0.4 mm
$s2$	0.1 mm	0.25 mm
$L1$	22.3 mm	28.9 mm
$L2$	22.3 mm	21.7 mm
$L3$	10 mm	17 mm

are compared to the ones obtained by the tuning of the reference stand-alone filter and listed in Table 3.2.

In the first section of the coupled-line filter, the upper line width is

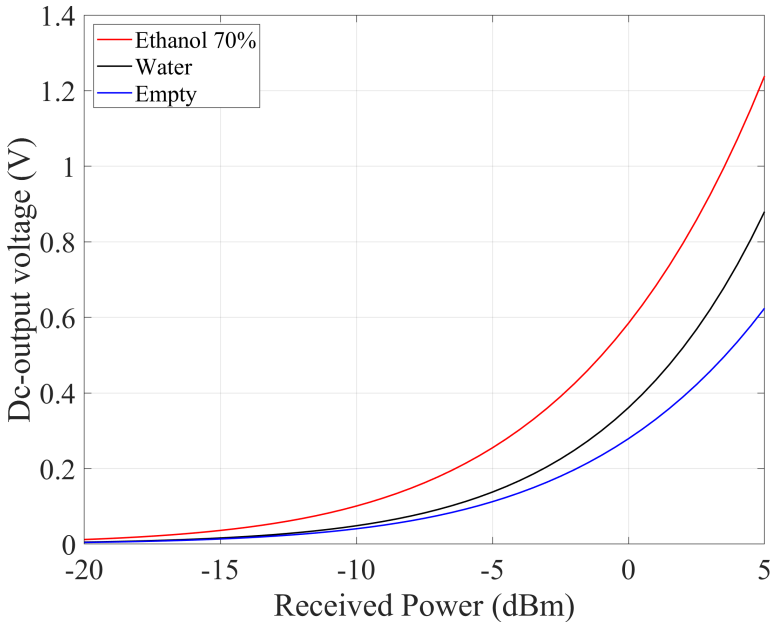

Figure 3.16: Dc-output voltage for different fluids filling the channel. [57] © 2021 IEEE

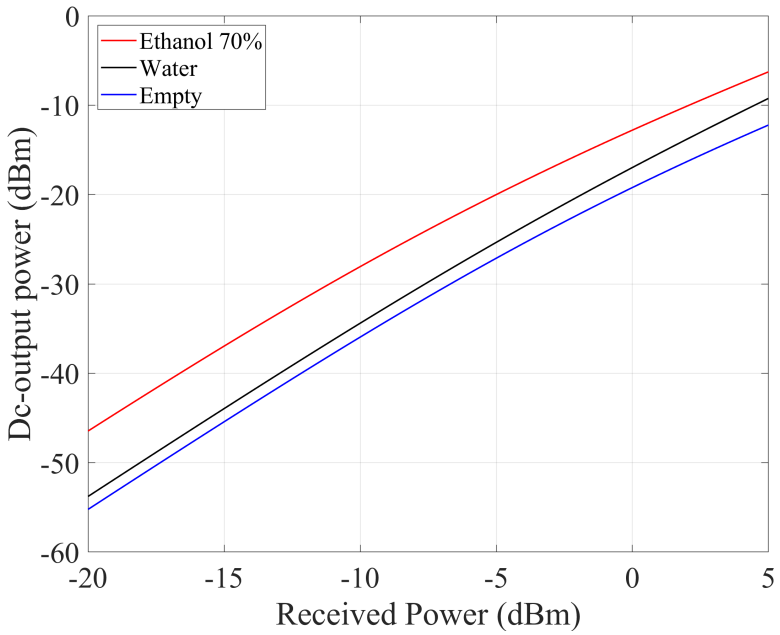

Figure 3.17: Dc-output power vs. impinging power for different fluids filling the channel. [57] © 2021 IEEE

maintained at its original length to match the one of the antenna feeding line. In the second section, using the resonant stub in place of an open

termination has resulted in a different line length with respect the the stand-alone filter. To keep the same band-pass filter performance at the resonant frequency of 2.45 GHz, the width of the remaining coupled lines results to be significantly reduced, becoming even one third of the original ones in certain cases. These geometrical parameter variations are required to have the filter performing both frequency selectivity and impedance matching between the antenna and the nonlinear rectifier. Furthermore, the coupled-line gap has been increased from 0.1 mm to 0.4 mm for the first section and from 0.1 mm 0.25 mm for the second section: this parameter plays an important role in accentuate the discernment of the three fluids, which is shown as separation of the dc-output voltage curves.

To have a thorough evaluation of the sensor performance, the system dc-output voltage and power level for variable loading conditions have been derived for a received power of 0 dBm and the trends are plotted in Fig. 3.18., for the case of having the channel filled with ethanol solution. By analysing Fig. 3.18, it is evident that the optimized value of dc-load, 6500 Ω, does not correspond to the one that would ensure the maximum dc-output power. In fact, by looking at Fig. 3.18, the maximum power is the value corresponding to the top of blue curve, which results in dc-load value of about 3750 Ω. This fact is the result of an optimization whose main goal has been the trade-off between RF-to-dc power transfer efficiency of the overall system and the ability to show appreciable and differentiated dc-output

voltages related to each tested fluid.

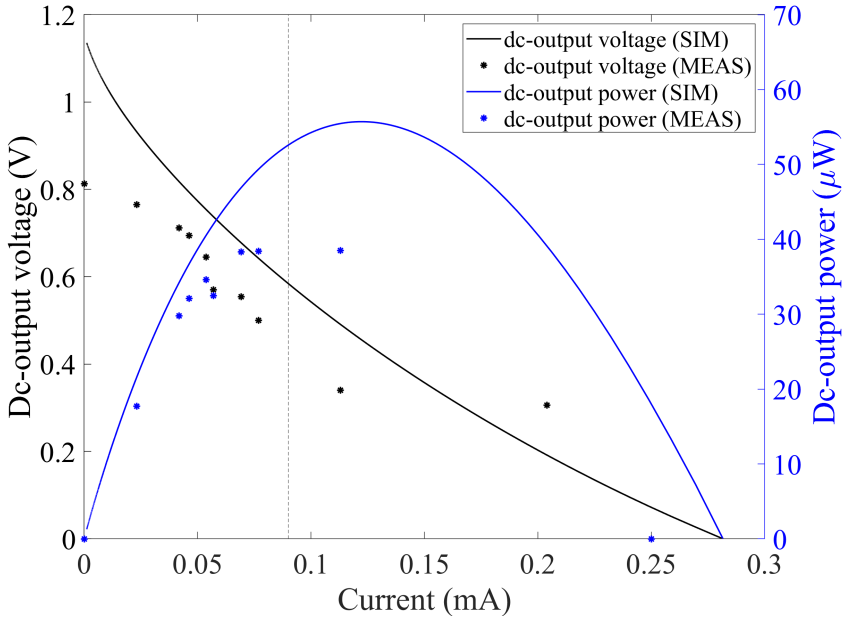

Figure 3.18: P–I and V–I rectenna characteristics in stationary conditions, for a received power of 0 dBm. [57] © 2021 IEEE

These two goals are rigorously related to the filter geometrical parameters and, more specifically, to the separation "s" between two coupled lines: a value of 0.1 mm would bring about higher dc-output voltage levels in the overall, regardless the fluid in the channel and leading to a less accurate detection of the three fluids. When the filter is optimized within a nonlinear simulation, the matching between the antenna and the rectifier is correctly performed by the filter itself. In order to have a rough representation of the filter behaviour after the optimization, the S-parameters are computed using Z_A and the rectifier input impedance at -10 dBm (see Fig. 3.12), respectively, as input and output of the 2-port system. This computation is conducted both for the loaded filter circuit model and for its EM simulation,

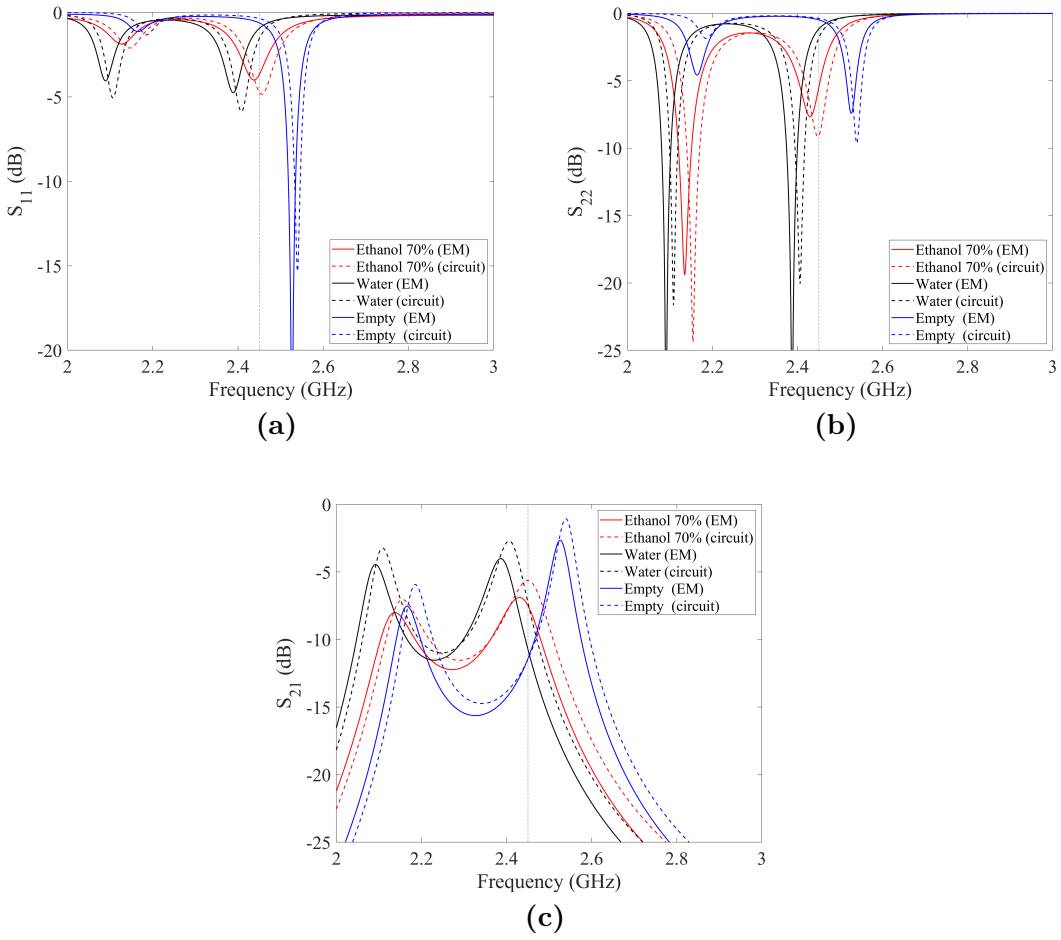

Figure 3.19: Scattering parameters of the designed filter: comparison between full-wave and circuital simulations. [57] © 2021 IEEE

and results are shown in Figs. 3.19.

As the graphs display, when the ethanol solution fills the channel, the filter resonates around 2.45 GHz and the performance expressed as reflection and transmission coefficients are evidently distinct from the other two cases, when different fluids are tested. As previously examinated, having substituted an ideal open termination of the coupled line filter with the resonant stub has induced a degradation on the performance with respect

to the stand alone filter without the resonator. However, although the absolute value accounts for the non ideality of the stub, the overall behaviour at the desired frequency is in agreement with the expectations. Fluid selectivity is performed correctly by the loaded filter at the operating frequency, showing sub-optima results.

Furthermore, to cover real case scenarios where the target ethanol solution contained in hand sanitizer may vary slightly, the system output performance have been investigated with respect to different ethanol concentrations, whose permittivity and conductivity have been derived from [71]. The results are reported in Table 3.3, for a received power of 0 dBm and show that, although concentrations may vary, the resulting dc-output voltage is always higher that the one experienced when water or air are present. Thus, it's not only possible to highlight the most common concentrations which have minimum of 60 % ethanol, but also it is possible to account for lower but rarer possible solutions who are all above the value the detector would identify as absence of ethanol.

Furthermore, for the sake of completeness, the microfluidic channel is considered half-filled with the ethanol solution whose concentration is made vary. Fig. 3.20 shows how these cases allow to safely detect the presence of ethanol despite of the half-filled channel. The simulated values are compared to the reference one, represented by the channel completely filled with the ethanol solution 70% concentration. It has to be stated that all

Table 3.3: Dc-output values for different ethanol concentrations. [57] © 2021 IEEE

ETHANOL CONCENTRATION	ε_r	σ	**DC-OUTPUT VOLTAGE**
30%	60	2.45 S/m	0.420 V
40%	52	2.45 S/m	0.463 V
50%	44	2.45 S/m	0.508 V
60%	33.5	2.18 S/m	0.585 V
70%	30	2.18 S/m	0.586 V
80%	22.8	1.91 S/m	0.608 V
90%	16	1.63 S/m	0.571 V

this presented combination between concentration and filling percentage has been investigated to simulate the detector sensitivity in the worst case scenario. However, in reality, a complete filling of the channel with a solutions having an ethanol concentration close to 70 % is highly expected.

3.5 Results and Measurements

The front view of the fabricated prototype is shown in Fig. 3.5a, whereas Fig. 3.5b displays the microfluidic channel derived in the system ground plane. The chosen technology with the ground plane allows to keep the designed wearable system, except from the microfluidic channel, completely decoupled from the human body.

The measurement campaign is conducted investigating the performance

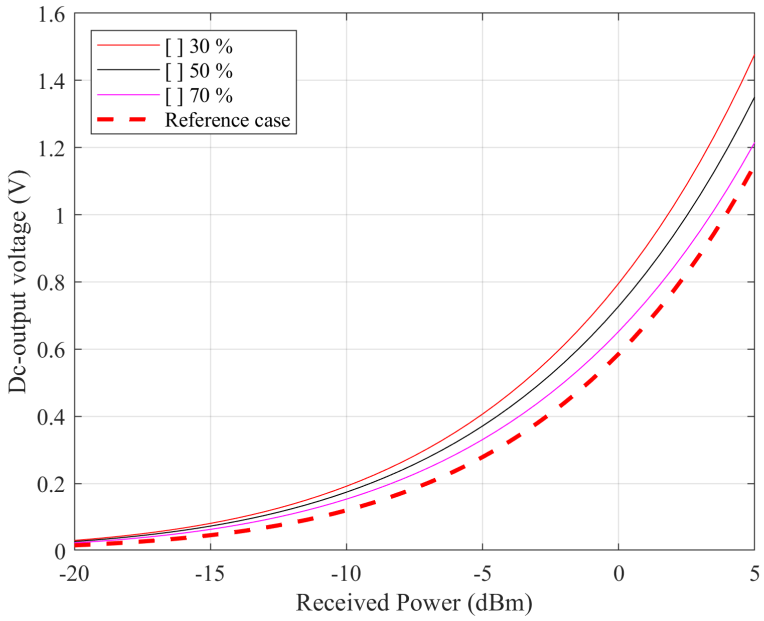

Figure 3.20: Dc-output voltage values when the channel is half-filled and the ethanol concentration is varied compared to the reference case. [57] © 2021 IEEE

of each single subcomponent separately. At first, the patch antenna reflection coefficient is characterized using a VNA (Vector Network Analyzer) to verify the correct tuning after the prototyping procedures; the results are shown in Fig. 3.21a. The corresponding radiation diagrams are then measured, first in air and then as it was placed on a human arm. As shown in Fig. 3.21b, the presence of the skin behind the antenna has influence on the front-to-back ratio, but does not affect its broadside behaviour.

Subsequently, the filter is characterized using the VNA to measure the related scattering parameters when the three fluids are interchanged.

To have a fair comparison between simulations and measurements, since the filter is connected to the VNA through two 50-Ω connectors, the full-

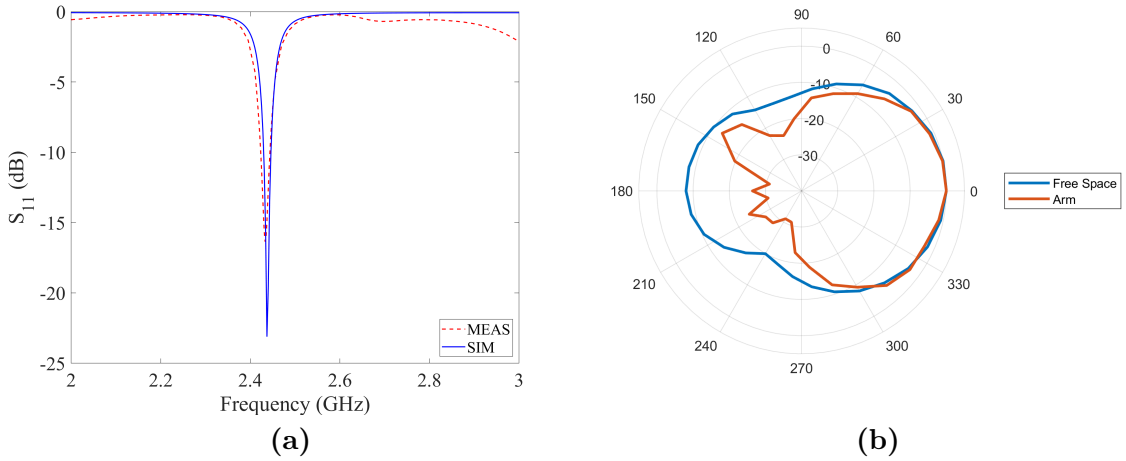

(a) **(b)**

Figure 3.21: (a) simulated and measured input reflection coefficient of the patch antenna, (b) radiation diagram for the designed patch antenna: the blue curve represents a measurement in air and the red one when the antenna is placed on an arm. The antenna gain is 5.54 dBi. [57] © 2021 IEEE

wave simulated filter scattering parameters have to be re-normalized with respect to 50-Ω terminations and results are shown in Fig. 3.22. The realized filter, measured with respect to the three tested fluids, is characterized by a slight detuning towards lower frequencies with respect to the simulated one. The new corresponding centre frequencies are 2.31 GHz for ethanol-based solution, 2.22 GHz for water and 2.46 GHz in the case of an empty channel. This discrepancy, occurred after the prototyping process, has been caused to the nonlinear/EM co-simulations that take into account a diode model whose parasitic elements, related to the diode package, may not be accurately estimated. In fact, during measurements the operating frequency of the filter is confirmed to be 2.3 GHz, with high repeatability. This is confirmed by the simulations carried out at 2.3 GHz

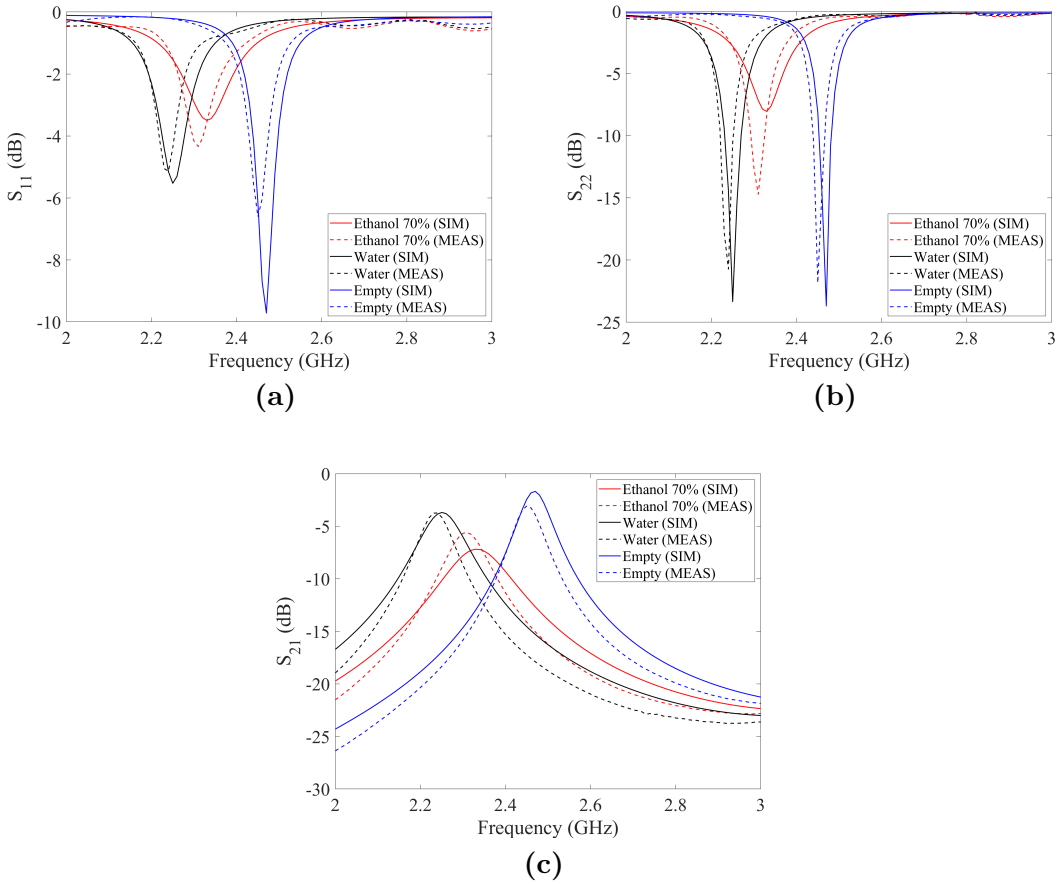

Figure 3.22: Scattering parameters of the designed filter: comparison between simulated (full-lines) and measured (dotted lines) results for the different fluid filling the channel. [57] © 2021 IEEE

that are in agreement with the measurements. To estimate the received power correctly, the filter loaded by the rectifier has been connected to the RF-generator, and the dc-output voltage is measured for increasing RF-power, first in open-circuit loading conditions and then with the optimum load of 6500 Ω. The measured values are compared with ones obtained by the circuital simulations in which the parasitic element are neglected, and results are reported in Fig. 3.23. The obtained results have also confirmed that a complete filling of the microfluidic channel can easily be achieved

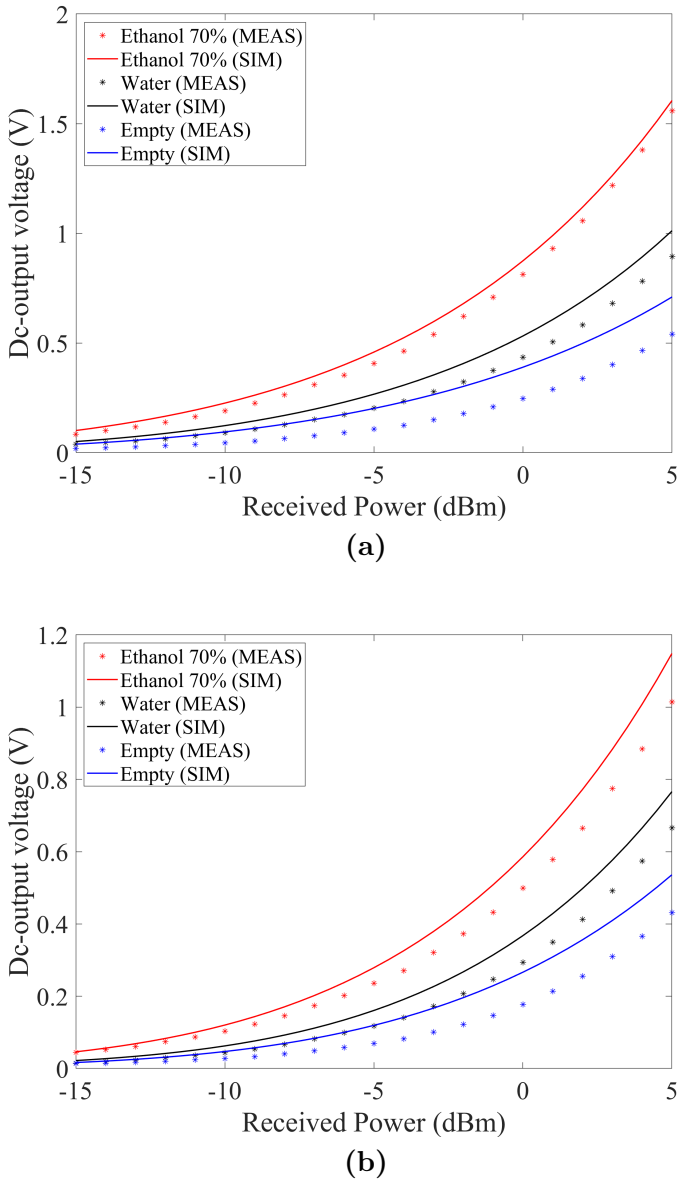

Figure 3.23: Measured dc-output voltage for (a) open circuit and (b) loaded conditions for different fluids filling the channel. [57] © 2021 IEEE

during measurements, leading to dc-output voltage values that are clearly separated. This is a confirm of the assumption made in Section 2.3 on the high probability of having the channel completely filled due to the reduced dimensions of the microfluidic channel. The outcomes are in very

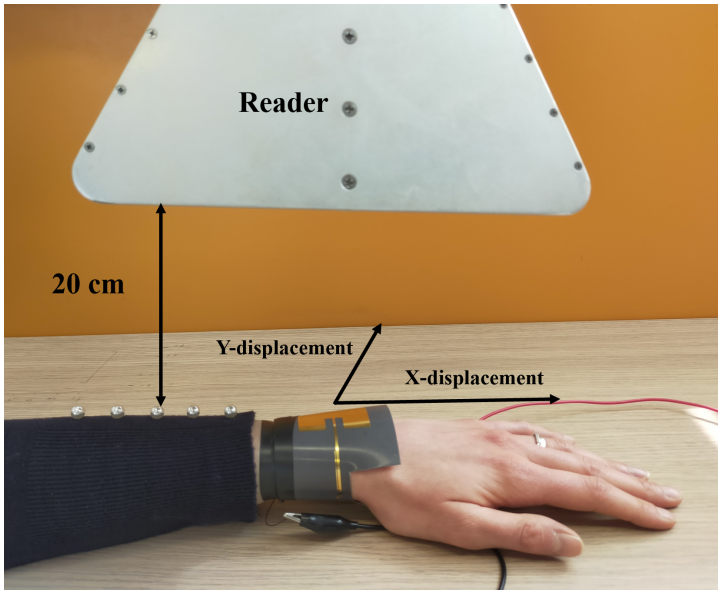

Figure 3.24: Photo of the laboratory setup used to mimic a controlled gate for ethanol detection: the distance between the RF-power source and the detector is fixed (the hand positioning on the x-y plane can vary). [57] © 2021 IEEE

good agreement throughout the entire power range, and the detection of the channel content can be performed safely. Furthermore, to overcome ambiguity, the system and the power source to energize should be placed in a line-of-sight condition and at a fixed distance. This setup allows the received power to be well determined. For a real case scenario, a controlled gate is foreseen: the subject who uses the alcohol-based hand sanitizer is asked to place the hand underneath it to perform the reading and check the correct procedure.

This is depicted in Fig. 3.24 where a horn antenna, for RF-power transmission is located at 20 cm from the bracelet; for the following measurements a received power of -10 dBm is considered. Using this set-up, the system robustness to possible displacements of the wearable detector with

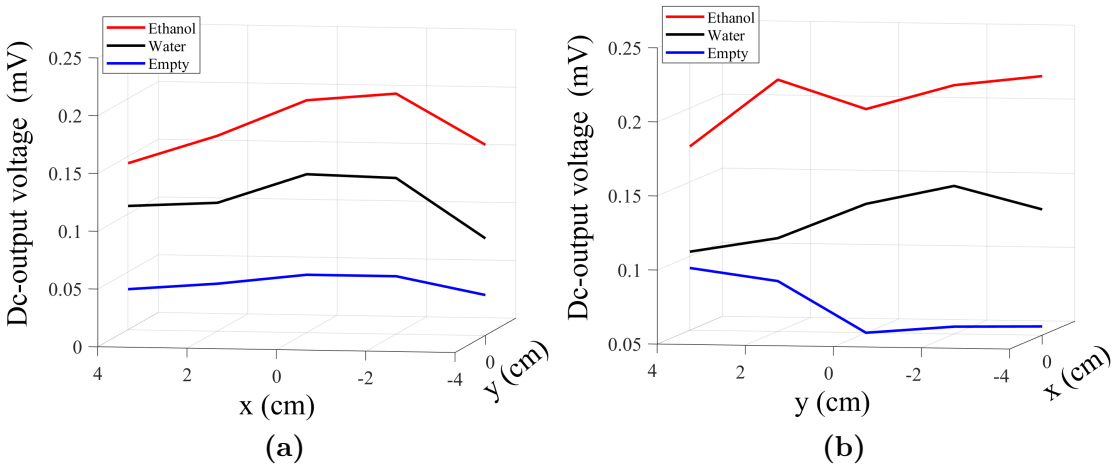

Figure 3.25: Measured dc-output voltage, on an open circuit load, for different fluids filling the channel, in case of misalignments between the RF source and the bracelet: (a) x-misalignment, (b) y-misalignment. [57] © 2021 IEEE

respect to the TX antenna has been checked: starting from a perfectly aligned position in which the two x-y centres are equal, the hand wearing the bracelet is moved along the x-y axes in a distance range of 8 cm. The measured dc-output voltages for x- and y- displacements (see Fig. 3.24 for reference) are depicted in Figs. 3.25: for both cases, it can be stated that the detection of ethanol solutions is correctly performed and accuracy is preserved regardless such large positioning uncertainties. This demonstrates the feasibility of the proposed system as an energy autonomous wearable ethanol detector.

4. Energy Harvesting System Exploiting Bessel-Beam Launchers

This Chapter is based on the following articles:

[72] F. Benassi, W. Fuscaldo, D. Masotti, A. Galli, and A. Costanzo, "Wireless power transfer in the radiative near-field through resonant bessel-beam launchers at millimeter waves," in *2021 IEEE Wireless Power Transfer Conference (WPTC)*, 2021, pp. 1–4

[73] F. Benassi, W. Fuscaldo, E. Negri, G. Paolini, E. Augello, D. Masotti, P. Burghignoli, A. Galli, and A. Costanzo, "Comparison between Hybrid- and TM-polarized Bessel-beam launchers for wireless power transfer in the radiative near-field at millimeter waves," in *Eur. Microw. Conf. (EuMC 2021)*. 2022, [Accepted Paper]

The author of this Thesis has had a relevant contribution within the above-mentioned articles, carrying out the estimation of overall link power budget and the design and optimization of a suitable rectifier to be embedded on the RX launcher.

4.1 Introduction on Bessel Beam Antenna Operating Principles

A novel solution for energy harvesting application, making use of Bessel Beam antennas at mm-waves, is presented. Although the operating principles of this type of antennas have been strongly consolidated in literature, few studies have applied them within wireless power transfer applications. With this Thesis, focus has been given to the investigation on the feasibility of this novel WPT link that boasts high focusing capability while maintaining relatively reduced dimensions.

Bessel Beams are a solution of the Helmholtz equation and one of their main important characteristics is that they have an unusual immunity from diffraction, which allows these waves to perform self-healing after being disrupted by an obstacle. Ideally, this can be achieved by using infinite aperture antennas and by providing infinite power, which makes it unfeasible for real applications . However, truncated antennas can still generate a Bessel beam, but the diffraction-free behaviour can be maintained up to a limited region when propagating away from the antenna radiating aperture, called *nondiffractive range* z_{ndr}.

$$z_{\mathrm{ndr}} = \rho_{\mathrm{ap}} \cot \theta_0 \tag{4.1}$$

where θ_0 is the so-called axicon angle that is strictly related to the leaky wavenumber and ρ_{ap} is the antenna radius. Bessel Beams are a class of leaky wave antennas, in particular, they can be described considering a *leaky radial waveguide* (LRW) excited by a coaxial cable. The model refers to a parallel plate waveguide whose upper top is substituted by a partially reflecting surface (PRS), a surface that enable the leaky behaviour offering a certain impedance and, with respect to standard 2-D LRW, the boundaries are closed on a metalling rim. This geometry allows to generate a resonant leaky mode thanks to the superposition of two leaky waves, described by means of Hankel functions [74].

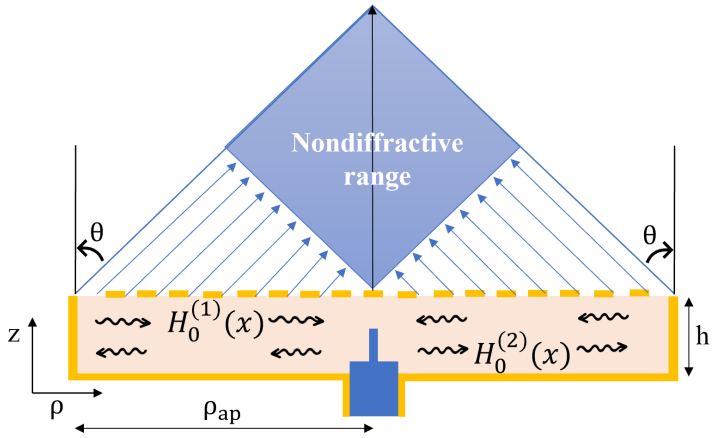

Figure 4.1: Schematic representation of a cross-sectional view of a Bessel Beam antenna fed by a coaxial cable.

The generation of a zeroth-order Bessel beam can be generalized as depicted in Fig. 4.1. The coaxial feeder allows for the excitation of the fundamental TM-leaky mode, thus the component of the electric field E_z, propagating along the broadside direction, has a profile of zeroth-order

Bessel function $J_0(k_\rho\rho)$, with k_ρ the transverse propagation constant of the beam [74]. As thoroughly described in [75], since the proposed system is invariant with respect to any planes parallel to the antenna radiating aperture, the magnetic vector potential A_z is sufficient to derive all the field components.

A_z can be described as [75]:

$$A_z = cos(k_z z)e^{jn\phi}[A_1 H_n^{(1)}(k_\rho\rho) + A_2 H_n^{(2)}(k_\rho\rho)] \tag{4.2}$$

where $H_n^{(1)}$ and $H_n^{(2)}$ are the nth-order Hankel function of first and second kind respectively.

All the field components can be easily calculated according to the theory [76]:

$$E_\rho = -j\frac{\eta}{k}\frac{\partial^2 A_z}{\partial\rho\partial z} \qquad H_\rho = \frac{1}{\rho}\frac{\partial A_z}{\partial\phi} \tag{4.3}$$

$$E_\phi = -j\frac{\eta}{k}\frac{1}{\rho}\frac{\partial^2 A_z}{\partial\phi\partial z} \qquad H_\phi = -\frac{\partial A_z}{\partial\rho} \tag{4.4}$$

$$E_\rho = j\frac{\eta}{k}(\frac{\partial^2}{\partial z^2} + k^2)A_z \qquad H_z = 0 \tag{4.5}$$

The order of the Bessel Beam function gives n=0 and the azimuthal

invariance allows to write Eq. 4.2 as [75]:

$$A_z = cos(k_z z)[A_1 H_0^{(1)}(k_\rho \rho) + A_2 H_0^{(2)}(k_\rho \rho)] \tag{4.6}$$

leading to E_ϕ=H_ρ=H_z=0 and:

$$E_\rho = -j\frac{\eta k_z k_\rho}{k} sin(k_z z)[A_1 H_1^{(1)}(k_\rho \rho) + A_2 H_1^{(2)}(k_\rho \rho)] \tag{4.7}$$

$$H_\phi = k_\rho cos(k_z z)[A_1 H_1^{(1)}(k_\rho \rho) + A_2 H_1^{(2)}(k_\rho \rho)] \tag{4.8}$$

$$E_z = -j\frac{\eta k_\rho^2}{k} cos(k_z z)[A_1 H_0^{(1)}(k_\rho \rho) + A_2 H_0^{(2)}(k_\rho \rho)] \tag{4.9}$$

As can be inferred by the equations above, each field component is made by the superposition of two cylindrical waves: inward ($H_n^{(1)}$) and outward ($H_n^{(2)}$), respectively. A constructive superposition allows for the E_z component to have a J_0 profile, and this can be achieved by placing a metallic rim at a distance ρ_{ap} for which A_1=A_2, in a practical way ρ_{ap} needs to correspond to one zero of the $J_0(k_\rho \rho_{ap})$ Bessel function. This geometrical condition allows to create a reflected wave, in this case the inward $H_n^{(1)}$, which has similar performance when compared to the outward one thanks to the finite and reduced antenna aperture. These types of antenna have particular interest when working at millimetre waves, due to the reduced wavelength and thus improved scalability. The following sections describe an application of these antennas at millimetre waves for energy harvesting purposes, focusing at first on the power budget calculation when a 37 GHz

TM-Bessel Beam launcher is exploited, and secondly discussing the design steps for implementing a TE-polarized version at 30 GHz.

4.2 Design Description and State-of-the-Art

The localized transmission of electromagnetic energy at millimeter waves (mm-waves) is a topic of tremendous interest for wireless power transfer (WPT) and energy harvesting applications [77]. The use of mm-waves WPT has led to new scenarios in which miniaturization and efficiency are well combined: as presented in [78], compact grid antennas operating at 60 GHz are used to power devices consuming up to 1 mW at 4 cm with very high beam-steering capabilities.

The state-of-the-art of wireless links is remarkably vast and varied (see, e.g., [79]). In this context, it is important to distinguish between *far-field* wireless links and *near-field* wireless links. The latter are further distinguished in *radiative* and *nonradiative* wireless links. Interestingly, the radiative near-field wireless links have several benefits over either non-radiative near-field or far-field wireless links. With respect to the former, the devices are not constrained to be in close proximity; with respect to the latter, the link budget is not constrained by Friis equation.

However, systems capable of establishing radiative wireless links in the microwave/mm-wave range are scarcely reported in the literature and most of them are based on focused, yet *diffractive* beams (see, e.g., [80]). Only re-

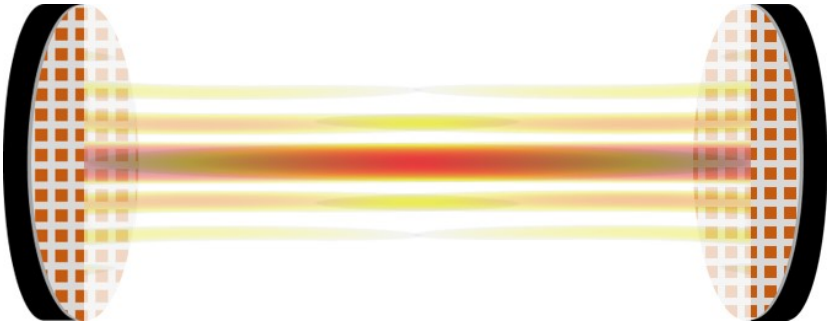

Figure 4.2: Pictorial representation of a radiative near-field wireless link between two resonant Bessel-beam launchers. [72] © 2021 IEEE

cently an energy harvesting system based on *nondiffractive* beams, namely *Bessel beams* (BB), has been preliminarily investigated [81]. The results reported therein referred to an electrically thin resonant BB launcher based on leaky modes and working at around 10 GHz. Although there exist several methods to generate Bessel beams at microwaves (see, e.g., [82]), *resonant* BB launchers as those analyzed in [83] look particularly attractive since they are capable of generating BBs by means of low-profile designs and electrically small apertures [84]. Unfortunately, these designs might lead to unbearable ohmic losses at higher frequencies such as mm-waves [74].

To this aim, we investigate here the transmission efficiency of a different kind of resonant BB launchers based on a Fabry–Perot cavity-like structure, thus featuring a $\lambda/2$-thick profile, working at about 40 GHz and experimentally validated in [74]. The transmission efficiency calculation is rigorously performed by means of a custom numerical algorithm that exploits the reciprocity and the equivalence theorem, allowing for a safe and accurate prediction of the link power budget reducing the standard computation

time needed for full-wave simulations of wireless links.

4.3 Bessel Beam Launcher Design

The common architecture of a resonant BB launcher consists of a radial parallel-plate waveguide, where the upper plate is replaced by a partially reflecting surface (PRS). The cavity is centrally fed from the bottom ground plane through the insertion of a coaxial cable that excites a *forward* cylindrical leaky mode. A circular metallic rim is then put at a proper radial distance to enforce the transverse resonance of this *forward* cylindrical leaky mode with that generated by reflection, so as to create a stationary Bessel-like aperture distribution [83]. As a result of this constructive interference, a BB is generated over a triangular region [85] whose vertex defines the so-called *nondiffractive distance* z_{ndr}; it depends on the radius of the aperture ρ_{ap} through the formula $z_{\mathrm{ndr}} = \rho_{\mathrm{ap}} \cot\theta_0$, where θ_0 is the so-called axicon angle, which is strictly related to the leaky wavenumber (details on the theoretical aspects can be found in [74, 83]).

Resonant BB launchers as those analyzed in [83] and [74] share the same architecture described above but considerably differ each other. Those in [83] are based on the excitation of the *fundamental* TM leaky mode (note that only TM modes are excited by the coaxial feed in this structure for symmetry reasons [86]) supported by the cavity that exists even for cavity heights h much smaller than the operating wavelength λ_{op}. Conversely,

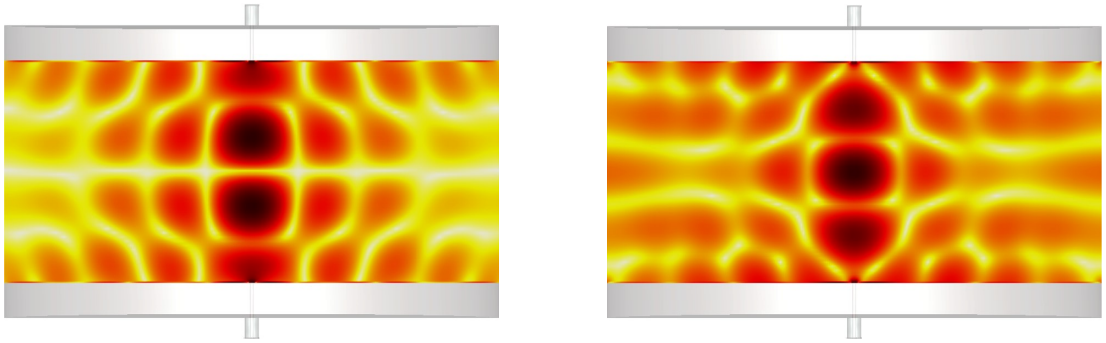

(a) (b)

Figure 4.3: Near-field distributions of E_z when both launchers are excited (a) in-phase or (b) out of phase at 37.5 GHz and are placed at a distance of 20 mm. The dynamic range goes from 0 (yellow) to 5 kV/m (black) with a logarithmic scaling. [72] © 2021 IEEE

those in [74] are based on the excitation of the first higher order TM leaky mode, thus it resonates for cavity heights h approximately equal to $\lambda_{\mathrm{op}}/2$. The resonance is affected by the reflectivity of the PRS, which is here fully described by its surface impedance Z_{s}.

Here, we analyze a WPT link using two identical BB launchers of the latter type (see Fig. 4.2). Specifically, we used the same design of [74], but working at 37.5 GHz instead of 39.7 GHz. The main physical parameters (namely, ρ_{ap}, h, Z_{s}) and radiating features (namely, the radial spot size S_ρ, the radial confinement ratio defined as $C_\rho = S_\rho/2\rho_{\mathrm{ap}}$, and z_{ndr}) are reported in Table I for the reader's convenience.

The coupling between the two launchers at different distances from one another has been simulated with the time-domain solver of CST Microwave Studio at 37.5 GHz, where a BB resonating so as to have the fourth null at ρ_{ap} is expected from an accurate dispersion analysis of the considered

Table 4.1: Design parameters and radiating features of the BB launcher. [72] © 2021 IEEE

Design Parameter	**Value**	**Radiating Feature**	**Value**
ρ_{ap}	22.3mm	S_ρ	9 mm
h	3.175 mm	C_ρ	20%
Z_{s}	$-j25\,\Omega$	z_{ndr}	24 mm

structure (see [74]).

The creation of a limited-diffractive wireless channel through the radiative near-field coupling of the two BB launchers placed at a reference distance of 20 mm (note that $z_{\mathrm{ndr}} \simeq 25\,\mathrm{mm}$) is manifest from Fig. 4.3(a)–(b), where the near-field distributions of the vertical electric field component E_z when the two launchers are simultaneously excited in-phase (Fig. 4.3(a)) or out-of-phase (Fig. 4.3(b)) is shown. We note that the in-phase/out-of-phase excitations correspond to the odd/even mode identification reported in [81] through a mode-matching analysis of similar devices working at 10 GHz.

4.4 Link Budget Prediction at 37.5 GHz

In order to quantify the received power, a link budget model is exploited. This numerical method has the advantage of calculating the power budget of a transmitter-receiver (TX-RX) link with half the computational time; in fact the full-wave simulation of only one of the two identical radiators is required to derive the performance of the whole link, with results compara-

ble to a full-wave simulation of the link including both the transmitting and receiving antenna. A first electromagnetic characterization is performed using a single BB launcher, which can be represented as the "RF source" in Fig. 4.4, and the electromagnetic (EM) field distribution, up to a distance of 20 mm from the tx launcher, is exported. Subsequently, a numerical algorithm is used to reconstruct the EM fields radiated by the launcher placed on the RX side. As described in [87], both the extracted EM fields are evaluated on a surface S which is located between the two launchers, as shown in Fig. 4.4. In the presented scenario, the evaluation plane is placed in the middle of the separation distance between the two launchers.

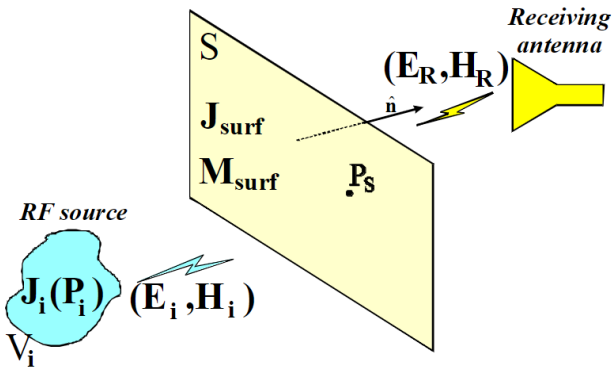

Figure 4.4: EM-theory-based model for the accurate and fast evaluation of the link budget. [72] © 2021 IEEE

This methodology [87] derives from the combination of the equivalence theorem and the reciprocity theorem and allows to represent the receiving antenna by a Norton equivalent circuit, whose current source is J_{eq}. The antenna admittance $Y_{\mathrm{a}}(\omega)$ can be evaluated through full-wave simulations

reducing the calculation of the received power to the evaluation of J_{eq} in the presence of a monochromatic incident field coming from a transmitting antenna of volume V_i. By applying the reciprocity theorem, the receiving antenna is made operate in the transmitting mode, when driven by a sinusoidal voltage source of emf U and internal impedance Z_R, and then in the receiving mode, loaded by Z_R, and immersed in the incident field generated by the transmitting antenna. To model a 2-antennas link, and extend this computation to a general case including both far- and near-field conditions, the independent transmitting antenna of volume V_i is substituted with the electric and magnetic surface currents, J_{surf} and M_{surf} in Fig.4.4, evaluated on a plane S placed between the two antennas. The J_{eq} is then rigorously calculated as:

$$J_{\mathrm{eq}} = \frac{1 + Z_{\mathrm{R}} Y_{\mathrm{a}}(\omega)}{U} \cdot \hat{\mathbf{n}} \bullet \int_S [\mathbf{E}_{\mathrm{i}}(P_{\mathrm{S}}) \times \mathbf{H}_{\mathrm{R}}(P_{\mathrm{S}}) - \mathbf{E}_{\mathrm{R}}(P_{\mathrm{S}}) \times \mathbf{H}_{\mathrm{i}}(P_{\mathrm{S}})] \mathrm{d}S \quad (4.10)$$

where E_{i}, H_{i}, E_{R} and H_{R} are the electric and magnetic fields of the transmitting and receiving antennas (i.e., launchers, in our case) respectively.

The received power P_{r} can be calculated as [88]:

$$P_{\mathrm{r}} = \frac{|J_{\mathrm{eq}}|^2}{8\mathrm{Re}(Y_{\mathrm{a}}(\omega))} \quad (4.11)$$

For the presented case, the received power is computed for different distances between the two launchers, which are perfectly aligned to each other, using a 13 dBm transmitted power. Subsequently, the same calculations are performed having a 5 mm misalignment along the x-direction for the transmitting antenna. Results are shown in Table 4.2.

Table 4.2: Received power at 37.5 GHz. [72] © 2021 IEEE

TX-RX distance (mm)	P_{r} **(dBm)**	P_{r} **(dBm) with 5 mm misalignment**
10	6.3	-4
20	5.1	-7.7
30	0.9	-9.7
40	-5.5	-14.1

As can be inferred from Table 4.2, the transmitted power is focused with high precision along a specific direction, confirming the limited-diffraction characteristics of the wireless channel created with the resonant BB launchers.

4.5 Bessel-beam Rectenna Design

After evaluating the expected received power for the presented reference distances, a rectifier connected to the rx antenna is designed by means of harmonic balance simulations. The circuit is derived on a Rogers RO3003 ($\varepsilon_r = 3.02$, $\tan\delta = 0.001$ at 10 GHz) with a thickness of 0.256 mm. This substrate is suitable for mm-wave applications because it boasts dielectric

properties that are almost constant in the 10-50 GHz frequency range. The circuit makes use of a GaAs Schottky diode (Teledyne TSC-S-01020), chosen for its low junction capacitance (1 fF), allowing a cut-off frequency above 2 THz. These characteristics, together with a very low parasitic capacitance, and an ultra-low series resistance make this diode suitable for building rectifiers operating in the mm-wave frequency range. The proposed topology is a half-wave rectifier, represented in Fig. 4.5. Due to the mm-wave operating frequency, this rectifier topology has been chosen as the best trade-off between component losses, due to the parasitic elements of the diode package, and rectification efficiency.

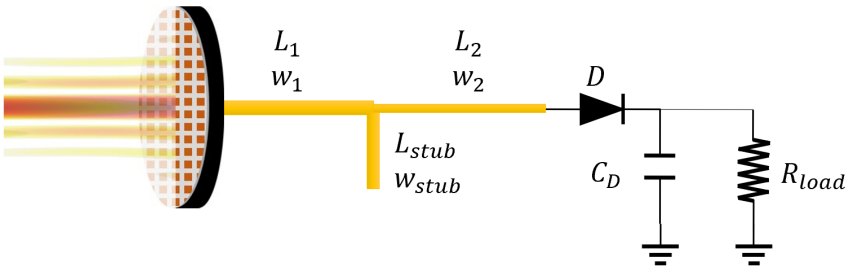

Figure 4.5: Circuit schematic of the 37.5 GHz rectenna adopting the Bessel-beam launcher. [72] © 2021 IEEE

The rectifier and its matching network are optimized with the goal of maximizing the $\eta_{\mathrm{RF-to-dc}}$ efficiency over a power range going from -8 dBm to $+6$ dBm and the resulting optimum values are listed in Table 4.3.

This power range has been chosen in order to be in agreement with the received power calculated through the link budget, focusing more attention on farther distances, namely 20, 30 and 40 mm. As a matter of fact, the

Table 4.3: Rectifier optimized values. [72] © 2021 IEEE

Component	Value	Component	Value
L_1	6.3 mm	L_{stub}	3.82 mm
w_1	0.65 mm	w_{stub}	0.47 mm
L_2	5.86 mm	C_D	50 pF
w_2	0.3 mm	R_{Load}	2700 Ω

closest distance of 10 mm would experience a received power that overcomes the diode breakdown voltage, however the considered distances lead to a more realistic scenario. Figure 4.6 shows the optimized $\eta_{\text{RF-to-dc}}$

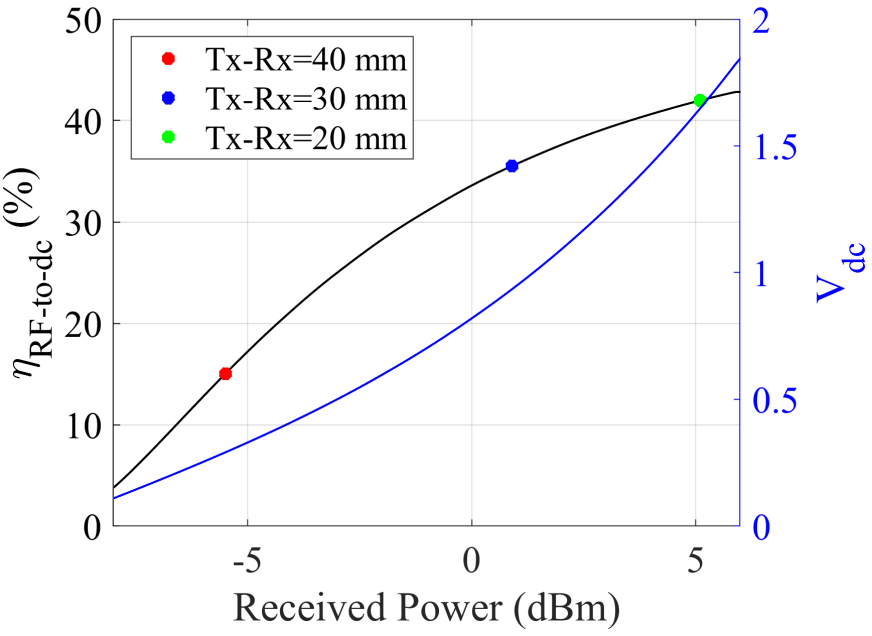

Figure 4.6: RF-to-dc power conversion efficiency and dc-output voltage vs received power (rectenna distance decreases) for a RF-power at the TX launcher input of 13 dBm. [72] © 2021 IEEE

and dc-output voltage for different received power levels. Moreover, in the same graph, the efficiency is highlighted in correspondence to the chosen TX-RX reference distances in the case of having no misalignment.

4.6 TE-polarized Bessel Beam Launcher: Design Goals

The previous sections have described the design and optimization of a wireless power transfer link made by two TM-polarized Bessel Beam launchers. The coaxial cable feeding allows for having a perfect 50-Ω antenna input impedance, but it does not allow to create a compact structure by embedding the entire receiving circuitry inside the cavity.

In the upcoming sections, we aim at further analyzing the potentialities offered by FPC-like BB launchers, by considering also configurations that are, in principle, capable of generating a TE-polarized BB through a loop antenna feeder (see, e.g., [89]). Here, we show that a realistic loop feeder radiates a hybrid-polarized BB instead of a purely TE BB, as manifested from full-wave results of the near-field electromagnetic distribution. A comparative analysis is then carried out between hybrid-polarized and TM-polarized BBs.

4.7 Design Workflow

4.7.1 Theoretical Framework

As described in 4.1 Bessel Beams are created by enforcing a radial resonance between the *outward* cylindrical leaky wave launched by the central

feeder, and the *inward* one coming from reflection on the circular metallic rim. The constructive interference between these two waves is obtained by placing the circular metallic rim in one of the zeros j_{0n}, $n \in \mathbb{N}$ of the desired stationary Bessel-like aperture distribution, thus leading to the following equation:

$$\beta \rho_{\mathrm{ap}} = j_{0n}, \tag{4.12}$$

where β represents the phase constant of the generally complex, leaky, radial wavenumber $k_\rho = \beta - j\alpha$, with α being the attenuation constant [74]. Here, we present a design workflow to *i)* determine β and α to create a BB with a given constraint on z_{ndr} and ρ_{ap}; *ii)* determine the cavity height and PRS surface impedance to get the required β and α at a given frequency f_0.

According to the theory, β is related to the axicon angle through $\beta = k_0 \sin\theta_0$ (k_0 being the free-space wavenumber), thus from (4.1) and (4.12) one finds a useful relation between the nondiffractive range, the aperture radius, and the order of the radial resonance n of the structure, which reads:

$$\bar{z}_{\mathrm{ndr}} = \bar{\rho}_{\mathrm{ap}} \sqrt{(\bar{\rho}_{\mathrm{ap}}/\bar{\rho}_n)^2 - 1}, \tag{4.13}$$

where the bar $(\bar{\cdot})$ indicates normalization with respect to the vacuum wavelength λ_0, and we have conveniently defined $\bar{\rho}_n = j_{0n}/2\pi$.

As the TM-polarized Bessel Beam [72], this further implementation con-

siders a realistic energy harvesting scenario for rechargeable wearable devices. For this purpose, the required covered distance has to be greater than 2 cm, and the device radius has to be lower than 1.5 cm. With respect to the TM-version [72], this new design aims to lower a little the operative frequency while maintaining a relatively small dimensions of the structure. With a design that operates at $f_0 = 30$ GHz, we have the possibility to satisfy the constraints of the EH scenario with both the first, $n = 1$, and the second, $n = 2$, radial resonance. However, a BB launcher working with the first radial resonance would produce a highly truncated BB, thus we preferred to consider $n = 2$ for which (4.12) yields $\hat{\beta} = \beta/k_0 \simeq 0.5857$ at which corresponds $\theta_0 \simeq 36°$.

At this point, $\hat{\alpha} = \alpha/k_0$ has to be determined. As shown in [74], a BB is obtained as long as the inward/outward cylindrical leaky waves have almost the same amplitude. At a first approximation, we may assume plane-wave propagation (which ignores the radial spreading of cylindrical leaky waves) inside the cavity, such that the previous criterion translates into $\hat{\alpha} < -\ln a_\mathrm{r}/(4\pi\bar{\rho}_\mathrm{ap})$, where $0 < a_\mathrm{r} < 1$ is the ratio between the power amplitudes of the inward and outward wave. This ratio should be moderately close to 1, in order to obtain a good BB profile, without requiring the design of a very high-Q cavity, and in turn an extremely narrow fractional bandwidth. Here, we set $a_\mathrm{r} = 0.95$ to get $\hat{\alpha} \simeq 0.0027$.

From the knowledge of the required $\hat{\beta}$ and $\hat{\alpha}$, one can easily get de-

sign equations for the cavity height h and the PRS sheet reactance X_{s} (which fully characterizes a *lossless* PRS), using an equivalent loss tangent model for the cavity [90]. For the choice made here, viz., $\hat{\beta} \simeq 0.5857$ and $\hat{\alpha} \simeq 0.0027$, and assuming an air-filled cavity we get $X_{\mathrm{s}} = 26.7\,\Omega$ and $h = 6.04\,\mathrm{mm}$ at 30 GHz.

4.7.2 Feeder Implementation

In principle, a VED (Vertical Electric Dipole) or a VMD (Vertical Magnetic Dipole) excitation is realized by centrally feeding the cavity with a coaxial probe [74] or a loop antenna [89], respectively. In practice, while coaxial probes are good representations of VEDs, small loop antennas are not as much as good representations of VMDs. As a result, the former excitation scheme allows for having a purely TM-polarized BB, whereas the latter leads to a *hybrid-TE-polarized* BB instead of a *purely* TE-*polarized* BB. This aspect is actually confirmed by full-wave simulations. Specifically, full-wave results for a coaxial feeder show no H_z component and a zeroth order Bessel function over the E_z component, as expected for the TM case. Conversely, full-wave results for a loop antenna feeder show a zeroth order Bessel function over the H_z component, but also a non-zero E_z component; this clearly demonstrates that a purely TE-polarized BB cannot be generated with such a loop antenna feeder. Nevertheless, it is interesting to compare the energy harvesting performance in this case, which will be

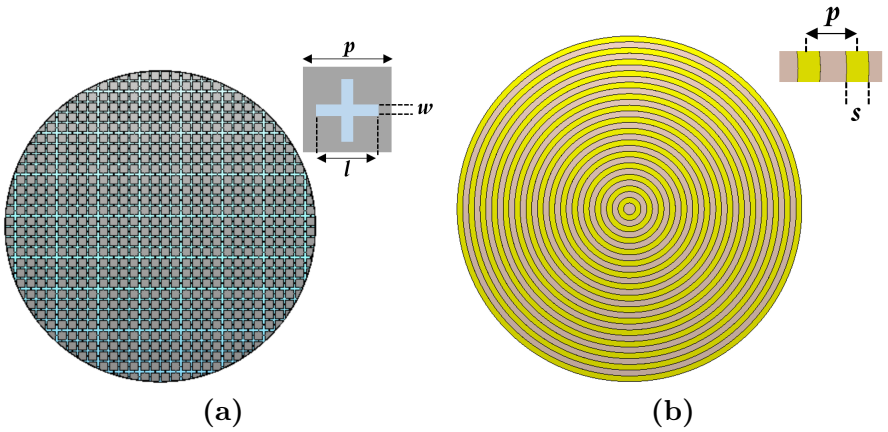

Figure 4.7: Pictorial representation of the two metasurfaces: (a) the fishnet-like for the TM-polarized BB launcher, (b) the annular strip grating for the hybrid-TE polarized BB launcher. [73] © 2022 EuMA

referred to as a *hybrid-TE polarization*, with respect to that of a purely TM-polarized BB launcher.

4.7.3 Metasurface Implementation

So far, we have made a theoretical analysis assuming a surface impedance approximation that is proven to be an accurate one for well-known geometries such as square patches and strips in the homogenization limit [91]. However, such canonical geometries sometimes do not offer enough degrees of freedom to obtain an arbitrary value of surface impedance, without requiring extreme variations of the design parameters [92]. For this purpose, in the TM case we have synthesized a fishnet-like unit-cell as those analyzed in [92]. Full-wave simulations of a unit-cell (not shown for brevity) demonstrate that the geometry shown in Fig. 4.7(a) with $p = 1$ mm, $w = 0.2$ mm,

and $l = 0.95$ mm realizes a surface reactance of about $X_{\mathrm{s}} \simeq 27\,\Omega$ at around 30 GHz. The radiated fields for the TM-polarized BB launcher fed with a coaxial cable and with the described metasurface are reported in Fig. 4.8(a). As shown, the field is purely TM and the field peak for the E_z component is rather high.

Unfortunately, this metasurface does not allow us to achieve satisfactory results in the TE case. Conversely, we have found that an annular strip grating in the homogenization limit is capable to produce better results under TE polarization. Specifically, we have considered an annular strip grating with $p = 1$ mm and $s = 0.5$ mm, printed on a Rogers 3003 substrate (relative dielectric permittivity of 3 and loss tangent of about 0.001) having a thickness of 0.256 mm. Unfortunately, analytical formulas for annular strip gratings only apply for $s \ll p$, a condition that is not fully met here (viz., $s/p = 1/2$), thus preventing the application of the previous analysis.

As can be inferred from Fig. 4.8(b) the field is mainly TE, the E_z component being an order of magnitude smaller than E_{t}, and the H_z following a zeroth order Bessel function profile.

The structure has been simulated considering the same loop feeder used with the impedance approximation and the simulated fields are depicted in Fig. 4.8b. Subsequently, the power budget will be computed comparing the performance between the TM-polarized BB launcher with the fishnet-like metasurface and the hybrid-TE Bessel Beam launcher with annular strip

grating.

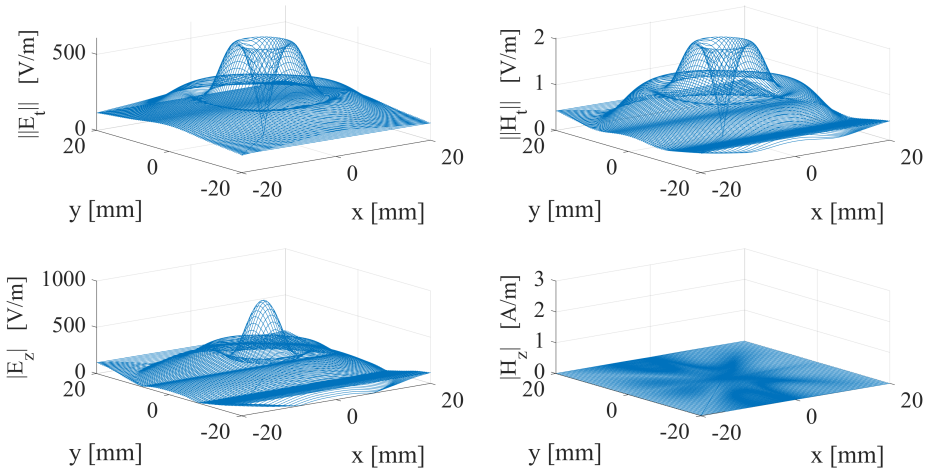

(a)

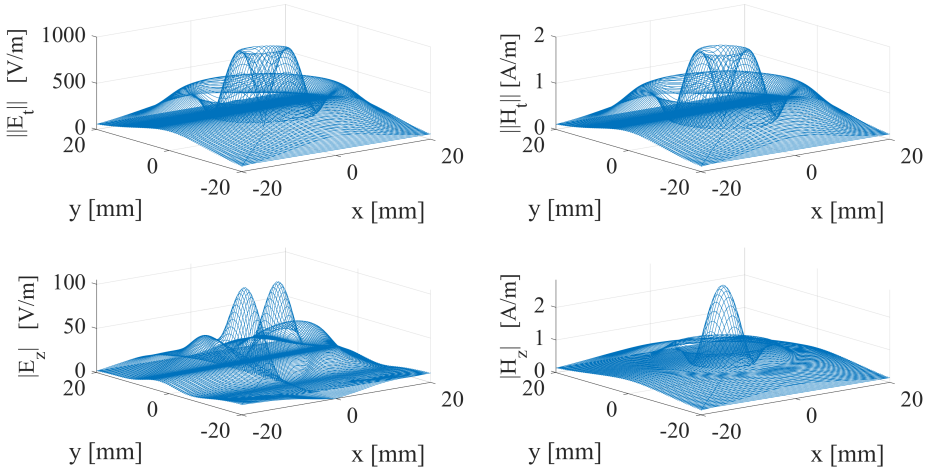

(b)

Figure 4.8: Full-wave results for the (a) TM-polarized BB launcher, and the (b) hybrid-TE polarized BB launcher with annular strip grating structure. [73] © 2022 EuMA

4.8 Link Budget Prediction at 30 GHz and Rectenna Design

To quantify the received power and carry out a safe comparison between the two types of launchers, the general-purpose link budget model described in paragraph 4.4 is adopted. For the presented case, the received power is calculated for different separation distances between the launchers, which are placed in perfect alignment to each other (effects of misalignments have been preliminarly discussed in [72]): for the following calculations, a reference input power at the TX side of 21 dBm is considered. For the same TX-RX distances the received power P_r has been computed in the case of the two couples BB launchers, accounting for the respective complex internal impedances, and the results are reported in Table 4.4.

Table 4.4: Received power at 30 GHz for differently fed BB launchers. [73] © 2022 EuMA

TX-RX distance (mm)	P_r **(dBm)** **TM BB with PRS**	P_r **(dBm)** **Hybrid-TE BB with annular strip grating**
20	10.7	6.4
30	5.7	-0.6
40	-0.7	-5.4

Table 4.4 reports the predicted received power at the BB launcher receiver side for the selected excitation conditions. The research activity is

in progress in order to optimize the launchers excitation network further, which can affect the exploited modal distribution.

After evaluating the expected received power for the above-mentioned reference distances, a rectifier to be connected to the RX launcher is designed by means of harmonic balance simulations, as previously done for the TM-polarized one. The received power level in which the optimization has been carried out are related to the annular strip grating structure. The circuit is implemented on a Rogers RO3003 ($\varepsilon_r = 3$, $\tan\delta = 0.001$ at 10 GHz) with a thickness of 0.256 mm and makes use of a GaAs Schottky diode (Macom MA4E2038), chosen for its low series resistance and high cutoff frequency that make it suitable for building rectifiers operating in the mm-wave range. The proposed topology is a half-wave rectifier, represented in Fig. 4.9(b).

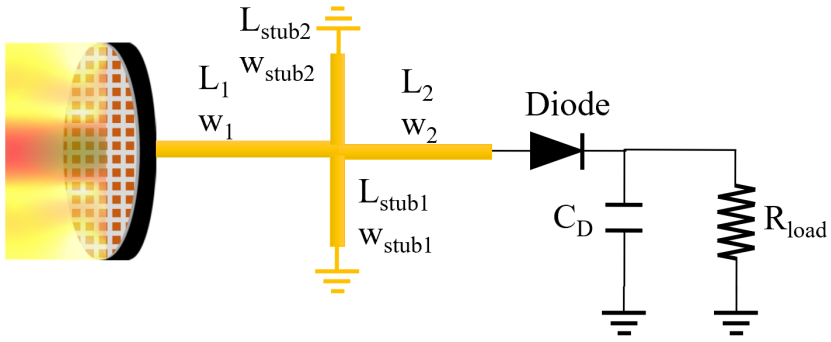

Figure 4.9: Circuit schematic of the 30 GHz rectenna adopting the annular strip grating BB launcher, for an RF-power at the TX launcher input of 21 dBm. [73] © 2022 EuMA

The hybrid-polarized launcher is fed by a loop antenna ($2\pi R \simeq \lambda$), which presents an inductive input impedance $Z_{\mathrm{A}} = 26.05 + j8.47\,\Omega$, whereas the

TM-polarized launcher is fed by a standard coaxial probe, which shows a real input impedance of about $Z_{\mathrm{A}} = 50\ \Omega$. Obviously, two distinct rectifiers designs are required in particular, due to the different antenna input impedance, a different matching network is realized to obtain comparable performance for the $\eta_{\mathrm{RF-to-DC}}$.

Table 4.5: Rectifier optimized values for the BB launcher under analysis. [73] © 2022 EuMA

Component	**Value**	**Component**	**Value**
L_1	4 mm	L_{stub1}	4.7 mm
w_1	0.76 mm	w_{stub1}	0.5 mm
L_2	2.7 mm	L_{stub2}	4.6 mm
w_2	0.76 mm	w_{stub2}	0.72 mm
R_{Load}	3600 Ω	C_D	100 pF

The optimization process is carried out only for the annular strip grating design and the goal is again the maximization of the $\eta_{\mathrm{RF-to-DC}}$ efficiency over a power range going from -7 dBm to $+8$ dBm, accounting for the real models of the linear components. The resulting optimum values are listed in Table 4.5.

This power range is chosen in order to be in agreement with the RX power calculated through the link budget, achieving good results especially at farther distances, namely 30 and 40 mm with a corresponding $\eta_{\mathrm{RF-to-DC}}$ of 30 % and 13 % respectively as shown in Fig. 4.10.

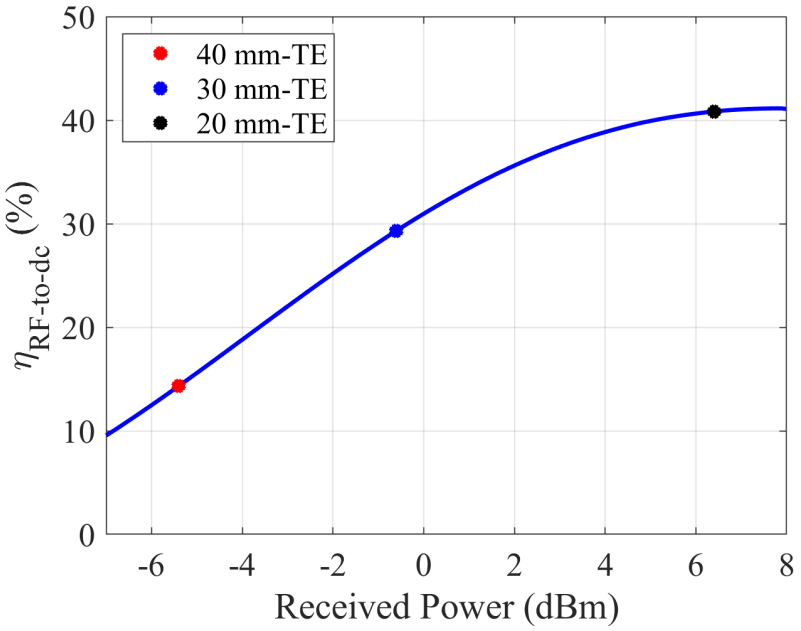

Figure 4.10: RF-to-dc power conversion efficiency for the Hybrid-TE Bessel Beam launcher.

5. Batteryless System Enabling LoRa Tracking in Industrial Plants

This Chapter is based on the following article:

[93] B. Gok, F. Benassi, D. Masotti, and A. Costanzo, "A wireless/wired uhf modular system combining energy and data transfer," in *2022 IEEE Wireless Power Transfer Conference (WPTC).* 2022, [Accepted Paper]

The author of this Thesis has been fully involved in the design and realization of the system proposed in [93] as co-supervisor of the first author, leading and coordinating both full-wave simulations, circuital optimizations and measurement campaign of the entire system.

5.1 Introduction

The aim of enabling the industry toward smarter systems and advanced services emerges concepts such as Industrial Internet of Things (IIoT) where instruments and sensors are connected to industrial applications through the internet. Among many applications of IIoT, one valuable benefit is the asset tracking which allows manufacturers to track the location, status and condition of products during the supply chain, not only for indoor tracking but also for long ranges [94]. The technology of low-power wide-area network (LPWAN) leads to a promising utilization in wireless communication because of its effective coverage, inexpensive deployment and low power consumption [95]. The study [96] shows that localization can be obtained using LoRa (short for long range), which is an RF modulation technology of LPWAN, in harbour environment with proper variables such as spreading factor. Solutions of adjusting the cycle of wake-up and sleep was thought in order to decrease the power consumption of wireless sensor networks (WSNs). In order to eliminate the disadvantage of batteries, one must turn its focus on technologies such as wireless power transfer (WPT). For example, a study [97] shows that efficient wireless powering of small-sized industrial sensors is possible even at millimetre waves through directive antennas.

In this Chapter, the design, realization and characterization of a mod-

ular system for the simultaneous transmission of energy and information between unplugged trolleys in industrial plants is presented. This can be achieved by means of a suitable combination of wireless power transfer between two consecutive trolleys, and guided power transfer between the edges of the same trolley. With respect to similar applications in literature, this design boasts modularity, allowing it to work properly regardless the order with which each trailer is connected.

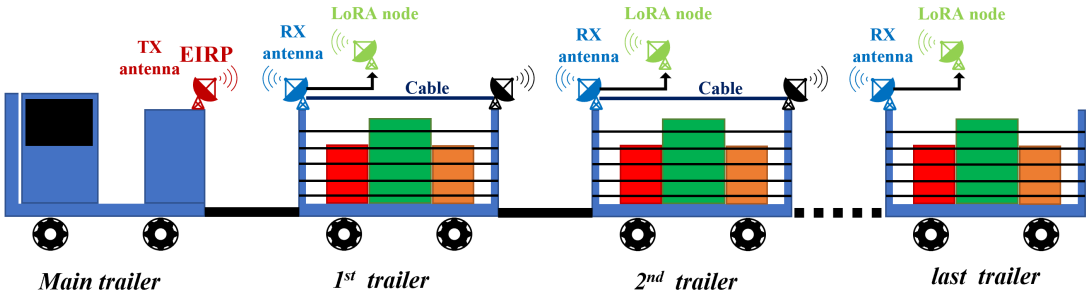

Figure 5.1: Pictorial representation of a train of unplugged trailers embedding WPT and LoRa communication. [93] © 2022 IEEE

An overview of the system implementation is presented in Fig. 5.1, where an active power transmitter is located on the first chart only, and couples of different wireless front-ends are located on the left and right edges of any other chart: the front-ends are connected to each other by a low loss coaxial cable laid along the length of the chart. Fig. 5.2 shows a block diagram representation of this installation: on the chart left edge, a power receiving block splits the power between the rectifier, supplying its LoRa node, and the cable, which guides the power to the right edge of the same chart, where a radiating element is used to wireless power the following

chart. In this way, a cascade scenario is established.

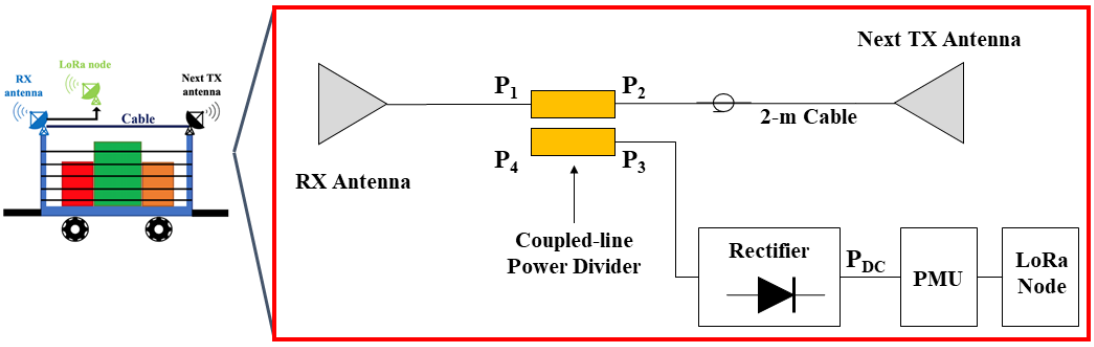

Figure 5.2: Details of the circuit blocks embedded into each trailer: at the receiving front-end a power splitter regulates the power to be provided at the input of the rectifier and to the cable which guides the remaining RF power to the far edge of the trailer, where the transmitting antenna is located. [93] © 2022 IEEE

The real application scenario delineates the constraints in terms of dimensions and operating distances that are the most relevant parameters to conduct an efficient design of the overall system. The maximum number of trailers, and thus LoRa nodes, that can be recharged in a minimum amount of time in order to ensure a continuous communication, is one of the main challenging goals on which the optimization has been based. A certain emphasis has been also given to obtain a modular system such that the performance is guaranteed regardless the mutual position and order of the trailers.

5.2 Selection of the Radiating Element: a 32-patch Antenna Array

Given the context and environment in which the system operates, patch antennas have been chosen as the most suitable topology also due to the presence of a back ground plane which contributes to keep the antenna insensitive to the material, mostly metal, on which they are attached. The antennas dedicated to energy harvesting are positioned at the chart edges and the reference distance between the charts is chosen to be 50 cm approximately. A good trade-off between dimensions and performance must be achieved to guarantee an efficient power transmission towards the highest number of trailers possible.

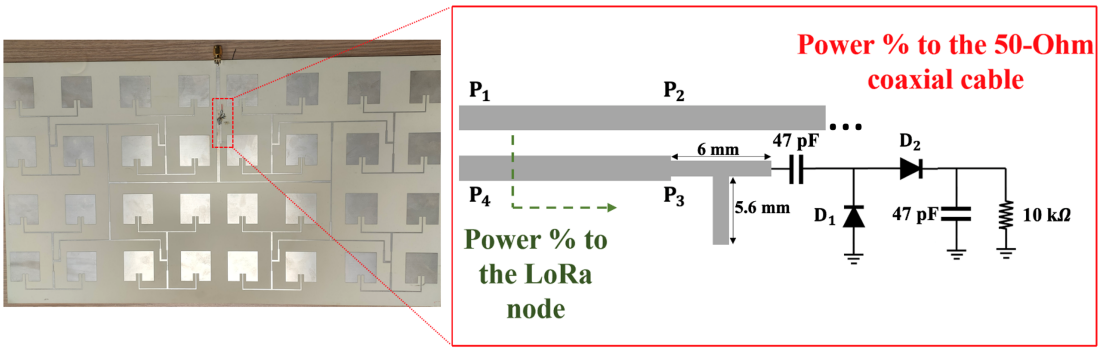

Figure 5.3: The realized antenna array with embedded power splitter and rectifier. [93] © 2022 IEEE

The antenna array is designed on Rogers 4350B ($\varepsilon_r = 3.66$ and $tan\delta = 0.0037$ at 10 GHz) and the chosen substrate thickness is 1.52 mm. In order to maximize the antenna gain without exceeding in the overall dimensions, a 32-patch array has been implemented, achieving an overall gain of 17 dBi.

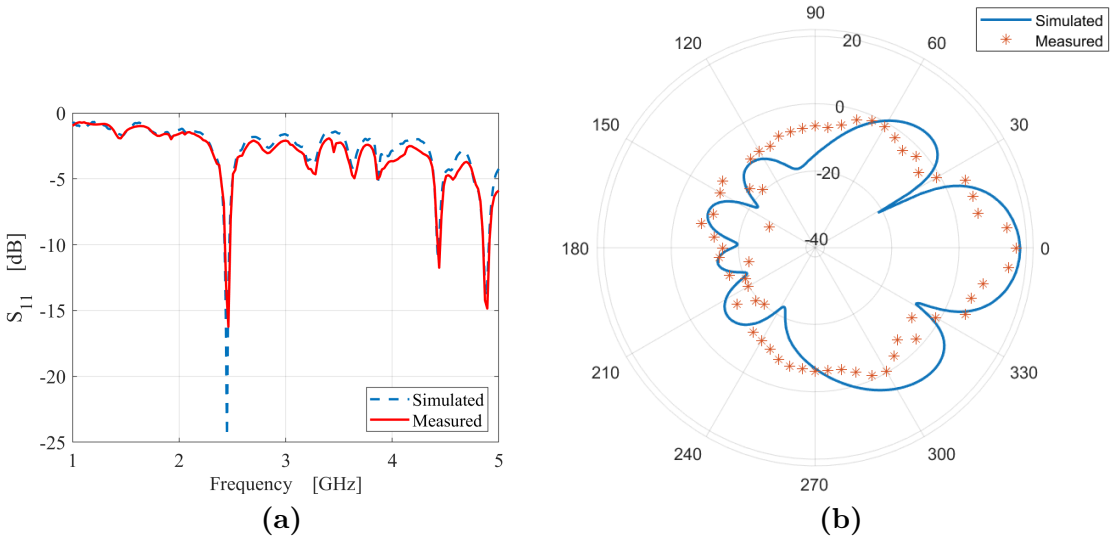

Figure 5.4: Measured and full-wave simulated array performance: (a) antenna reflection coefficient; (b) radiation diagrams in the E-plane. [93] © 2022 IEEE

The antenna has an overall volume of 487 x 287 x 1.52 mm^3 that has been found to be the best trade-off between performance and encumbrance, given the location on which the antennas have to be placed: the industrial trolley metal walls. Moreover, having double dimensions would imply obtaining a theoretical +3 dB increment of the antenna gain but it would result in a bulkier structure and a wider meandered array feeding network, which may lead to further losses. Fig. 5.3 shows the photo of the realized patch antenna array, embedding the power splitter and rectifier block, whereas in Fig. 5.4(a) and (b) the near-field and far-field measured and full-wave simulated performances are plotted, demonstrating very good agreement.

A quite high gain of the array, desired for a safe wireless power transmission between the trailers, is compatible with reciprocal position of the antennas of two neighbouring charts, that are expected in a line of sight.

The two antennas per trailer are connected by means of a high-performance 2-meter 50-Ω coaxial cable, which has a total attenuation of 0.66 dB.

5.3 Power Budget Evaluation and Rectifier Design

Preliminary calculations, considering a set of 4 trolleys of a length of 2 meters each, are carried out to compute the received power of each wireless link and to account for the cable attenuation occurring when connecting the two antennas of the same trailer. Furthermore, since the main purpose is to charge the LoRa node on each chart, a power splitter is coupled to each receiving array to provide the minimum amount of power to the LoRa node and at the same time to transfer the highest one to the far end edge of the same trailer through the coaxial cable.

One important design goal is to establish the appropriate power splitting percentage needed to provide sufficient power to recharge the last LoRa node while reaching the maximum number of possible trailers. A preliminary hypothesis could have been to fix a prescribed splitting percentage, however, since the first trailer would have a higher amount of received power with respect to the further ones, we have opted to collect a different power percentage from each trailer. In particular, for lower received power levels, thus for the farther trailers, the percentage collected power is higher than for the first ones which receive higher amount of power.

A coupled microstrip line power splitter has been derived on the same substrate of the antenna for providing different RF power percentages to the rectifier and to the cable. The whole sub-system, including the full-wave rectifier, has been designed by using the full-wave description of the antenna array within the nonlinear simulator, to determine the optimized geometry of the structure, with the goal of achieving the highest RF-to-dc efficiency at the lower power levels, thus guaranteeing the farthest LoRa node powering. With reference to Fig. 5.3, the following expression for the efficiency is used:

$$\eta_{RF-to-DC} = \frac{P_{DC}}{P_3} \tag{5.1}$$

$$P_3 = |S_{31}|^2 P_1 \tag{5.2}$$

The optimization has been carried out with respect to a received RF power ranging from -19 dBm to 14 dBm, imposing a different power splitting percentage depending on the power level.

The measured RF-to-dc efficiency is shown in Fig. 5.5. The constraint on the power percentage has led the rectifier efficiency not to be as maximum as it could be in a regular rectenna.

The measured power percentage entering the rectifier input is also shown in Fig. 5.5, ranging from almost 8% to 32% with respect to the received power by the antenna.

Finally, Table 5.1 reports the summary of the measured performance

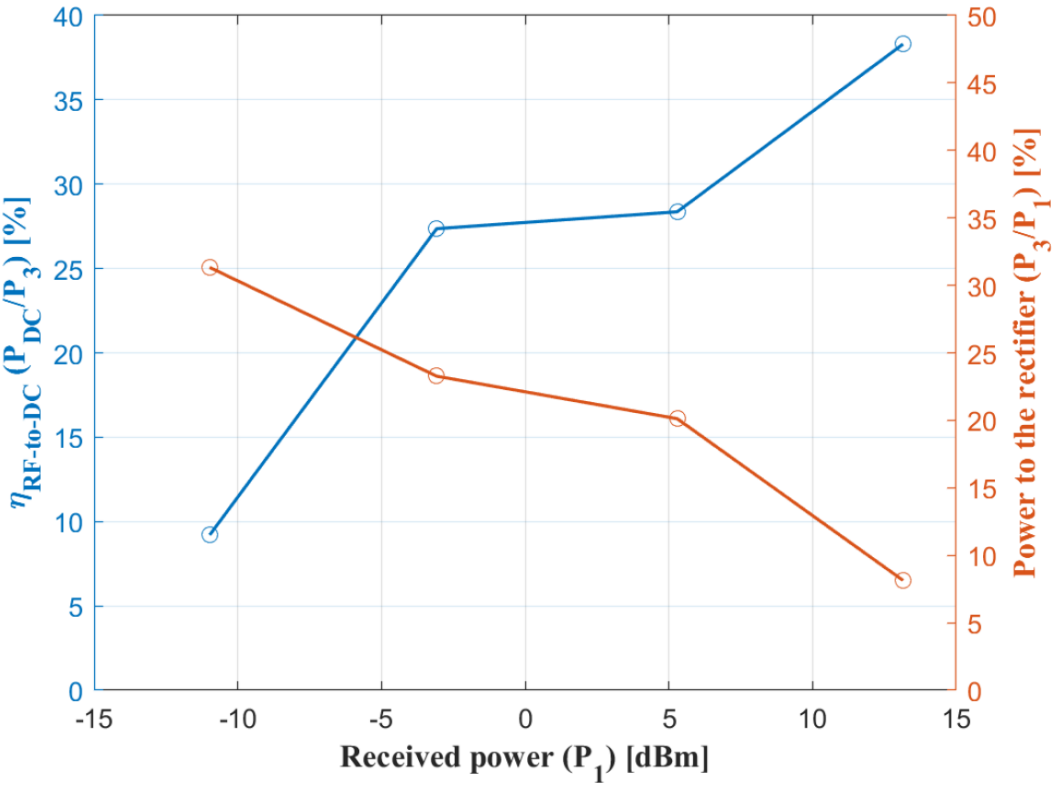

Figure 5.5: Measurement results of power conversion efficiency and the power splitting percentage to the LoRa node branch vs antenna array received power. © 2022 IEEE

belonging to each of the 4 trailers considered. It can be seen that the system is able to seamlessly increase the power splitter ratio to the rectifier when the total received power decreases. The resulting RF input power and RF-to-dc efficiency are also shown in the third and fourth rows respectively. As stated before, they are not optimized to be the highest possible one, but as an overall system performance to enable LoRa communication [98] for the maximum number of trailers. The last row of Tab. 5.1 reports the power that is provided to the next transmitting antenna on the same trailer, which corresponds to the previously defined remaining power from

Table 5.1: Summary of the measured performance of the system. [93] © 2022 IEEE

Trailer #	**1**	**2**	**3**	**4**
Received power at the front edge (P_1) [dBm]	13.15	5.29	-3.08	-10.98
Power splitter ratio to the rectifier [%]	8.14	20.12	23.27	31.33
Rectifier input power (P_3) [dBm]	2.26	-1.69	-9.43	-16.02
RF-to-DC efficiency [%]	38.30	28.36	27.36	9.20
Charging time of LoRa node [s]	4.1	14.2	22.1	226.6
Transmitted power at the back edge [dBm]	12.12	3.65	-4.91	-13.27

which the coaxial cable attenuation is subtracted.

Conclusion

This Thesis has described the outcomes of the research activity carried out during the PhD program. The main *"fil rouge"* is the aim of creating energy autonomous systems to be applied in various scenarios. The deep interest for the biomedical environment has set the basis for some of the applications described in this Thesis. Nevertheless, energy harvesting systems to be applied in industrial plants, to perform predictive maintenance or trailer tracking, have been also designed and developed. The obtained results show how energy autonomy can definitely be a breakthrough for modern IoT devices that allows to create more versatile systems to be applied both in medical and industrial scenarios.

The proof-of-concept described in Chapter 2 has demonstrated the feasibility of designing a rotation-insensitive wireless power transfer system for implantable devices, showing promising results for both miniaturization and power transfer efficiency. In the field of fluid detection, the energy-autonomous system proposed in Chapter 3 has brought interesting results both in the design, with the exploitation of a loaded coupled-line filter to perform frequency and fluid selectivity, and in the sensing capabilities, showing how a safe detection of the target solution can be performed.

Moving on to the millimeter wave frequency range, Chapter 4 has de-

scribed a novel WPT scenario exploiting Bessel Beam launchers. The obtained results show high-focusing capabilities, due to the intrinsic nature of these antennas, allowing to transfer power up to some centimetres with high precision.

Leaving the biomedical side to focus on applications to be used within industrial plants, Chapter 5 describes an application in which the concept of electromagnetically harsh environment is still a dominant challenge. The system not only accounts for the design of a WPT system to power batteryless nodes, but, during the design steps, focus has been given on obtaining an efficiency power distribution when having different trailers to be charged in a cascade configuration. Results have been promising, showing how system modularity can be achieved without affecting the wireless power transfer efficiency.

This Thesis has described the implementation of different systems within the field of wireless power transfer, setting the basis for future developments and paths.

In particular, several can be the aspects in which this work can be further improved:

- In the field of WPT for implantable devices, the rotational independency of the system proposed in Chapter 2 can be exploited for a further miniaturized system, together with a more extensive characterization of the overall system performance for different patient-specific

tissue layers.

- Further miniaturization the ethanol detector together with sensitivity enhancement.

- Always related to wearable applications, the study conducted in Chapter 4 has been a starting point that can lead to a more extensive design of mm-wave systems that can boast miniaturization and high performance at the same time.

- Realization of the Bessel Beam launcher prototype in order to perform a measurement campaign and also investigation of different feeding techniques.

- Regarding the system presented in Chapter 5, further improvements and development will be focused on obtaining a higher number of trailers that can be charged with a single power source located on the main trailer.

Concluding, the aim of removing batteries from electronic devices is an ongoing challenge that current researches are facing. Indeed, technology developments will allow to fill the missing gaps, such as extreme miniaturization and high efficiency, targeting energy autonomy as one of the most essential characteristics for future IoT devices.

Appendix

This presented Thesis gathers different works carried out by the author in the field of EH and WPT applications in electromagnetically harsh environments, for which she has played the role of main contributor. In the following, a short description of a multi-team work to which the author of this Thesis has partially contributed. The project has been fully described in the following articles:

[99] G. Paolini, M. Shanawani, A. Costanzo, F. Benassi, and D. Masotti, "Rf energy on-demand for automotive applications," in *2020 IEEE/MTT-S International Microwave Symposium (IMS)*, 2020, pp. 1191–1194

[100] G. Paolini, M. Guermandi, D. Masotti, M. Shanawani, F. Benassi, L. Benini, and A. Costanzo, "Rf-powered low-energy sensor nodes for predictive maintenance in electromagnetically harsh industrial environments," *Sensors*, vol. 21, no. 2, p. 386, 2021

and in the following PhD Thesis:

[101] G. Paolini, "Microwave radar and wireless power transfer systems for biomedical and industrial applications," 2021

Introduction

The following section aim at describing the design and experimental validation of CP antennas to be applied within an RF source called illuminator, operating in the 2.4 GHz band. The main purpose is to energize small sensor nodes dedicated to the remote monitoring and predictive maintenance of some components inside the engine compartment of a car [100]. This research has demonstrated that the sensors can be correctly powered without being equipped with batteries and can simultaneously communicate with a gateway in order to register, in a given amount of time, the acceleration and temperature registered by the sensors and relative to a specific part. The communication between the gateway and sensor nodes is allowed by the use of a LoRa protocol, operating in the same frequency band of the RF powering system. This way allows to prevent or register possible malfunctioning, failure, or unwanted warmings of the tagged components. Being the presented works multi-team, the following section is focused on the description of a specific element of the overall structure: the CP TX antenna.

Design and Realization of the 2.45-GHz RF Illuminator

The illuminator circuitry is realized by using off-the-shelf components, such as the Maxim MAX2750 voltage-controlled oscillators (VCO), having an output power of -3 dBm in the 2.4 GHz ISM band; this frequency band is selected to design reduced-dimension antennas both on the transmitter and receiver side of the system. Using a VCO allows for dynamically selecting the illuminators operating frequency to perform frequency division between the powering and the communication operations. The VCO tuning voltage input is defined by a voltage control element (Linear Technology LT6650), that is set to have the oscillator signal at 2.45 GHz. This is done to have a sufficient distance in the spectrum between the energy harvesting signal and the LoRa communication one (at 2.401 GHz). Other main components of the illuminator are the RF amplifiers (Skyworks SE2598L) that have the are responsible for feeding the antennas incoherently; to avoid the generation of an array made by the three antennas, but three distinct energy sources. They provide an input power of 23 dBm to the transmitting circularly polarized (CP) patch antennas, whose gain is measured to be around 4 dBi, thus the overall EIRP is of 27 dBm, in compliance with the current regulations. Circular polarization, obtained by the corner-trimming technique, shown in Fig. 5.6, is chosen to ensure efficiency when providing

power to each sensor regardless of their mutual position with respect to the incident EM waves. Fig. 5.7 shows the axial ratio at 2.45 GHz for each

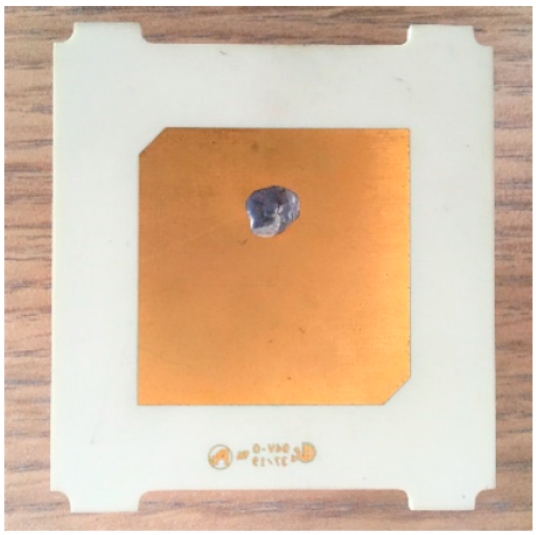

Figure 5.6: Pictorial representation of the CP patch antenna with trimmed corners [100].

antenna of the illuminator; the value is lower than 5 dBi for azimuthal rotations in the $\pm 100°$ range.

The board substrate of the feeding circuitry is Rogers RO4360G2 (thickness 0.610 mm, $\varepsilon_r = 6.15$, $tan\delta = 0.0038$), chosen to have a reduced microstrip line width of 0.9 mm for a 50-Ω impedance together with low dielectric losses, with respect to a standard FR4 substrate ($\varepsilon_r = 4.3$, $tan\delta = 0.025$). On the other hand, three CP patch antennas are realized on a thicker and less dense Rogers RO4350B (thickness 1.524 mm, $\varepsilon_r = 3.48$, $tan\delta = 0.0037$) and they are connected to the board by means of right-angle coaxial connectors. A pictorial representation of the realized RF source is shown in Figs. 5.8, including the three CP antennas mutually rotated by

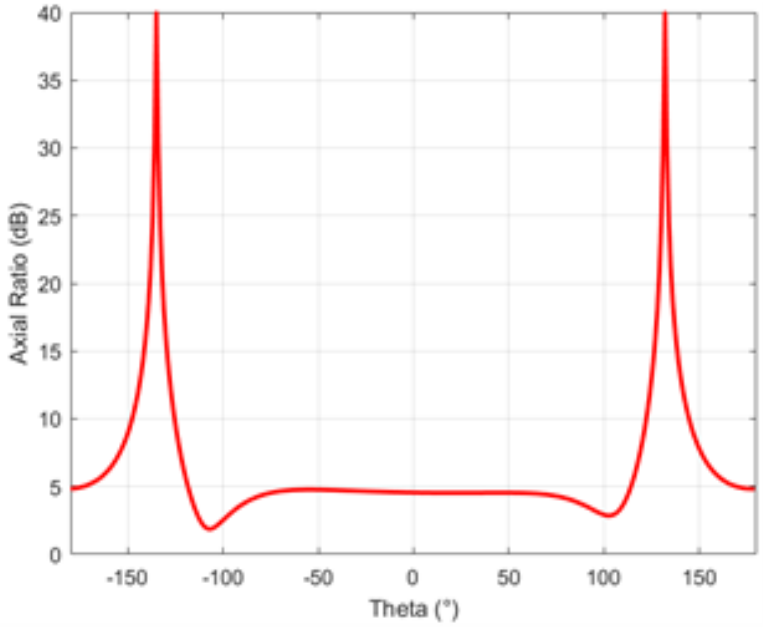

Figure 5.7: Plot of the axial ratio of each TX antenna.

45° for a wider power coverage. The overall dimensions of the illuminator prototype are 13 x 6 x 5.5 cm^3. Fig. 5.9a shows the simulated normalized radiation pattern of each stand-alone antennas, whereas Fig. 5.9b displays the normalized total radiation pattern (measured and simulated) due to the incoherent and simultaneous feeding strategy of the antennas (Fig. 5.9b), both in the horizontal plane.

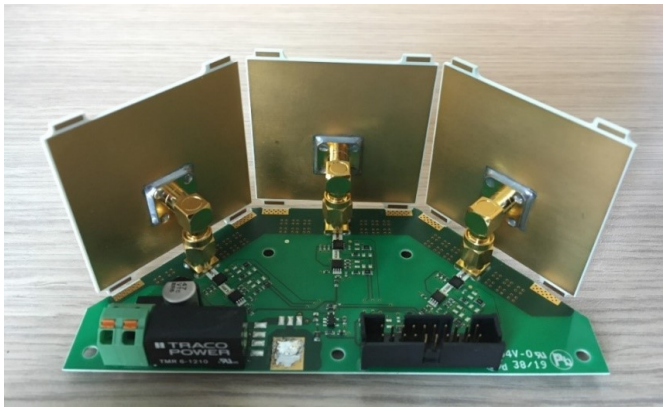

(a)

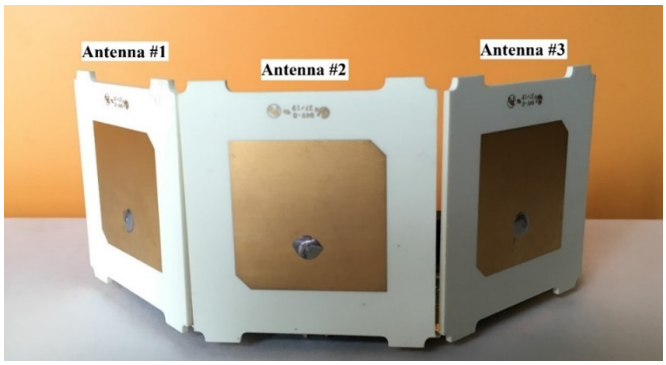

(b)

Figure 5.8: (a) Picture of the illuminator feeding circuitry working in the 2.4 GHz band. (b) Front view with the three coaxial-fed CP patch antennas. [99] © 2020 IEEE

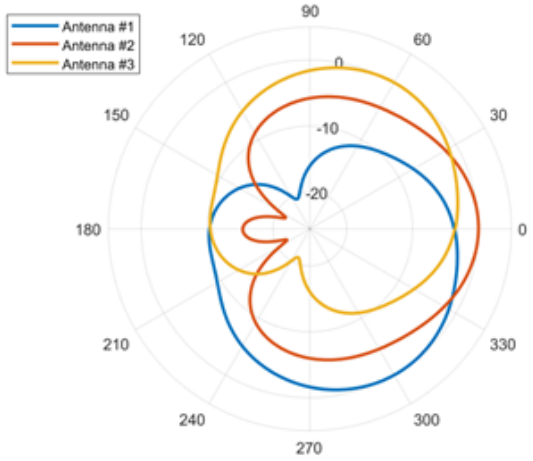

(a)

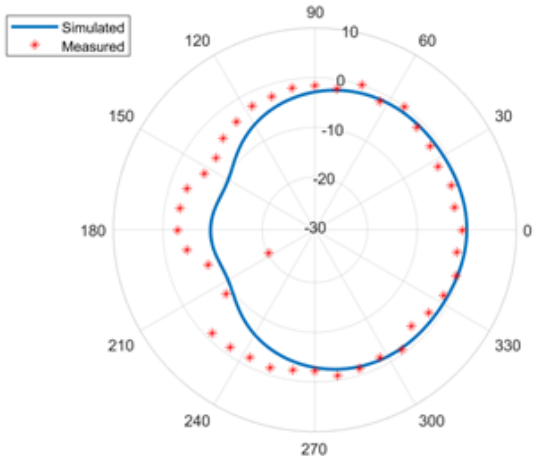

(b)

Figure 5.9: (a) Normalized simulated power patterns (in dB) of the self-standing three illuminator CP patch antennas and (b) normalized simulated and measured power patterns of the entire RF illuminator, both in the horizontal plane [100].

Bibliography

[1] J. Lin, W. Yu, N. Zhang, X. Yang, H. Zhang, and W. Zhao, "A survey on internet of things: Architecture, enabling technologies, security and privacy, and applications," *IEEE Internet of Things Journal*, vol. 4, no. 5, pp. 1125–1142, 2017.

[2] F. Aktas, C. Ceken, and Y. E. Erdemli, "Iot-based healthcare framework for biomedical applications," *Journal of Medical and Biological Engineering*, vol. 38, no. 6, pp. 966–979, 2018.

[3] O. Friha, M. A. Ferrag, L. Shu, L. Maglaras, and X. Wang, "Internet of things for the future of smart agriculture: A comprehensive survey of emerging technologies," *IEEE/CAA Journal of Automatica Sinica*, vol. 8, no. 4, pp. 718–752, 2021.

[4] Y. Song, F. R. Yu, L. Zhou, X. Yang, and Z. He, "Applications of the internet of things (iot) in smart logistics: A comprehensive survey," *IEEE Internet of Things Journal*, vol. 8, no. 6, pp. 4250–4274, 2021.

[5] M. Shahroz, M. F. Mushtaq, M. Ahmad, S. Ullah, A. Mehmood, and G. S. Choi, "Iot-based smart shopping cart using radio frequency identification," *IEEE Access*, vol. 8, pp. 68 426–68 438, 2020.

[6] A. Costanzo, F. Benassi, and M. Giuseppina, "Wearable, energy-autonomous rf microwave systems," *IEEE Microwave Magazine*, vol. 22, no. 12, pp. 48–59, 2022.

[7] S. Gahlot, S. R. N. Reddy, and D. Kumar, "Review of smart health monitoring approaches with survey analysis and proposed framework," *IEEE Internet of Things Journal*, vol. 6, no. 2, pp. 2116–2127, 2019.

[8] Y. Shen, H. Zhang, Y. Fan, A. P. Lee, and L. Xu, "Smart health of ultrasound telemedicine based on deeply represented semantic segmentation," *IEEE Internet of Things Journal*, vol. 8, no. 23, pp. 16 770–16 778, 2021.

[9] E. Spanò, S. Di Pascoli, and G. Iannaccone, "Low-power wearable ecg monitoring system for multiple-patient remote monitoring," *IEEE Sensors Journal*, vol. 16, no. 13, pp. 5452–5462, 2016.

[10] W. Li, B. Tan, and R. Piechocki, "Passive radar for opportunistic monitoring in e-health applications," *IEEE Journal of Translational Engineering in Health and Medicine*, vol. 6, pp. 1–10, 2018.

[11] F. Hu, Y. Xiao, and Q. Hao, "Congestion-aware, loss-resilient bio-monitoring sensor networking for mobile health applications," *IEEE Journal on Selected Areas in Communications*, vol. 27, no. 4, pp. 450–465, 2009.

[12] H. U. Chung, B. H. Kim, J. Y. Lee, J. Lee, Z. Xie, E. M. Ibler, K. Lee, A. Banks, J. Y. Jeong, J. Kim *et al.*, "Binodal, wireless epidermal electronic systems with in-sensor analytics for neonatal intensive care," *Science*, vol. 363, no. 6430, 2019.

[13] A. A. N. Shirehjini, A. Yassine, and S. Shirmohammadi, "Equipment location in hospitals using rfid-based positioning system," *IEEE Transactions on Information Technology in Biomedicine*, vol. 16, no. 6, pp. 1058–1069, 2012.

[14] E. Borelli, G. Paolini, F. Antoniazzi, M. Barbiroli, F. Benassi, F. Chesani, L. Chiari, M. Fantini, F. Fuschini, A. Galassi *et al.*, "Habitat: An iot solution for independent elderly," *Sensors*, vol. 19, no. 5, p. 1258, 2019.

[15] S. de Miguel-Bilbao, J. Roldán, J. García, F. López, P. García-Sagredo, and V. Ramos, "Comparative analysis of indoor location technologies for monitoring of elderly," in *2013 IEEE 15th International Conference on e-Health Networking, Applications and Services (Healthcom 2013)*, 2013, pp. 320–323.

[16] A. Khanna and S. Kaur, "Internet of things (iot), applications and challenges: A comprehensive review," *Wireless Personal Communications*, vol. 114, pp. 1687–1762, 2020.

[17] B. Pozo, J. I. Garate, J. Á. Araujo, and S. Ferreiro, "Energy harvesting technologies and equivalent electronic structural models," *Electronics*, vol. 8, no. 5, p. 486, 2019.

[18] A. Khaligh, P. Zeng, and C. Zheng, "Kinetic energy harvesting using piezoelectric and electromagnetic technologies—state of the art," *IEEE Transactions on Industrial Electronics*, vol. 57, no. 3, pp. 850–860, 2010.

[19] X. Yue, M. Kauer, M. Bellanger, O. Beard, M. Brownlow, D. Gibson, C. Clark, C. MacGregor, and S. Song, "Development of an indoor photovoltaic energy harvesting module for autonomous sensors in building air quality applications," *IEEE Internet of Things Journal*, vol. 4, no. 6, pp. 2092–2103, 2017.

[20] L. Sigrist, N. Stricker, D. Bernath, J. Beutel, and L. Thiele, "Thermoelectric energy harvesting from gradients in the earth surface," *IEEE Transactions on Industrial Electronics*, vol. 67, no. 11, pp. 9460–9470, 2020.

[21] H. Uluşan, K. Gharehbaghi, Ö. Zorlu, A. Muhtaroğlu, and H. Külah, "A fully integrated and battery-free interface for low-voltage electromagnetic energy harvesters," *IEEE Transactions on Power Electronics*, vol. 30, no. 7, pp. 3712–3719, 2014.

[22] Y.-W. Chong, W. Ismail, K. Ko, and C.-Y. Lee, "Energy harvesting for wearable devices: A review," *IEEE Sensors Journal*, vol. 19, no. 20, pp. 9047–9062, 2019.

[23] F. K. Shaikh and S. Zeadally, "Energy harvesting in wireless sensor networks: A comprehensive review," *Renewable and Sustainable Energy Reviews*, vol. 55, pp. 1041–1054, 2016.

[24] M. Piñuela, P. D. Mitcheson, and S. Lucyszyn, "Ambient rf energy harvesting in urban and semi-urban environments," *IEEE Transactions on Microwave Theory and Techniques*, vol. 61, no. 7, pp. 2715–2726, 2013.

[25] S. Lemey, F. Declercq, and H. Rogier, "Textile antennas as hybrid energy-harvesting platforms," *Proceedings of the IEEE*, vol. 102, no. 11, pp. 1833–1857, 2014.

[26] R. Moro, S. Agneessens, H. Rogier, A. Dierck, and M. Bozzi, "Textile microwave components in substrate integrated waveguide technology," *IEEE Transactions on Microwave Theory and Techniques*, vol. 63, no. 2, pp. 422–432, 2015.

[27] J. Antonio Estrada, E. Kwiatkowski, A. López-Yela, M. Borgoñós-García, D. Segovia-Vargas, T. Barton, and Z. Popović, "Rf-harvesting tightly coupled rectenna array tee-shirt with greater than octave bandwidth," *IEEE Transactions on Microwave Theory and Techniques*, vol. 68, no. 9, pp. 3908–3919, 2020.

[28] S.-E. Adami, P. Proynov, G. S. Hilton, G. Yang, C. Zhang, D. Zhu, Y. Li, S. P. Beeby, I. J. Craddock, and B. H. Stark, "A flexible 2.45-ghz power harvesting wristband with net system output from-24.3 dbm of rf power," *IEEE Transactions on Microwave Theory and Techniques*, vol. 66, no. 1, pp. 380–395, 2017.

[29] H. S. Vu, N. Nguyen, N. Ha-Van, C. Seo, and M. Thuy Le, "Multi-band ambient rf energy harvesting for autonomous iot devices," *IEEE Microwave and Wireless Components Letters*, vol. 30, no. 12, pp. 1189–1192, 2020.

[30] S. Mandal, L. Turicchia, and R. Sarpeshkar, "A low-power, battery-free tag for body sensor networks," *IEEE Pervasive Computing*, vol. 9, no. 1, pp. 71–77, 2009.

[31] C. Viehweger, T. Keutel, and O. Kanoun, "Energy harvesting for wireless sensor nodes in factory environments," in *2014 IEEE 11th International Multi-Conference on Systems, Signals & Devices (SSD14)*. IEEE, 2014, pp. 1–4.

[32] T. Ruan, Z. J. Chew, and M. Zhu, "Energy-aware approaches for energy harvesting powered wireless sensor nodes," *IEEE Sensors Journal*, vol. 17, no. 7, pp. 2165–2173, 2017.

[33] A. Berger, L. B. Hörmann, C. Leitner, S. B. Oswald, P. Priller, and A. Springer, "Sustainable energy harvesting for robust wireless sensor networks in industrial applications," in *2015 IEEE Sensors Applications Symposium (SAS)*. IEEE, 2015, pp. 1–6.

[34] C. A. Balanis, *Antenna theory: analysis and design*. John wiley & sons, 2015.

[35] Z. Zhang, K. T. Chau, C. Liu, F. Li, and T. W. Ching, "Quantitative analysis of mutual inductance for optimal wireless power transfer via magnetic resonant coupling," *IEEE Transactions on Magnetics*, vol. 50, no. 11, pp. 1–4, 2014.

[36] J. Kim, A. Banks, Z. Xie, S. Y. Heo, P. Gutruf, J. W. Lee, S. Xu, K.-I. Jang, F. Liu, G. Brown, J. Choi, J. H. Kim, X. Feng, Y. Huang, U. Paik, and J. A. Rogers, "Miniaturized flexible electronic systems with wireless power and near-field communication capabilities," *Advanced Functional Materials*, vol. 25, no. 30, pp. 4761–4767, 2015.

[37] J. S. Ho, S. Kim, and A. S. Poon, "Midfield wireless powering for implantable systems," *Proceedings of the IEEE*, vol. 101, no. 6, pp. 1369–1378, 2013.

[38] U. Olgun, C.-C. Chen, and J. L. Volakis, "Investigation of rectenna array configurations for enhanced rf power harvesting," *IEEE Antennas and Wireless Propagation Letters*, vol. 10, pp. 262–265, 2011.

[39] X. Li, L. Yang, and L. Huang, "Novel design of 2.45-ghz rectenna element and array for wireless power transmission," *IEEE Access*, vol. 7, pp. 28 356–28 362, 2019.

[40] H. Sun, Y.-x. Guo, M. He, and Z. Zhong, "Design of a high-efficiency 2.45-ghz rectenna for low-input-power energy harvesting," *IEEE Antennas and Wireless Propagation Letters*, vol. 11, pp. 929–932, 2012.

[41] M. Fantuzzi, "Design and modelling of wireless power transfer and energy harvesting systems," 2018.

[42] X. Gu, P. Burasa, S. Hemour, and K. Wu, "Recycling ambient rf energy: Far-field wireless power transfer and harmonic backscattering," *IEEE Microwave Magazine*, vol. 22, no. 9, pp. 60–78, 2021.

[43] A. Pacini, F. Benassi, D. Masotti, and A. Costanzo, "Design of a miniaturized omni-directional rf-to-dc ir-wpt," in *2018 IEEE Wireless Power Transfer Conference (WPTC)*, 2018, pp. 1–4.

[44] F. Benassi, D. Masotti, and A. Costanzo, "Engineered and miniaturized 13.56 mhz omni-directional wpt system for medical applications," in *2019 IEEE International Conference on RFID Technology and Applications (RFID-TA)*, 2019, pp. 306–309.

[45] K. Agarwal, R. Jegadeesan, Y.-X. Guo, and N. V. Thakor, "Wireless power transfer strategies for implantable bioelectronics," *IEEE reviews in biomedical engineering*, vol. 10, pp. 136–161, 2017.

[46] G. B. Joun and B. H. Cho, "An energy transmission system for an artificial heart using leakage inductance compensation of transcutaneous transformer," *IEEE Transactions on Power Electronics*, vol. 13, no. 6, pp. 1013–1022, 1998.

[47] A. Pacini, A. Costanzo, S. Aldhaher, and P. D. Mitcheson, "Load- and position-independent moving mhz wpt system based on gan-distributed current sources," *IEEE Transactions on Microwave Theory and Techniques*, vol. 65, no. 12, pp. 5367–5376, 2017.

[48] A. Pacini, F. Benassi, D. Masotti, and A. Costanzo, "Design of a rf-to-dc link for in-body ir-wpt with a capsule-shaped rotation-insensitive receiver," in *2018 IEEE/MTT-S International Microwave Symposium-IMS*. IEEE, 2018, pp. 1289–1292.

[49] V. Rizzoli, A. Costanzo, and G. Monti, "General electromagnetic compatibility analysis for nonlinear microwave integrated circuits," in *2004 IEEE MTT-S International Microwave Symposium Digest (IEEE Cat. No. 04CH37535)*, vol. 2. IEEE, 2004, pp. 953–956.

[50] T. Ohira, "The kq product as viewed by an analog circuit engineer," *IEEE Circuits and Systems Magazine*, vol. 17, no. 1, pp. 27–32, 2017.

[51] A. Costanzo, M. Dionigi, D. Masotti, M. Mongiardo, G. Monti, L. Tarricone, and R. Sorrentino, "Electromagnetic energy harvesting and wireless power transmission: A unified approach," *Proceedings of the IEEE*, vol. 102, no. 11, pp. 1692–1711, 2014.

[52] K. Van Schuylenbergh and R. Puers, *Inductive powering: basic theory and application to biomedical systems*. Springer Science & Business Media, 2009.

[53] A. Costanzo, M. Dionigi, F. Mastri, M. Mongiardo, J. A. Russer, and P. Russer, "Rigorous design of magnetic-resonant wireless power transfer links realized with two coils," in *2014 44th European Microwave Conference*. IEEE, 2014, pp. 414–417.

[54] C. Gabriel, "Compilation of the dielectric properties of body tissues at rf and microwave frequencies." King's Coll London (United Kingdom) Dept of Physics, Tech. Rep., 1996.

[55] "Icnirp," https://www.icnirp.org/en/activities/news/news-article/rf-guidelines-2020-published.html.

[56] F. Benassi, N. Zincarelli, D. Masotti, and A. Costanzo, "A wearable passive microwave fluid sensor wirelessly activated," in *2019 IEEE Wireless Power Transfer Conference (WPTC)*. IEEE, 2019, pp. 236–240.

[57] F. Benassi, G. Paolini, D. Masotti, and A. Costanzo, "A wearable flexible energy-autonomous filtenna for ethanol detection at 2.45 ghz," *IEEE Transactions on Microwave Theory and Techniques*, 2021.

[58] J. Leroy, C. Dalmay, A. Landoulsi, F. Hjeij, C. Mélin, B. Bessette, C. Bounaix Morand du Puch, S. Giraud, C. Lautrette, S. Battu,

F. Lalloué, M. Jauberteau, A. Bessaudou, P. Blondy, and A. Pothier, "Microfluidic biosensors for microwave dielectric spectroscopy," *Sensors and Actuators A: Physical*, vol. 229, pp. 172–181, 2015.

[59] K. Grenier, D. Dubuc, T. Chen, F. Artis, T. Chretiennot, M. Poupot, and J.-J. Fournié, "Recent advances in microwave-based dielectric spectroscopy at the cellular level for cancer investigations," *IEEE Transactions on Microwave Theory and Techniques*, vol. 61, no. 5, pp. 2023–2030, 2013.

[60] A. A. Helmy, S. Kabiri, M. M. Bajestan, and K. Entesari, "Complex permittivity detection of organic chemicals and mixtures using a 0.5–3-ghz miniaturized spectroscopy system," *IEEE transactions on microwave theory and techniques*, vol. 61, no. 12, pp. 4646–4659, 2013.

[61] T. Chretiennot, D. Dubuc, and K. Grenier, "A microwave and microfluidic planar resonator for efficient and accurate complex permittivity characterization of aqueous solutions," *IEEE Transactions on Microwave Theory and Techniques*, vol. 61, no. 2, pp. 972–978, 2012.

[62] ——, "Double stub resonant biosensor for glucose concentrations quantification of multiple aqueous solutions," in *2014 IEEE MTT-S International Microwave Symposium (IMS2014)*. IEEE, 2014, pp. 1–4.

[63] ——, "Optimized electromagnetic interaction microwave resonator/microfluidic channel for enhanced liquid bio-sensor," in *2013 European Microwave Conference*. IEEE, 2013, pp. 464–467.

[64] T. Chen, D. Dubuc, M. Poupot, J.-J. Fournié, and K. Grenier, "Broadband discrimination of living and dead lymphoma cells with a microwave interdigitated capacitor," in *2013 IEEE Topical Conference on Biomedical Wireless Technologies, Networks, and Sensing Systems*. IEEE, 2013, pp. 64–66.

[65] B. S. Cook, J. R. Cooper, and M. M. Tentzeris, "An inkjet-printed microfluidic rfid-enabled platform for wireless lab-on-chip applications," *IEEE Transactions on microwave theory and techniques*, vol. 61, no. 12, pp. 4714–4723, 2013.

[66] D. M. Pozar, *Microwave Engineering*. Hoboken, NJ, USA: John Wiley & Sons, 2009.

[67] A. Costanzo and D. Masotti, "Energizing 5g: Near-and far-field wireless energy and data trantransfer as an enabling technology for the 5g iot," *IEEE Microwave Magazine*, vol. 18, no. 3, pp. 125–136, 2017.

[68] V. Rizzoli, A. Costanzo, D. Masotti, P. Spadoni, and A. Neri, "Prediction of the end-to-end performance of a microwave/rf link by means of nonlinear/electromagnetic co-simulation," *IEEE transactions on microwave theory and techniques*, vol. 54, no. 12, pp. 4149–4160, 2006.

[69] A. Costanzo, D. Masotti, M. Fantuzzi, and M. Del Prete, "Co-design strategies for energy-efficient uwb and uhf wireless systems," *IEEE Transactions on Microwave Theory and Techniques*, vol. 65, no. 5, pp. 1852–1863, 2017.

[70] T. Jensen, V. Zhurbenko, V. Krozer, and P. Meincke, "Coupled transmission lines as impedance transformer," *IEEE Transactions on microwave Theory and Techniques*, vol. 55, no. 12, pp. 2957–2965, 2007.

[71] J.-Z. Bao, M. L. Swicord, and C. C. Davis, "Microwave dielectric characterization of binary mixtures of water, methanol, and ethanol," *The Journal of chemical physics*, vol. 104, no. 12, pp. 4441–4450, 1996.

[72] F. Benassi, W. Fuscaldo, D. Masotti, A. Galli, and A. Costanzo, "Wireless power transfer in the radiative near-field through resonant bessel-beam launchers at millimeter waves," in *2021 IEEE Wireless Power Transfer Conference (WPTC)*, 2021, pp. 1–4.

[73] F. Benassi, W. Fuscaldo, E. Negri, G. Paolini, E. Augello, D. Masotti, P. Burghignoli, A. Galli, and A. Costanzo, "Comparison between Hybrid- and TM-polarized Bessel-beam launchers for wireless power transfer in the radiative near-field at millimeter waves," in *Eur. Microw. Conf. (EuMC 2021)*. 2022, [Accepted Paper].

[74] W. Fuscaldo, G. Valerio, A. Galli, R. Sauleau, A. Grbic, and M. Ettorre, "Higher-order leaky-mode Bessel-beam launcher," *IEEE Trans. Antennas Propag.*, vol. 64, no. 3, pp. 904–913, Mar. 2016.

[75] W. Fuscaldo, "Advanced radiating systems based on leaky waves and nondiffracting waves," Ph.D. dissertation, Rennes 1, 2017.

[76] C. Balanis, *Advanced Engineering Electromagnetics*. Wiley Online Library, 2012, vol. 111.

[77] R. W. Ziolkowski, "Localized transmission of electromagnetic energy," *Phys. Rev. A*, vol. 39, no. 4, p. 2005, 1989.

[78] M. Nariman, F. Shirinfar, A. Papió Toda, S. Pamarti, A. Rofougaran, and F. De Flaviis, "A compact 60-Ghz wireless power transfer system," *IEEE Trans. Microw. Theory Tech.*, vol. 64, no. 8, pp. 2664–2677, 2016.

[79] J. Garnica, R. A. Chinga, and J. Lin, "Wireless power transmission: From far field to near field," *Proceedings of the IEEE*, vol. 101, no. 6, pp. 1321–1331, 2013.

[80] D. R. Smith, V. R. Gowda, O. Yurduseven, S. Larouche, G. Lipworth, Y. Urzhumov, and M. S. Reynolds, "An analysis of beamed wireless power transfer in the Fresnel zone using a dynamic, metasurface aperture," *J. Appl. Phys.*, vol. 121, no. 1, p. 014901, 2017.

[81] J. D. Heebl, M. Ettorre, and A. Grbic, "Wireless links in the radiative near field via Bessel beams," *Phys. Rev. Appl.*, vol. 6, no. 3, p. 034018, 2016.

[82] M. Ettorre, S. C. Pavone, M. Casaletti, M. Albani, A. Mazzinghi, and A. Freni, "Near-field focusing by non-diffracting Bessel beams," in *Aperture Antennas for Millimeter and Sub-Millimeter Wave Applications*. Cham, Switzerland: Springer, 2018, pp. 243–288.

[83] M. Ettorre and A. Grbic, "Generation of propagating Bessel beams using leaky-wave modes," *IEEE Trans. Antennas Propag.*, vol. 60, no. 8, pp. 3605–3613, 2012.

[84] W. Fuscaldo, S. C. Pavone, D. Comite, G. Valerio, M. Albani, M. Ettorre, and A. Galli, "Design criteria of X-wave launchers for millimeter-wave applications," *Int. J. Microwave Wireless Techn.*, vol. 11, no. 9, pp. 939–949, 2019.

[85] M. Albani, S. C. Pavone, M. Casaletti, and M. Ettorre, "Generation of non-diffractive Bessel beams by inward cylindrical traveling wave aperture distributions," *Opt. Express*, vol. 22, no. 15, pp. 18 354–18 364, 2014.

[86] P. Burghignoli, W. Fuscaldo, D. Comite, P. Baccarelli, and A. Galli, "Higher-order cylindrical leaky waves–Part I: Canonical sources and radiation formulas," *IEEE Trans. Antennas Propag.*, vol. 67, no. 11, pp. 6735–6747, 2019.

[87] V. Rizzoli, D. Masotti, N. Arbizzani, and A. Costanzo, "CAD procedure for predicting the energy received by wireless scavenging systems in the near- and far-field regions," in *2010 IEEE MTT-S Int. Microw. Symp.*, 2010, pp. 1768–1771.

[88] G. Monti, D. Masotti, G. Paolini, L. Corchia, A. Costanzo, M. Dionigi, F. Mastri, M. Mongiardo, R. Sorrentino, and L. Tarricone, "EMC and EMI issues of WPT systems for wearable and implantable devices," *IEEE Electromagn. Compat. Mag.*, vol. 7, no. 1, pp. 67–77, 2018.

[89] P. Lu, D. Voyer, A. Bréard, J. Huillery, B. Allard, X. Lin-Shi, and X.-S. Yang, "Design of TE-polarized Bessel antenna in microwave range using leaky-wave modes," *IEEE Trans. Antennas Propag.*, vol. 66, no. 1, pp. 32–41, 2017.

[90] W. Fuscaldo, "Rigorous evaluation of losses in uniform leaky-wave antennas," *IEEE Trans. Antennas Propag.*, vol. 68, no. 2, pp. 643–655, Feb. 2020.

[91] S. Tretyakov, *Analytical Modeling in Applied Electromagnetics*. Norwood, MA, USA: Artech House, 2003.

[92] W. Fuscaldo, S. Tofani, D. C. Zografopoulos, P. Baccarelli, P. Burghignoli, R. Beccherelli, and A. Galli, "Systematic design of THz leaky-wave antennas based on homogenized metasurfaces," *IEEE Trans. Antennas Propag.*, vol. 66, no. 3, pp. 1169–1178, Mar. 2018.

[93] B. Gok, F. Benassi, D. Masotti, and A. Costanzo, "A wireless/wired uhf modular system combining energy and data transfer," in *2022 IEEE Wireless Power Transfer Conference (WPTC)*. 2022, [Accepted Paper].

[94] F. Flammini, A. Gaglione, D. Tokody, and D. Dohrilovic, "LoRa WAN Roaming for Intelligent Shipment Tracking," in *2020 IEEE Global Conference on Artificial Intelligence and Internet of Things (GCAIoT)*, 2020, pp. 01–02.

[95] U. Raza, P. Kulkarni, and M. Sooriyabandara, "Low Power Wide Area Networks: An Overview," *IEEE Communications Surveys Tutorials*, vol. 19, no. 2, pp. 855–873, 2017.

[96] I. F. Priyanta, F. Golatowski, T. Schulz, and D. Timmermann, "Evaluation of LoRa Technology for Vehicle and Asset Tracking in Smart

Harbors," in *IECON 2019 - 45th Annual Conference of the IEEE Industrial Electronics Society*, vol. 1, 2019, pp. 4221–4228.

[97] H. Li, K. Ota, M. Dong, and H.-H. Chen, "Efficient Energy Transport in 60 GHz for Wireless Industrial Sensor Networks," *IEEE Wireless Communications*, vol. 24, no. 5, pp. 143–149, 2017.

[98] M. Ballerini, T. Polonelli, D. Brunelli, M. Magno, and L. Benini, "NB-IoT Versus LoRaWAN: An Experimental Evaluation for Industrial Applications," *IEEE Transactions on Industrial Informatics*, vol. 16, no. 12, pp. 7802–7811, 2020.

[99] G. Paolini, M. Shanawani, A. Costanzo, F. Benassi, and D. Masotti, "Rf energy on-demand for automotive applications," in *2020 IEEE/MTT-S International Microwave Symposium (IMS)*, 2020, pp. 1191–1194.

[100] G. Paolini, M. Guermandi, D. Masotti, M. Shanawani, F. Benassi, L. Benini, and A. Costanzo, "Rf-powered low-energy sensor nodes for predictive maintenance in electromagnetically harsh industrial environments," *Sensors*, vol. 21, no. 2, p. 386, 2021.

[101] G. Paolini, "Microwave radar and wireless power transfer systems for biomedical and industrial applications," 2021.